SPARTAN 2.5 User's Manual

Mário Lino da Silva, Bruno Lopez, and Susana Espinho

July 17, 2013

Contents

Introduction **1**

1 Getting Started **3**
1.1 Launching the SPARTAN code 4
1.1.1 Running the Graphical User Interface (GUI) of the SPARTAN code 4
1.1.2 How the Graphical User Interface works 6
1.1.3 Other user-defined parameters 6
1.1.4 Running the SPARTAN code without the Graphical User Interface 6
1.2 Recorded data 6
1.3 Sample comparisons 7
1.4 Stepping a little further 7

2 Physical Models **9**
2.1 Discrete radiation models 9
2.1.1 Selection rules 9
2.1.2 Line positions and intensities 13
2.1.3 Broadening mechanisms 20
2.2 Continuum radiation models 23
2.2.1 Transition intensities 24
2.2.2 Special cases 25
2.3 Generalized Kirchhoff–Planck Law for radiative transfer 26
2.3.1 Discrete transitions 26
2.3.2 Photoionization transitions 26
2.3.3 Photodissociation transitions 27
2.3.4 Bremsstrahlung transitions 27

3 Detailed Description of the Code **29**
3.1 Introduction 29
3.2 Summary of the capabilities of the SPARTAN code 31
3.3 Units used in the SPARTAN code 32
3.4 Core routines 32
3.5 The Lineshape calculation routine 34
3.5.1 Calculation of a Voigt lineshape 38
3.5.2 Handling and Overlay of Individual Lineshapes 42

4 Modifying the Code Spectral Database **45**
4.1 Introduction . . . 45
4.2 Building spectral datafiles for diatomic transitions . . . 46
4.2.1 Guidelines for the selection of appropriated spectral constants . . . 46
4.2.2 Step-by-step instructions . . . 50
4.2.3 Special case for Homonuclear/Fermion transitions . . . 55
4.2.4 Testing your files . . . 55
4.3 Datafiles for diatomic species partition functions calculations . . . 56
4.3.1 Approximations considered in the population routine . . . 57
4.3.2 File structure . . . 58
4.4 Building spectral datafiles for other transitions . . . 59
4.4.1 Atomic discrete and continuum transitions . . . 59
4.4.2 Linear polyatomic discrete transitions . . . 60
4.4.3 Molecular continuum transitions . . . 62
4.5 Linking new spectral datafiles to the SPARTAN database . . . 63
4.6 Summary . . . 66

A References for the SPARTAN Spectral Database **67**

B Hönl–London Factors **71**
B.1 Applied approximations . . . 72
B.1.1 Neglecting line spin-splitting effects for satellite lines involving Σ states . . . 72
B.1.2 Neglecting weaker rotational branches . . . 72
B.2 First Rotational Lines intensities . . . 74
B.3 Intermediary a–b case Hönl-London Factors . . . 74

C Potential Energies and Wavefunctions Reconstruction **81**
C.1 Theory . . . 81
C.1.1 Recalculating potentials for an arbitrary rotational excitation . . . 83
C.1.2 Expressions for Radiative transition probabilities . . . 84
C.1.3 Numerical Routines Description . . . 85

D Other Auxiliary Routines **87**

Bibliography **88**

E Code Versions Log **95**
E.1 Next Version updates . . . 96
E.2 Code Regressions . . . 96
E.3 Code Run Times . . . 96

F Selected Published Works **99**

Introduction

The SPARTAN code (**S**imulation of **P**lasm**A** **R**adiation in **T**hermodyn**A**mic **N**onequilibrium) is a line-by-line numerical code which calculates the spectral-dependent emission and absorption coefficients of a gas which can be either in thermodynamic equilibrium or not. In it's present version, the code is written in the MATLAB language. A FORTRAN version of the code is in the works.

The numerical code has been initially focused for the simulation of low-pressure, high-temperature plasma applications in aerospace applications (simulation of planetary atmospheric entry radiation). However, the code can and has been applied to a variety of different applications, as for example the simulation of radiation from atmospheric and low-pressure plasma sources. Last but not least, the code can be applied to the simulation of atmospheric opacities, the simulation of radiation from combustion processes, or even other applications.

The code can be operated in two different fashions:

- coupled to a fluid dynamics code, which calculates the local macroscopic properties of the flow, and handles them to the SPARTAN code. The SPARTAN code is in turn coupled to a radiative transfer code, which accounts for the calculated spectral dependent emission and absorption coefficients of the gas, and calculates radiative transfer.

- stand-alone for the simulation of the local spectral properties of gases and plasmas, or for the comparison with experimentally determined spectra, providing information on the species temperatures/energy levels distribution functions.

The second standalone application is by far the most common one, and this program manual is primarily intended at providing support with the setup of such kind of simulations.

This manual is divided in four Chapters:

- Chapter 1 gives a quick overview on how to quickly start using the code for calculating spectra, using the supplied database of the code.

- Chapter 2 describes the physical models available in the code.

- Chapter 3 provides a more detailed description of the numerical algorithms inserted in the code.
- Chapter 4 provides an in-depth description of the file structure of the SPARTAN spectral database, and explains how the database can be customized by the user.
- Appendix A references the spectral database of the SPARTAN code (except for Bound Diatomic transitions).
- Appendix B presents the expressions for the Hönl–London factors that have been inserted in the code.
- Appendix C describes the companion `RKR_SCH` routine that can be used for the calculation of the full set of rovibronic states for a specific electronic configuration of a diatomic molecule, and the calculation of Einstein coefficients for bound diatomic transitions.
- Appendix D describes the other auxiliary routines of the SPARTAN code.

Copyright Notice

The SPARTAN code is distributed under the terms of the GNU Lesser Public License (LGPL) as published by the Free Software Foundation, either version 3 of the License, or (at your option) any later versions. The LGPL license allows utilizing the SPARTAN code linked to closed-source/proprietary codes. This program is distributed to the scientific and general community in the hope that it will be useful, but without any warranty.

Community involvement in the development of the SPARTAN code itself, or its associated database, is an important endeavor for the developers and maintainers of the code. As such, we would be grateful if you would be willing to take back a little of your time and share with us any improvements of the code and/or its spectral database so that they can be further distributed among the community of SPARTAN code users. This is something that sometimes tends to be overlooked by the academic community, as much as it can avoid spurious duplication of efforts by different research teams.

As such, any sort of feedback would be welcomed by the team, who also manages an online repository of spectral data (the GASPAR database, available at http://esther.ist.utl.pt/gaspar). If you wish to have any spectroscopic data added to this ever growing open-access repository (with nearly 1,000 different sets of data), feel free to contact us.

The latest version of the SPARTAN code is maintained at the following address: http://esther.ist.utl.pt/spartan.

Chapter 1

Getting Started

This Chapter describes how the SPARTAN code can be quickly used by first-time users, relying on the provided spectroscopic database and using the default line calculation settings.

1.1 Launching the SPARTAN code

Upon starting MATLAB, the user should select the SPARTAN code directory as a working directory. Then, in the line command, one can type one of the two following instructions to start the SPARTAN code:

```
>> SPARTAN
```

or

```
>> SPARTAN_noGUI
```

The first command launches the graphical user interface (GUI) of the code, whereas the second command launches the application directly, without using the GUI.

1.1.1 Running the Graphical User Interface (GUI) of the SPARTAN code

This section will focus on the SPARTAN GUI, which provides a useful interface allowing the main calculation parameters to bet set and calculations to be launched without major efforts.

Upon launching the application, the GUI window is opened (see Fig. 1.1).

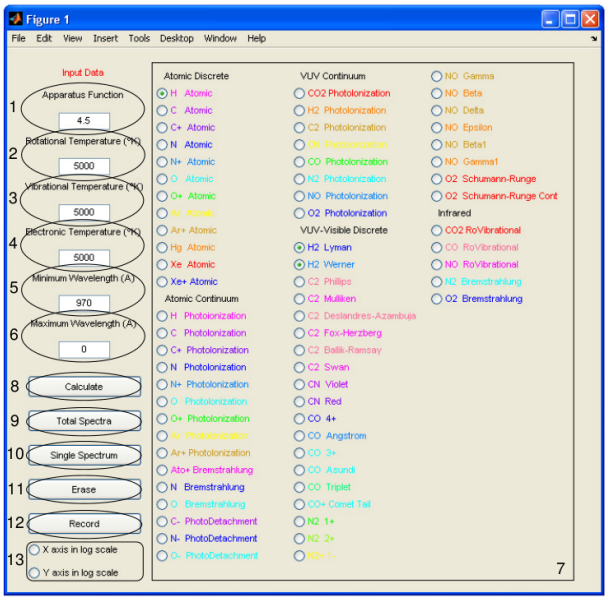

Figure 1.1: Graphical User Interface of the SPARTAN Code

The interface provides the following items which can be defined by the user:

1. **Apparatus function:** Here, the user can define a Gaussian apparatus function of a given FWHM in Å for the simulation of experimentally measured spectra. this FWHM is added to the calculated Voigt FWHM. Setting this option to 0 reproduces the "physical" spectra, for given local conditions.

2. **Rotational temperature:** The user defines here the rotational temperature for the overall species[1]. For the calculation of broadening mechanisms, the species translational temperature is considered to be equivalent to the rotational temperature[1] (T_{tr}=T_{rot}).

3. **Vibrational temperature:** The user defines here the vibrational temperature for the overall species[1].

4. **Electronic excitation temperature:** The user defines here the electronic excitation temperature for the overall species[1]. Also, the free electrons temperature is considered to be equivalent to the electronic excitation temperature[1] (T_{el}=T_{exc}).

5. **Minimum wavelength:** The user defines the minimum wavelength for which the calculation is to be carried. If the maximum wavelength parameter is set to 0, this parameter is overridden and the overall spectra is calculated.

6. **Maximum wavelength:** The user defines the maximum wavelength for which the calculation is to be carried. If this parameter is set to 0, the overall spectra is calculated.

7. **Transitions database:** The user selects the radiative transitions which are to be calculated.

8. **Calculate:** Launches the calculation.

9. **Total spectra:** After the calculation is finished, this button reproduces the overall spectra over the spectral range defined in boxes 5 and 6 (Minimum Wavelength and Maximum Wavelength). Setting a new minimum and/or maximum wavelength and pressing the Total Spectra button will reshape the graphical window to this new limits.

10. **Single spectrum:** After the calculation is finished, this button reproduces each radiative spectra with it's associated color, over the spectral range defined in boxes 5 and 6 (Minimum Wavelength and Maximum Wavelength). Setting a new minimum and/or maximum wavelength and pressing the Single Spectrum button will reshape the graphical window to this new limits.

11. **Erase:** This button cleans the graphical window.

12. **Record:** This button records the overall spectra (`IE_IA_nu_Total.txt`), and each radiative system spectra (`IE_IA_nu_01..i.txt`) in the `OUTPUTS` directory. Each ASCII textfile contains columnwise values of the wavenumber, emission coefficient, and absorption coefficient.

[1] The code can however consider different internal modes temperatures for each species, see chapter 3.

13. **X and Y axis scale:** These two buttons allow the user to switch between linear to logarithmic scales for both the X and Y axis.

Note that besides setting these parameters in the code GUI, the user must define the local number density of the different species present in the simulated gas. These values must be changed by the user in the `Inputs.txt` file in the code `INPUTS` subdirectory.

1.1.2 How the Graphical User Interface works

The SPARTAN code GUI has been built as an upper layer to the core version of the SPARTAN code (`SPARTAN_noGUI`). The SPARTAN code receives it's calculation parameters from the file `Inputs.txt` (besides it's other associated files –`Database.txt` and `Lineshape.txt`– which will be further discussed in chapter 3). The GUI commands merely updates the values of the `Inputs.txt` file, without any interaction with the core of the SPARTAN code. Therefore, this GUI can be straightforwardly overridden for coupled calculations using the SPARTAN code and other numerical codes.

1.1.3 Other user-defined parameters

Besides the parameters modified through the GUI, and the local species densities (in units of particle/m^3) that have to be input in the file `Inputs.txt`, many other parameters maybe adjusted by the user of the code. However these imply a more detailed knowledge on the structure of the code and are discussed in Chapter 3.

1.1.4 Running the SPARTAN code without the Graphical User Interface

When using the SPARTAN code without using the program GUI, the user must manually set the input parameters in the `Inputs.txt` file, record the changes, and launch the calculation in the MATLAB command line by typing `>> SPARTAN_noGUI`. Upon the calculation end, the code records the overall spectra (`IE_IA_nu_Total.txt`), and each radiative system spectra (`IE_IA_nu_01..i.txt`) in the `OUTPUTS` directory.

1.2 Recorded data

Each ASCII textfile for the the overall spectra (`IE_IA_nu_Total.txt`), and each radiative system spectra (`IE_IA_nu_01..i.txt`) contains columnwise values of the emission coefficient (in W/m^3-cm^{-1}-sr), absorption coefficient (in m^{-1}), and wavenumber (in cm^{-1}). Also, the code displays some of the calculation overall results, like the spectrum total radiative power, the radiative power of each radiative transition, and the overall calculation time. Such parameters are also recorded in the file `Calc\_Log.txt`, located in the `OUTPUTS` directory, overriding any older logfile encountered in this directory.

Note that both versions of the code also leave the calculation parameters (variables `Inputs`, `Reference`, `Species`, and `Transitions`) and results (vari-

ables `Result` for each radiative transition spectra, and `ResultTotal` for the overall radiative spectra) in the MATLAB workspace.

1.3 Sample comparisons

A few supplied test routines showcase the capabilities of the SPARTAN code for reproducing experimental spectra, and performing large scale spectral computations.

Inside the `TESTS` directory there are several directories with a matlab executable each. These contain:

- A Simulation of the C_2 $\Delta v = 0$ Swan Bands, using the routine for the simulation of ${}^3\Pi - {}^3\Pi$ transitions for homonuclear molecules, and comparison with an experimental spectrum.
- A Simulation of the CN Violet $\Delta v = 0$ System, using the routine for the simulation of ${}^1\Sigma - {}^1\Sigma$ transitions for heteronuclear molecules, and comparison with an experimental spectrum.
- A Simulation of the H_2 Lyman & Werner bands, using the routine for the simulation of ${}^1\Sigma - {}^1\Sigma$ and ${}^1\Pi - {}^1\Sigma$ transitions for homonuclear molecules, and comparison with an experimental spectrum.
- A Simulation of the N_2 1^{st} Negative $\Delta v = 0$ System, using the routine for the simulation of ${}^2\Sigma - {}^2\Sigma$ transitions for homonuclear molecules, including the effects of rotational perturbations, and comparison with an experimental spectrum.
- A Simulation of the NO Rovibrational $\Delta v = 0$ Transitions, using the routine for the simulation of ${}^2\Pi - {}^1\Pi$ transitions for heteronuclear molecules, and comparison with an experimental spectrum.
- A Simulation of a full VUV–IR spectrum for Air at 1 bar mixture in full thermochemical equilibrium at 1,000K and 6,000K.
- A Simulation of a full VUV–IR spectrum for a 97% CO_2–3% N_2 1 bar mixture in full thermochemical equilibrium at 1,000K, 5,000K, and 10,000K.

An excel file (`CO2N2_RadPower.xls`) is also included, providing the integrated radiative intensity of a 97% CO_2–3% N_2 mixture at 1bar and 4,300Pa.

1.4 Stepping a little further

This chapter has dealt with the essentials for a quick launch of the line-by-line code SPARTAN, using its graphical interface. For the more detailed description of the physical models implemented in the code, please refer to Chapter 2. For a detailed description of the SPARTAN code structure and routines, please refer to Chapter 3. For the information on how to customize the code for your specific needs, please refer to Chapter 4.

Chapter 2

Physical Models

$$H\Psi = E\Psi$$

Schrödinger's Equation

This Chapter provides an abridged description of the theoretical and numerical quantum models that have been implemented in the SPARTAN code. The Chapter is split into three sections, which respectively describe the implemented theoretical models for the calculation of discrete radiation, the calculation of continuum radiation, and the generalized relationships between emission/absorption coefficients.

2.1 Discrete radiation models

The theory of discrete atomic and diatomic transitions is shortly summarized in this section, starting with the selection rules, which indicate which radiative transitions are allowed between the species different internal levels, followed by the description of the models utilized for the calculation of line positions, intensities, and shapes.

2.1.1 Selection rules

2.1.1.1 Atomic transitions

Atomic transitions are split into electric/magnetic dipolar or quadrupolar transitions. The transitions can be classified by order of decreasing intensity: dipolar electric E1, quadrupolar electric E2, dipolar magnetic M1, and quadrupolar magnetic M2. E1 transitions are called "allowed transitions", the others "forbidden transitions". The selection rules [2] are summarized in Table 2.1

2.1.1.2 Diatomic transitions

Only electric dipolar transitions are considered for the calculation of synthetic discrete spectra from diatomic species, as the other type of transitions have much lower probabilities and are generally covered by this stronger spectra.

	Transitions E1	Transitions M1	Transitions E2
		All couplings	
1	$\Delta J = 0, \pm 1$ (except $0 \nleftrightarrow 0$)	$\Delta J = 0, \pm 1$ (except $0 \nleftrightarrow 0$)	$\Delta J = 0, \pm 1, \pm 2$ (except $0 \nleftrightarrow 0$, $\frac{1}{2} \nleftrightarrow \frac{1}{2}$,$1 \nleftrightarrow 1$)
2	$\Delta M = 0, \pm 1$ (except $0 \nleftrightarrow 0$ when $J = 0$)	$\Delta M = 0, \pm 1$ (except $0 \nleftrightarrow 0$) when $J = 0$)	$\Delta M = 0, \pm 1, \pm 2$
3	parity change	identical parity	identical parity
4[1]	one electron transition with $\Delta l = \pm 1$, for arbitrary Δn	no electronic configuration change, i.e. for all electrons: $\Delta l = 0$, $\Delta n = 0$	no electronic configuration change, i.e. for one electron: $\Delta l = 0, \pm 2$, Δn arbitrary
		L–S Coupling	
5	$\Delta S = 0$	$\Delta S = 0$	$\Delta S = 0$
6	$\Delta L = 0, \pm 1$ (except $0 \nleftrightarrow 0$)	$\Delta L = 0$, $\Delta J = \pm 1$	$\Delta L = 0, \pm 1, \pm 2$ (except $0 \nleftrightarrow 0$, $0 \nleftrightarrow 1$)

Table 2.1: Selection rules for atomic transitions

The overall rotational lines of for the transitions between upper (e', v', J') and lower (e'', v'', J'') levels which share the same ΔN and ΔJ are written as:

$$^{\Delta N}\Delta J_{i,j}$$

where i and j stand for the index of the upper and lower states multiplet components. Since for an electric dipolar transition we have $i = j$, the branches with $\Delta J = \Delta N$ are called "main branches", whereas the branches with $\Delta J \neq \Delta N$ are called "satellite branches". The nomenclature for the different branches is summarized in Table 2.2

	N	O	P	Q	R	S	T
ΔJ			-1	0	1		
ΔN	-3	-2	-1	0	1	2	3

Table 2.2: Nomenclature for the different rotational branches

For diatomic transitions, three levels of coupling rules have to be accounted for:

1. General selection rules
2. Selection rules for molecular angular momentum coupling Hünd Case a
3. Selection rules for molecular angular momentum coupling Hünd Case b[2]

We define the notations e and f which allow identifying a level parity. For a integer rotational quantum number J we note e as the parity level $(-1)^J$ and f the parity level $-(-1)^J$. For a half-integer rotational quantum number J we note e as the parity level $(-1)^{J-\frac{1}{2}}$ and f the parity level $-(-1)^{J-\frac{1}{2}}$.

The general selection rules for diatomic dipolar transitions have been summarized by Herzberg [3], and are reported in table 2.3.

For the a et b Hünd cases, both Λ and S quantum numbers are defined, and the following selection rules are observed:

$$\begin{aligned} \Delta\Lambda &= 0, \pm 1 \\ \Delta S &= 0 \end{aligned} \tag{2.1}$$

additionally, for a $\Sigma \leftrightarrow \Sigma$ transition we have

$$\begin{aligned} \Sigma^+ \leftrightarrow \Sigma^+, \Sigma^- \leftrightarrow \Sigma^- \quad &\text{allowed} \\ \Sigma^+ \leftrightarrow \Sigma^- \quad &\text{forbidden} \end{aligned} \tag{2.2}$$

For the a Hünd case, the quantum number Σ (not to be confused with the electronic state Σ such that $\Lambda = 0$) is also defined. If both initial and final states of the transition belong to Hünd case a, we have the selection rule

[2]Other very specific coupling cases also exist but are not considered in the code

transition between rotational levels	$\Delta J = 0, \pm 1$ (except $0 \nleftrightarrow 0$)
parity of the rotational levels	$+ \leftrightarrow -$ allowed $+ \nleftrightarrow +, - \nleftrightarrow -$ forbidden
rotational branches $Q(\Delta J = 0)$	$e \leftrightarrow f$ allowed $e \leftrightarrow e, f \leftrightarrow f$ forbidden
rotational branches $P, R(\Delta J = \pm 1)$	$e \leftrightarrow e, f \leftrightarrow f$ allowed $e \nleftrightarrow f$ forbidden
homonuclear molecules	$s \leftrightarrow s, a \leftrightarrow a$ allowed $s \nleftrightarrow a$ forbidden
same charge cores	$g \leftrightarrow u$ allowed $g \leftrightarrow g, u \leftrightarrow u$ forbidden

Table 2.3: Selection rules for diatomic electric dipolar transitions

$$\Delta\Sigma = 0 \tag{2.3}$$

accounting for selection rules (2.1) and (2.2) we obtain the selection rule:

$$\begin{aligned} &\Delta\Omega = 0, \pm 1 \\ &\Delta J = 0 \quad \text{forbidden for} \quad \Omega = 0 \leftrightarrow \Omega = 0 \end{aligned} \tag{2.4}$$

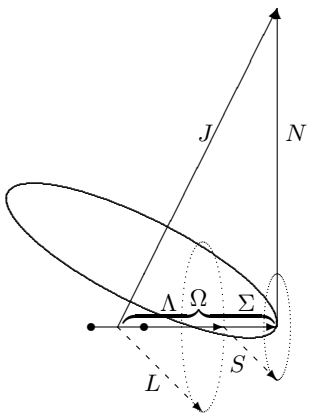

Figure 2.1: Hünd case a vector diagram

For the b Hünd case, the quantum number Σ is no longer defined. If both initial and final states of the transition both belong to Hünd case b, we have the selection rule

$$\Delta N = 0, \pm 1$$
$$\Delta N = 0 \quad \text{forbidden for} \quad \Sigma \leftrightarrow \Sigma \tag{2.5}$$

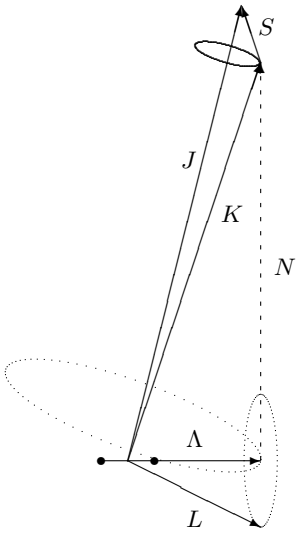

Figure 2.2: Hünd case b vector diagram

2.1.1.3 Linear Polyatomic transitions

In addition to the same rules considered for diatomic transitions ($\Delta J = 0, \pm 1$, etc..) we observe the additional vibrational selection rules:

1. $\Delta v_2 + \Delta v_3$ odd and $\Delta \ell_2 = \pm 1$ for perpendicular bands;
2. $\Delta v_2 + \Delta v_3$ odd and $\Delta \ell_2 = 0$ for parallel bands.

2.1.2 Line positions and intensities

Discrete atomic and molecular spectra are composed of a collection of lines which can be defined by three specific parameters:

1. Line position: $\overline{\nu} = (E_u - E_l)/h$
2. Line intensity[3]: $\varepsilon = N_u A_{ul} \Delta E_{ul}/4\pi$
3. Line profile: $F(\overline{\nu} - \overline{\nu}_0)$

This section outlines the theoretical models that are implemented for the production of a line database with these three parameters.

[3] absorption coefficients are determined from the emission coefficients according to Kirchoff–Planck Law

2.1.2.1 Atomic transitions

Atomic line transition lists are typically compiled into comprehensive databases providing the line center positions $\overline{\nu}_0$, the upper and lower energy level energies and degeneracies E_u, g_u, E_l, g_l, and the transition Einstein coefficients A_{ul}.

2.1.2.2 Diatomic transitions

For diatomic transitions, the procedure of calculating the level energies and transition probabilities is slightly more complex, due to the additional degrees of freedom from molecular vibrational and rotational motion. As such, for each electronic state of a molecule corresponds a set of vibration and rotational levels. Following the Born–Oppenheimer approximation, the electronic, vibration and rotational energies may be usually separated so that the total internal wave function of the molecule may be decoupled in three wave functions grouping the electronic, vibration and rotation terms:

$$\psi = \psi_{el} \times \psi_{vib} \times \psi_{rot} \tag{2.6}$$

Line Positions

Following Eq. 2.6, the total energy of a specific diatomic level is split into an electronic, vibrational and rotational term:

$$E_{e,v,J} = E_{el} + E_{vib} + E_{rot} \tag{2.7}$$

with

$$E_{el} \gg E_{vib} \gg E_{rot} \tag{2.8}$$

These level energies correspond to the solutions of the Schrödinger equation for an anharmonic oscillator and a distorted rotator, represented by a series of polynomial expansions:

$$\begin{aligned} E_{e,v,J} &= T(e) + G(v) + F_v(J) \\ &= T(e) + \omega_e \left(v + \frac{1}{2}\right) - \omega_e x_e \left(v + \frac{1}{2}\right)^2 + \omega_e y_e \left(v + \frac{1}{2}\right)^3 + \cdots \\ &\quad + B_v(J(J+1)) - D_v(J(J+1))^2 + H_v(J(J+1))^3 + \cdots \end{aligned} \tag{2.9}$$

These expressions can be presented in a more compact form replacing the different spectroscopic constants by a Dunham matrix such that:

$$E_{e,v,J} = \sum_{i,j} Y_{ij} \left(v + 1/2\right)^i \left[F(J)\right]^j, \tag{2.10}$$

This formalism is consistent with Zare's effective Hamiltonian [4]. The correspondence between traditional spectroscopic expressions and the Dunham coefficients is then given by:

$$G(v) = \sum_{i=0,\dots} Y_{i0}\left(v+\frac{1}{2}\right)^i = T(e) + \omega_e\left(v+\frac{1}{2}\right) - \omega_e x_e\left(v+\frac{1}{2}\right)^2 + \omega_e y_e\left(v+\frac{1}{2}\right)^3 + \dots \tag{2.11a}$$

$$B_v = \sum_{i=0,\dots} Y_{i1}\left(v+\frac{1}{2}\right)^i = B_e - \alpha_e\left(v+\frac{1}{2}\right) + \gamma_e\left(v+\frac{1}{2}\right)^2 + \dots \tag{2.11b}$$

$$D_v = -\sum_{i=0,\dots} Y_{i2}\left(v+\frac{1}{2}\right)^i = D_e + \beta_e\left(v+\frac{1}{2}\right) + \dots \tag{2.11c}$$

$$H_v = \sum_{i=0,\dots} Y_{i3}\left(v+\frac{1}{2}\right)^i, \dots$$

$\dots$

Energies for fine-structure levels

When spin-splitting is considered, we need to introduce the constants A_v for spin-orbit interactions, γ_v for spin-rotation interactions, and λ_v for spin-spin interactions. The vibrational dependence of these constants is expressed in the usual way:

$$[A,\lambda,\gamma]_v = \sum_0^i [A,\lambda,\gamma]_i\left(v+\frac{1}{2}\right)^i \tag{2.12}$$

We will now present the different equations for the level energies.

For general doublet states [5]:

$$F_{3/2}(J\geq 1) = B_v\left[\begin{array}{l}\left(J+\frac{1}{2}\right)^2-\Lambda^2 \\ -\frac{1}{2}\left(4\left(J+\frac{1}{2}\right)^2+Y_v(Y_v-4)\Lambda^2\right)^{\frac{1}{2}}\end{array}\right] - D_v J^4 \tag{2.13a}$$

$$F_{1/2}(J\geq 0) = B_v\left[\begin{array}{l}\left(J+\frac{1}{2}\right)^2-\Lambda^2 \\ +\frac{1}{2}\left(4\left(J+\frac{1}{2}\right)^2+Y_v(Y_v-4)\Lambda^2\right)^{\frac{1}{2}}\end{array}\right] - D_v(J+1)^4 \tag{2.13b}$$

For $^2\Sigma$ states [3]:

$$^2\Sigma_{3/2}(J \geq 1) = B_v(J(J+1)) - D_v(J(J+1))^2 + \gamma_v \left(\frac{J}{2}\right) \tag{2.14a}$$

$$^2\Sigma_{1/2}(J \geq 0) = B_v(J(J+1)) - D_v(J(J+1))^2 - \gamma_v \left(\frac{J+1}{2}\right) \tag{2.14b}$$

For $^3\Sigma$ states the energy levels expression is given by [6] from the formulation of [7] with a typographic correction from [8]. This expression is deemed more accurate than the general expression from [3]. The expressions read:

$$\begin{aligned} ^3\Sigma_2(J \geq 2) = {} & B_v(J(J+1)) - D_v(J(J+1))^2 - \left(\lambda_v - B_v + \tfrac{1}{2}\gamma_v\right) \\ & - \left[\left(\lambda_v - B_v + \tfrac{1}{2}\gamma_v\right)^2 + 4J(J+1)\left(B_v - \tfrac{1}{2}\gamma_v\right)^2\right]^{\frac{1}{2}} \end{aligned} \tag{2.15a}$$

$$^3\Sigma_1(J \geq 1) = B_v(J(J+1)) - D_v(J(J+1))^2 \tag{2.15b}$$

$$\begin{aligned} ^3\Sigma_0(J \geq 0) = {} & B_v(J(J+1)) - D_v(J(J+1))^2 - \left(\lambda_v - B_v + \tfrac{1}{2}\gamma_v\right) \\ & + \left[\left(\lambda_v - B_v + \tfrac{1}{2}\gamma_v\right)^2 + 4J(J+1)\left(B_v - \tfrac{1}{2}\gamma_v\right)^2\right]^{\frac{1}{2}} \end{aligned} \tag{2.15c}$$

The expression for the $^3\Pi$ levels is given by [9]:

$$^3\Pi_2(J \geq 2) = B_v \begin{bmatrix} J(J+1) - \sqrt{y_1 + 4J(J+1)} \\ -\frac{2}{3}\frac{y_2 - 2J(J+1)}{y_1 + 4J(J+1)} \end{bmatrix} - D_v\left(J - \frac{1}{2}\right)^4 \tag{2.16a}$$

$$^3\Pi_1(J \geq 1) = B_v\left[J(J+1) + \frac{4}{3}\frac{y_2 - 2J(J+1)}{y_1 + 4J(J+1)}\right] - D_v\left(J + \frac{1}{2}\right)^4 \tag{2.16b}$$

$$^3\Pi_0(J \geq 0) = B_v \begin{bmatrix} J(J+1) + \sqrt{y_1 + 4J(J+1)} \\ -\frac{2}{3}\frac{y_2 - 2J(J+1)}{y_1 + 4J(J+1)} \end{bmatrix} - D_v\left(J + \frac{3}{2}\right)^4 \tag{2.16c}$$

with

$$y_1 = Y_v(Y_v - 4) + \frac{4}{3} \qquad y_2 = Y_v(Y_v - 1) - \frac{4}{9} \qquad Y_v = \frac{A_v}{B_v}$$

These expressions are also consistent with Zare's effective Hamiltonian [4], and one should be careful enough to select spectroscopic constants that have been fitted to such formalism. If spectroscopic constants fitted to other formalisms are selected, they should be converted to Zare's effective Hamiltonian prior to insertion in the code. Table 2.4, reported from Ref. [10] presents the correspondence between spectroscopic constants fitted to Zare's Hamiltonian and Brown's Hamiltonian [11], which is also popular among spectroscopists.

Line Intensities

The intensity of one line will depend on the energy of the transition, the population of the excited level, and the transition probability, described by its

Brown	Zare
A	$A^Z - 1/8\frac{A^Z}{B^Z}p$
B	$B^Z + 1/2q$
D	D
H	H
γ	$\gamma^Z - 1/2p$
p	p
q	q
D_p	$D_{p+2q} - 2D_q$
D_q	D_q
H_p	$H_{p+2q} - 2H_q$
H_q	H_q

Table 2.4: Spectroscopic constants correspondence for Brown's and Zare's Hamiltonians

Einstein coefficient A_{ul}. Here we will describe the method for the calculation of such parameter.

Although we admit the separability of the electronic, vibrational and rotational modes of a molecule, according to the Born–Oppenheimer approximation, electronic and vibrational configurations are intrinsically connected through the different potential curves, and there is also a coupling between the molecular rotational motion and the electronic cloud of the molecule due to the electrons spin movement. The transition probability A_{ul} can then be decomposed as a product:

$$A_{ul} = A^{e'v'}_{e''v''} \cdot A^{\Lambda'J'}_{\Lambda''J''}$$

The vibronic component $A^{e'v'}_{e''v''}$ can then be expressed as a function of the vibronic transition moment $R_e^{v'v''}$ using the following expression (in atomic units, using wavenumber $\overline{\nu}$ units over frequency ν units[4]:

$$A^{e'v'}_{e''v''} = \frac{64\pi^4\overline{\nu}^3}{3hc^3}\frac{(2-\delta_{0,\Lambda'+\Lambda''})}{(2-\delta_{0,\Lambda'})}\left(R_e^{v'v''}\right)^2$$

As the vibronic transition moment $\left(R_e^{v'v''}\right)^2$ cannot usually be resolved for each multiplet transition, an average transition moment value $\sum\left(R_e^{v'v''}\right)^2$ is rather used. We then have:

$$\left(R_e^{v'v''}\right)^2 \cong \frac{\sum\left(R_e^{v'v''}\right)^2}{(2-\delta_{0,\Lambda'+\Lambda''})(2S+1)} \tag{2.17}$$

The vibronic transition moment is calculated using the electronic transition moment $R_e(r)$ which is taken from the literature, and the upper and lower

[4]The term $4\pi\epsilon_0$ has an unit value in atomic units and hence does not appear explicitly in the expression

states vibrational wavefunctions ψ which can be obtained by solving the radial time-independent Schrödinger equation over recalculated potentials. This is carried out by a companion routine of the SPARTAN code (RKR_SCH) which is described in appendix C. The relationship allowing to calculate the vibronic transition moment for each upper/lower state pair reads as:

$$\left(R_e^{v'v''}\right)^2 = \left(\int \psi_{v'}(r) R_e(r) \psi_{v''}(r) dr\right)^2 \tag{2.18}$$

The rotational transition probability is in turn given by the different theoretical Hönl–London factors, which depend on the transition upper and lower electronic states types (${}^n\Lambda \leftrightarrow {}^n\Lambda$) and the Hünd coupling case:

$$A^{\Lambda' J'}_{\Lambda'' J''} = \frac{S^{\Lambda' J'}_{\Lambda'' J''}}{2J'+1}$$

Using the normalization rule:

$$\sum_{J''} S^{\Lambda' J'}_{\Lambda'' J''}(J') = (2J'+1)$$

we then have:

$$A_{ul} = \frac{64\pi^4 \overline{\nu}^3}{3hc^3} \frac{\sum \left(R_e^{v'v''}\right)^2}{(2-\delta_{0,\Lambda'})(2S+1)} \frac{S^{\Lambda' J'}_{\Lambda'' J''}}{2J'+1} \tag{2.19}$$

The analytic expressions for the Hönl–London factors considered in the SPARTAN code are presented in appendix B.

Modeling of perturbations in the spectra

Perturbations in the spectrum can either affect the electronic states rotationless potential curves (avoided crossings), or affect the potential curves at a given rotational quantum number (also avoided crossings). In the first case, the vibrational-specific constants are modified after a given threshold vibrational number, but this can be easily accounted for by using vibrationally-specific spectroscopic constants (B_v, D_v, etc...). For the case of rotational perturbations, one can either resort to a complex approach of solving the perturbed system Hamiltonian to yield the perturbed energy levels (see for example ref. [12]), or the perturbation can be simply approached by an expression of the type $1/x$ (see [3] pp. 283). In the SPARTAN code we have chosen this more simplified approach, applying the equation:

$$E_J = E_J + \frac{\Delta E_{max}}{2\left(J - J_{pert} - 1/2\right)} \tag{2.20}$$

and using supplied values for ΔE_{max} and J_{pert}. The splitting of the exact perturbed level in two different sub-levels is neglected.

2.1.2.3 Linear Polyatomic transitions

The procedure for the calculation of linear polyatomic transitions (inserted in the SPARTAN code due to the importance of CO_2 IR radiation), is quite similar to the one for diatomic transitions.

The emission coefficient is obtained as:

$$\varepsilon_{\overline{\nu}} = \frac{1}{4\pi} N_{v'J'} A_{v'v''} S^{\ell' J'}_{\ell'' J''} F_{J'J''} h\overline{\nu} \tag{2.21}$$

where the additional term $F_{J'J''}$ stands for the Hermann–Wallis factors, which describe the interactions between the vibrational and rotational modes. (see [3], p. 110).

The Einstein coefficient $A_{v'v''}$ for a purely vibrational transition is expressed as a function of the square of the vibrational transition moment $(R_{v'v''})^2$ according to the relationship

$$\begin{aligned} A_{v'v''} &= \frac{64\pi^4}{3hc^3} \nu^3_{v'v''} \frac{(2-\delta_{0,\ell'})}{(2-\delta_{0,\ell''})} (R_{v'v''})^2 \\ &= 2.026 \cdot 10^{-6} \overline{\nu}^3_{v'v''} \frac{(2-\delta_{0,\ell'})}{(2-\delta_{0,\ell''})} (R_{v'v''})^2 \end{aligned} \tag{2.22}$$

Since the numerical evaluation of the parameter $(R_{v'v''})^2$ is quite complex, it is customary to instead present the integrated intensity $S^{\circ}_{v'v''}$ for a specific vibrational band, calculated at a reference temperature T_0 (usually 296K) [13]. The value of the dipolar moment (in atomic units $(ea_0)^2$) can then be determined from this parameter according to the relationship [14, 15]:

$$(R_{v'v''})^2 I_a = \frac{3hc}{8\pi^3} 10^{43} \frac{S^{\circ}_{v'v''}}{\overline{\nu}_{v'v''}} \frac{Q^{\circ}_v}{(2-\delta_{0,\ell''}) \exp\left(-\frac{hcE_{v'}}{k_B T_0}\right)} \frac{(ea_0)^2}{D^2} \tag{2.23}$$

The Hönl–London factors for these kind of linear vibrational transitions are given by Ref. [16] and are presented in table 2.5:

	$\Delta\ell = 0$	$\Delta\ell \neq 0$
P	$\frac{(J''+\ell'')(J''-\ell'')}{J''}$	$\frac{(J''-1-\ell''\Delta\ell)(J''-\ell''\Delta\ell)}{2J''}$
Q	$\frac{(2J''+1)\ell''^2}{J''(J''+1)}$	$\frac{(J''+1+\ell''\Delta\ell)(J''-\ell''\Delta\ell)(2J''+1)}{2J''(J''+1)}$
R	$\frac{(J''+1+\ell'')(J''+1-\ell'')}{J''+1}$	$\frac{(J''+2+\ell''\Delta\ell)(J''+1+\ell''\Delta\ell)}{2(J''+1)}$

Table 2.5: Hönl–London factors for parallel and perpendicular rovibrational transitions of linear polyatomic molecules

Lastly, the Herman–Wallis factors can be expressed as a function of the following polynomial expressions:

P branch: $(1 - A_1 J'' + A_2 J''^2 - A_3 J''^3)^2$
Q branch: $(1 + A_Q J''(J''+1))^2$
R branch: $(1 + A_1(J''+1) + A_2(J''+1)^2 + A_3(J''+1)^3)^2$

The values for each coefficient $A_{1,2,3,Q}$ being tabulated for each vibrational band.

2.1.3 Broadening mechanisms

Broadening mechanisms lead to the broadening of the initial transition Dirac to a line following a specific shape. Broadening mechanisms can be split into two different categories:

- Broadening from atomic and molecular collisions, described by a Lorentz shape
- Broadening from Doppler effects, described by a Doppler shape

"Universal" expressions are presented in this section. Some of these expressions are in general approximate, but should suffice for the level of detail needed for the typical applications of the SPARTAN code, proving flexible enough for allowing an automated calculation of each transition broadening widths. All broadening width units are presented in wavenumber units [cm^{-1}], with the species densities in [cm^{-3}].

2.1.3.1 Collisional broadening mechanisms

Collisional broadening processes are described through a Lorentzian line profile such that:

$$\ell(\overline{\nu}) = \frac{1}{1 + 4\left(\frac{\overline{\nu}-\overline{\nu}_0}{\Delta\overline{\nu}_L}\right)^2} \tag{2.24}$$

The convolution of different Lorentz line profiles also yields a Lorentz line profile such that $(\Delta\overline{\nu}_L)_{tot} = \sum(\Delta\overline{\nu}_L)_i$.

Natural broadening: The linewidth depends on the radiative lifetime τ according to the following expression:

$$\Delta\overline{\nu}_N = \frac{1}{4\pi c\tau} \tag{2.25}$$

This broadening mechanism is generally very small, and has accordingly been neglected in the SPARTAN code. For example, a radiative lifetime of 1 ns yields $\Delta\overline{\nu}_N = 0.005\ \mathrm{cm}^{-1}$.

Pure collisional broadening: This process stems from the rate of collisions between the different particles in the gas. The equivalent width has the following expression:

$$\Delta\overline{\nu}_C = \frac{2\nu_{col}}{c} \tag{2.26}$$

with

$$\nu_{col} = \frac{10^6}{N_i}\sum_j N_i N_j \pi \left(r_i[\mathrm{m}] + r_j[\mathrm{m}]\right)^2 \sqrt{\frac{8k_B}{\pi}\mu_{i,j}} \tag{2.27}$$

Resonance broadening: This broadening mechanism is confined to the electric dipolar atomic and molecular lines (resonance lines). An expression adapted from [17] is used. In its current version, the SPARTAN code assumes all its database lines as electric dipolar and as such applies this broadening mechanism to all its database.

$$\begin{aligned} \Delta\lambda_R &= 1.2893 \cdot 10^{-45} \left(\frac{g_u}{g_l}\right)^{\frac{1}{2}} A_{ul} \lambda^2 \lambda_R^3 N_g \\ \Leftrightarrow \quad \Delta\overline{\nu}_R &= 1.2893 \cdot 10^{-13} \left(\frac{g_u}{g_l}\right)^{\frac{1}{2}} A_{ul} \frac{1}{\overline{\nu}_R^3} N_g \end{aligned} \tag{2.28}$$

Van der Waals broadening: This broadening process stems from collisions with neutral particles who do not share a resonant transition with the radiating particle. The simplified expression from [18] is preferred to the expression from [19], which is more precise but more difficult to implement:

$$\Delta\overline{\nu}_W = 20(1.6 \cdot 10^{-33} \cdot 3^4)^{\frac{2}{5}} \left(\frac{3k_B T}{m}\right)^{\frac{3}{10}} \frac{1}{c} N \tag{2.29}$$

where $m = \frac{\rho}{N}$ is the mean species mass and $N = N_e + \sum_i N_i$ the total particle density.

Stark broadening: This broadening process stems from the interaction between the external electronic shells of the radiating species and the plasma charged species. Both ions and electron can account for such a broadening process, but in practice it is the electrons who contribute the most, due to their higher kinetic speeds. We can therefore on a first approximation express Stark broadening as a function of electronic density and temperature. Theoretical expressions for the calculation of Stark broadening are not available, except for hydrogenoïd species [18]. Tabulated values providing the parameter $\Delta\lambda_S$ as a function of n_e and T_e are used [19]:

$$\Delta\lambda_S = f(T_e) \frac{N_e}{10^{16}} \tag{2.30}$$

In its current version, the SPARTAN code totally neglects Stark broadening, due to the difficulties of implementing this broadening process in an universal fashion. Future versions of the code will likely be updated to allow for some amount of accounting for this process.

2.1.3.2 Doppler broadening

Doppler broadening profiles follow a Gaussian shape and are described by the following expression:

$$g(\overline{\nu}) = \exp\left[-4\ln 2 \left(\frac{\overline{\nu} - \overline{\nu}_0}{\Delta\overline{\nu}_G}\right)^2\right] \tag{2.31}$$

As for the Lorentzian collisional lineshapes, the same additivity rule applies for Doppler Gaussian-type lineshapes: $(\Delta\overline{\nu}_G)_{tot} = \sum(\Delta\overline{\nu}_G^2)_i$

Doppler broadening is a consequence of the thermalized motion of the radiating species. A molecule radiating at a frequency ν_0 in its own reference plane, and approaching at a velocity v from the observation plane will have a Doppler-type shift in the observation plane, such that $\nu = \nu_0 \left(1 + \frac{v}{c}\right)$. Assuming a Maxwellian velocity distribution function at a characteristic temperature T we may obtain the corresponding Doppler broadening width:

$$\Delta\overline{\nu} = \overline{\nu}_0 \sqrt{8 \log 2 \frac{k_B T}{mc^2}} \tag{2.32}$$

2.1.3.3 Voigt line profile

A Voigt profile results from the convolution of a Lorentz and Doppler/Gaussian profile such that:

$$v(x) = \ell(x) \otimes g(x) \tag{2.33}$$

$$= \frac{\Delta\nu_L}{\Delta\nu_G} \sqrt{\frac{\ln 2}{\pi^3}} \int_{-\infty}^{+\infty} \frac{\exp\left\{-\left[(\xi - x)^2 \ln 2\right] / \Delta\nu_G^2\right\}}{\xi^2 + \Delta\nu_L^2} d\xi \tag{2.34}$$

$$x = \nu - \nu_0 \tag{2.35}$$

This profile cannot be analytically calculated and an approximate expression needs to be used. Here we select the expression proposed by Whiting [20][5]:

$$\begin{aligned} v(\overline{\nu}) = C_1 e^{-4 \ln 2 D^2} + \frac{C_2}{1 + 4D^2} \cdots \\ + 0.016 C_2 \left(1 - \frac{\Delta\overline{\nu}_L}{\Delta\overline{\nu}_L}\right) \left(e^{-0.4 D^{2.25}} - \frac{10}{10 + D^{2.25}}\right) \end{aligned} \tag{2.36}$$

with

$$D = \frac{\overline{\nu} - \overline{\nu}_0}{\Delta\overline{\nu}_V}$$

$$\Delta\overline{\nu}_V = \frac{1}{2}\left(\Delta\overline{\nu}_L + \sqrt{\Delta\overline{\nu}_L^2 + 4\Delta\overline{\nu}_G^2}\right)$$

$$C_1 = \frac{\left(1 - \frac{\Delta\overline{\nu}_L}{\Delta\overline{\nu}_V}\right)}{\Delta\overline{\nu}_V \left(1.065 + 0.447 \frac{\Delta\overline{\nu}_L}{\Delta\overline{\nu}_V} + 0.058 \frac{\Delta\overline{\nu}_L^2}{\Delta\overline{\nu}_V^2}\right)}$$

$$C_2 = \frac{\left(\frac{\Delta\overline{\nu}_L}{\Delta\overline{\nu}_V}\right)}{\Delta\overline{\nu}_V \left(1.065 + 0.447 \frac{\Delta\overline{\nu}_L}{\Delta\overline{\nu}_V} + 0.058 \frac{\Delta\overline{\nu}_L^2}{\Delta\overline{\nu}_V^2}\right)}$$

This expression has been critically assessed by Olivero [21] who estimated a precision with an accuracy of about 1% minimum. Olivero then proposed a

[5] with $4\ln 2$ replaced by 2.772 for numerical efficiency reasons.

modification to the Voigt linewidth parameter, improving the accuracy down to 0.02%:

$$\Delta\overline{\nu}_V = \frac{1}{2}\left(1.0692\Delta\overline{\nu}_L + \sqrt{0.86639\Delta\overline{\nu}_L^2 + 4\Delta\overline{\nu}_G^2}\right)$$

In the SPARTAN code, we retain this analytical expression over the exact convolution expression from Eq. 2.35, as it is significantly more computationally efficient, specially in view of the sheer number of lines that have to be calculated for the production of detailed spectra over a broad range.

2.2 Continuum radiation models

Continuum transitions are transitions in which one or both of the upper/lower states do not have a discrete energy, meaning that the radiation spectrum will not have a discrete structure.

Continuum radiation transitions include:

1. Photoionization/Radiative recombination reactions:

$$\begin{aligned} \mathrm{A}^{(n)+} + h\nu &\leftrightarrow \mathrm{A}^{(n+1)+} + e^- \\ \mathrm{AB}^{(n)+} + h\nu &\leftrightarrow \mathrm{AB}^{(n+1)+} + e^- \end{aligned} \tag{2.37}$$

2. Photodetachment/Photoatachment reactions:

$$\mathrm{A}^- + h\nu \leftrightarrow \mathrm{A} + e^- \tag{2.38}$$

3. Photodissociation–Dissociative Photoionization/Radiative association reactions:

$$\begin{aligned} \mathrm{AB} + h\nu &\leftrightarrow \mathrm{AB}^* \leftrightarrow \mathrm{A{+}B} \\ \mathrm{AB} + h\nu &\leftrightarrow \mathrm{AB}^* \leftrightarrow \mathrm{A}^+ + \mathrm{B} + e^- \end{aligned} \tag{2.39}$$

4. Bremsstrahlung/Inverse Bremsstrahlung reactions:

$$\begin{aligned} \mathrm{A} + e_i^- &\leftrightarrow \mathrm{A} + e_f^- + h\nu \\ \mathrm{AB} + e_i^- &\leftrightarrow \mathrm{AB} + e_f^- + h\nu \end{aligned} \tag{2.40}$$

For these reactions, which include the emission or absorption of a free electron, energy conservation allows writing (with ΔE_i the ionization energy of the atomic or molecular state):

$$h\nu = \Delta E_i + \frac{1}{2}m_e v^2 \tag{2.41}$$

which means that this kind of radiative transitions will have an energy/frequency threshold below which they will not be able to occur.

2.2.1 Transition intensities

The transition intensities are usually expressed through calculated or measured absorption cross-sections. These allow an immediate calculation of the absorption coefficient, taking into account the population for the absorbing states, and the calculation of the emission coefficient through detailed balancing, using the Planck–Kirchhoff law.

For processes 1–3, the expression for the absorption coefficient can be written as:

$$\alpha(\overline{\nu}) = \left[\sum_i N_i \sigma_i(\overline{\nu})\right]\left[1 - \exp\left(-\frac{h\nu}{k_B T_e}\right)\right] \tag{2.42}$$

provided that level-dependent $\sigma_i(\overline{\nu})$ spectral absorption cross-sections are available. Here the factor $\left[1 - \exp\left(-\frac{h\nu}{k_B T_e}\right)\right]$ allows for the subtraction of stimulated emission processes, yielding the net absorption coefficient.

In certain cases only values for the global absorption cross-sections, tabulated at different tabulated temperatures T, are available. In this case, the global absorption coefficient, for an interpolated temperature T is written as:

$$\alpha(\overline{\nu})_T = N\sigma(\overline{\nu}, T)\left[1 - \exp\left(-\frac{h\nu}{k_B T}\right)\right] \tag{2.43}$$

For free-free Bremsstrahlung transitions (process 4), the absorption cross-section is written as:

$$\alpha(\overline{\nu}) = N_e N\sigma(\overline{\nu}, T_e)\left[1 - \exp\left(-\frac{h\nu}{k_B T_e}\right)\right] \tag{2.44}$$

2.2.1.1 Gaunt factors

A quantum correction for the classical absorption cross-section is usually proposed in the form of a so-called Gaunt factor g which will depend on the gas temperature T and the transition frequency ν. These corrective factors stem from the analysis of high density stellar plasmas. The Gaunt factor is usually close to unity. The correction to the classical absorption coefficient is simply expressed as:

$$\alpha(\overline{\nu})_{quantum} = \alpha(\overline{\nu}) \cdot g(\overline{\nu}, T_{el}) \tag{2.45}$$

The current version of the SPARTAN code accounts only for Free-Free Gaunt factors, keeping the bound-free Gaunt factor g_{bf} to unity.

The free-free Gaunt factor g_{ff} is obtained for T_{el}>1 eV(11604 K) according to the formulas proposed by Stallcop and Billman [22], who have adjusted the results from Karzas and Latter [23] in numerical form. For T_{el}<1 eV, Hummer [24] suggests considering the values provided by Menzel and Pekeris [25], who provide a good approximation of the Gaunt factor for the temperature range T_e=[150–15000K] and for the wavenumbers $\overline{\nu}$=[10–350000cm^{-1}].

2.2.2 Special cases

Special cases, in which some additional approximations or some analytical expressions are considered, are discussed in this section.

2.2.2.1 Photodetachment

Photodetachment transitions are typically modeled with the assumption that:

1. Only the ground state of the negative ion contributes for the overall absorption coefficient.
2. The negative ions ground state is in a Saha equilibrium with the neutral species ground state.

The Saha equilibrium equation becomes in this case:

$$N_{AB_0^-} = \frac{N_{AB}}{\left(\frac{2\pi\mu k_B T_{el}}{h^2}\right)^{3/2} \exp\left[-1.4388\left(E_{AB_0^-} - E_{AB}\right)\right]} \frac{Q_{AB_0^-}(T)}{Q_{el} Q_{AB}(T)} \tag{2.46}$$

with $Q_{el} = 2$ and $Q_{AB_0^-}(T) = g_{AB_0^-}$

Photodetachment absorption cross-sections are then calculated in the usual fashion:

$$\alpha(\overline{\nu})_T = N_{AB_0^-} \sigma(\overline{\nu}) \left[1 - \exp\left(-\frac{h\nu}{k_B T}\right)\right] \tag{2.47}$$

2.2.2.2 Bremsstrahlung

Some analytic expressions for the calculation of the Bremstrahlung emission/absorption cross-sections are available in the literature.

The classical emission coefficient for the Inverse Bremsstrahlung of atomic ionized species is given by Kramers [26]:

$$\varepsilon_\nu[\mathrm{J/m^3\ s\ sr\ Hz}] = \frac{8}{3}\left(\frac{2\pi}{3k_B T_e m_e}\right)^{\frac{1}{2}} \frac{\alpha^2 \left(\frac{e}{\sqrt{4\pi\epsilon_0}}\right)^6}{m_e c^3} \exp\left(\frac{hc}{k_B T_e}\overline{\nu}\right) N_e N_i \ [\mathrm{MKS}] \tag{2.48}$$

Cross-sections for the Inverse Bremsstrahlung of N and O are provided by Mjolsness and Ruppel [27]:

$$\sigma(\overline{\nu}, T_e) = 8\pi^2\sqrt{2\pi}\left(\frac{hc}{2\pi\left[\frac{e}{\sqrt{4\pi\epsilon_0}}\right]^2}\right)^2 \left(\frac{\left[\frac{e}{\sqrt{4\pi\epsilon_0}}\right]^2}{a_0} k_B T_e\right)^{\frac{3}{2}} \frac{1 + \frac{1}{2}\frac{hc}{k_B T_e}\overline{\nu}}{(hc\overline{\nu})^3} a_0^5 \sigma_0 \tag{2.49}$$

with σ_0=0.71 · 10^{-6} for O and σ_0=0.80 · 10^{-6} for N.

Tabulated N_2 and O_2 Bremstrahlung cross-sections $\sigma(\overline{\nu}, T)$ are reported in Ref. [28]

2.3 Generalized Kirchhoff–Planck Law for radiative transfer

The detailed balance principle states that in full thermodynamic equilibrium, direct and inverse reaction processes fully balance themselves. Since physical/chemical elementary processes do not depend on the thermodynamic state of the gas/plasma, one may put to use the detailed balance principle to deduce the intensity of an inverse process considering the intensity of the direct process and the expressions for the thermodynamic equilibrium of a gas. The Law relating the radiative emission/absorption coefficients is the so-called Kirchhoff–Planck Law, which will be shortly summarized for all the discrete and continuum processes described in this chapter.

2.3.1 Discrete transitions

For discrete transitions of the type $A, AB(i) \rightarrow A, AB(j)$ the general Kirchhoff–Planck Law, valid for any arbitrary population distribution of the species internal levels, yields (in frequency units):

$$\frac{\varepsilon_\nu}{\alpha(\nu)} = \frac{2h\nu^3}{c^2}\left(\frac{g_u N_l}{g_l N_u} - 1\right)^{-1} \tag{2.50}$$

In thermodynamic equilibrium conditions (with $N_i = g_i \exp(-E_i/k_B T)$), this expression becomes

$$\frac{\varepsilon_\nu}{\alpha(\nu)} = \frac{2h\nu^3}{c^2}\left[\exp\left(\frac{h\nu}{k_B T}\right) - 1\right]^{-1} \tag{2.51}$$

If we use wavenumber units $\overline{\nu}$ (cm^{-1}), the term $2h\nu^3/c^2$ in Eq. 2.50 is replaced by $2hc^2\overline{\nu}^3$. For wavelength units λ (Å), the term $2hc^2/\lambda^5$ is used.

2.3.2 Photoionization transitions

For photoionization/photodetachment processes such that $AB^{(n)+} + h\nu \rightarrow AB^{(n+1)+}$, the relationship for the bound-free $\sigma_{bf}(\nu)$ photoionization absorption cross-sections, and the free-bound $\sigma_{fb}(\nu)$ radiative recombination cross-sections is given by the Milne relations [29, 30]:

$$\frac{\sigma_{bf}(\nu)}{\sigma_{fb}(\nu)} = \frac{1}{2}\left(\frac{m_e v_e c}{h\nu}\right)^2 \frac{g_i g_e}{g_n} \tag{2.52}$$

If the electrons are thermalised and follow a Maxwell distribution function, Eq. 2.52 can be further simplified to:

$$\frac{\sigma_{bf}(\nu)}{\sigma_{fb}(\nu)} = \frac{g_i}{g_n}\frac{8k_B m_e c^2}{\pi h^2}\frac{T_e}{\nu^2} \tag{2.53}$$

The emission coefficient can then be calculated in the usual way:

$$\varepsilon_\nu = N_i N_e \sigma_{fb}(\nu)\left[1 - \exp\left(-\frac{h\nu}{k_B T_e}\right)\right] \tag{2.54}$$

Further if we have an Saha ionization equilibrium in the plasma, we can instead use the general Planck–Kirchhoff law of Eq. 2.51 for relating the emission and absorption coefficients, by simply replacing T by T_e.

2.3.3 Photodissociation transitions

For photodissociation processes such that AB(i) + $h\nu \rightarrow$ A+B, the relationship for the bound-free $\sigma_{bf}(\nu)$ and the free-bound $\sigma_{fb}(\nu)$ cross-sections is given (in wavenumber [cm^{-1}] units) by [31]:

$$\frac{\sigma_{bf}(\overline{\nu})}{\sigma_{fb}(\overline{\nu})} = \frac{(hc\overline{\nu})^2}{\mu c^2 \frac{3}{2} k_B T} \tag{2.55}$$

if we assume that the overall species translation velocities are Maxwellian. Here μ in the molecular species reduced mass, in kg units.

2.3.4 Bremsstrahlung transitions

For Bremsstrahlung transitions such that AB+e_i^- $\leftrightarrow$ AB+e_f^- + $h\nu$, if we assume that the electrons are thermalized (i.e. follow a Maxwell-Boltzmann vdf), we may define the emission/absorption coefficients detailed balance through the Planck–Kirchoff expression, proposed for the conditions of thermal equilibrium, replacing the term T by T_e:

$$\frac{\varepsilon_\nu}{\alpha(\nu)} = \frac{2h\nu^3}{c^2}\left[\exp\left(\frac{h\nu}{k_B T_e}\right) - 1\right]^{-1} \tag{2.56}$$

Chapter 3

Detailed Description of the Code

This Chapter provides a more detailed description of the code routines and their associated functions. A full summary of the SPARTAN code capabilities will be firstly presented, followed by a brief description of each of the core routines. Finally an extensive discussion of the algorithm for the `Lineshape` routine will be presented. Indeed, knowledge on the inner workings of this routine is paramount for a good understanding of the inner works of the SPARTAN code, as over 99% of the overall calculation times are spent inside this routine, which convolutes the lines lists supplied by the `Atomic1,2,3` routines into a synthetic spectrum. For a partial listing of the spectral database of the SPARTAN code, please refer to Appendix A.

3.1 Introduction

The SPARTAN code has been developed with a particular concern in providing a flexible and scalable structure. Rather than trying to provide an "authoritative" tool with its own monolithic database, it has been acknowledged that different applications will need more or less focus on different aspects of the physical models implemented in the code. We also feel that with the constant improvement of the state-of-the art in spectroscopy and modeling

of physical-chemical processes in gases an plasmas (which is still undergoing major progress at the time of this last manual update; 2013), it is important that the code structure allows place for major future upgrades. For example, progress in state-to-state modeling is likely to supersede more restrictive approximations such as considering that the different species internal modes follow a Boltzmann distribution.

With this in mind, a modular structure for the SPARTAN code has been retained. The code itself is split into an excitation and a radiative module. The excitation module is tasked with simulating the population of the different upper and lower levels of radiative transitions, handling the calculated values to the radiative module which then obtains the spectral-dependent emission and absorption coefficients through the numerical routines which implement the appropriate quantum-mechanic models. The calculation parameters are supplied by an input file which can be bypassed if the code is utilized in a coupled fashion (for example coupled to an hydro/plasma code). As stated before, a GUI layer, which is totally independent from the code itself, is also proposed. Finally, a fully-parametric spectral database is stored in a specific folder, with each transition having its own file[1].

The structure of the SPARTAN code is summarized in Fig. 3.1.

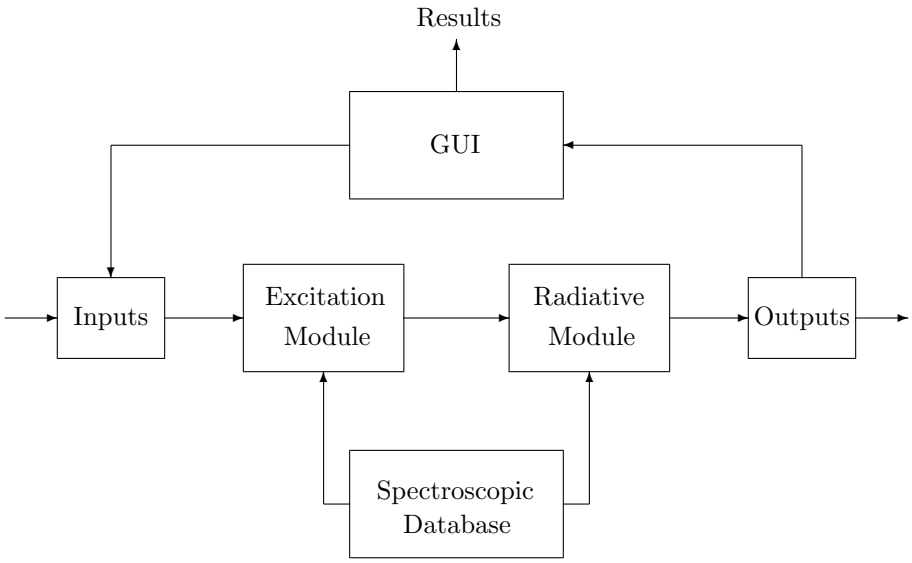

Figure 3.1: Structure of the SPARTAN Code

[1]With a small caveat in the sense that some continuum transitions, modeled by semi-empirical expressions proposed by several authors, are hard-coded instead of being in a text file

3.2 Summary of the capabilities of the SPARTAN code

The SPARTAN code has been constructed with the aim of implementing the most generalized physical models possible, trying to avoid the necessity of resorting to any approximation of any kind, specifically when it comes to the description of the thermodynamic state of the gas/plasma. A summary of the physical models and capabilities of the SPARTAN code is summarized below:

- Simulation of discrete and continuum radiative transitions from Atomic, Diatomic and Linear Triatomic molecules.
- Simulation of photoionization, photodissociation, photodetachment, and Bremstrahlung transitions for atomic (when applicable) and diatomic species. Global or level-specific cross-sections can be considered.
- Voigt lineshapes for discrete spectra, including Doppler, collisional, resonance, and van der Waals. Stark broadening is not considered at this point (lack of a general expression).
- For discrete transitions from Diatomic molecules:
  - Simulation of transitions between Σ, Π, and Δ electronic states.
  - Accounting for fine-structure transitions (singlet, doublet and triplet), except for transitions involving Δ electronic states which only can be treated as singlet transitions.
  - Accounting for Λ-doubling effects for homonuclear molecules.
  - Transitions consider the intermediate *a*–*b* Hünd case for rotational states.
  - Level energies can be calculated either by using a Dunham matrix, or with the input of vibrationally-specific spectroscopic constants.
  - Simplified treatment of rotational perturbations.
- Individual T_{rot}, T_{vib}, and T_{exc} for each species. For now we assume T_{tr}=T_{rot} and T_{el}=T_{exc}.
- Fully customizable database for the calculation of each species total partition function. Vibrational partition function sum obtained either from the truncated (at D_e) harmonic oscillator approximation or from the explicit input of levels, Vibrational partition function sum obtained from $\sum Q_J = T_{rot}/(1.4388B_v)/\sigma_{nuc}$, valid if $B_v \ll 1.4388T_{rot}$.
- Fully customizable spectral database.
- Variable spectral grid methods allowing the production of compact, yet accurate synthetic lineshapes. A multitude of parameters, such as the number of points of each Voigt lineshape, is user-parameterizable.
- De-coupled excitation and radiative modules, allowing for the direct supply of nonequilibrium level populations by associated codes.
- General non-equilibrium Planck relationship between the emission and absorption coefficients.

3.3 Units used in the SPARTAN code

This is a short outline of the units for the critical variables used in the SPARTAN code:

- Number density N (in `Inputs.txt`): m^{-3}
- Wavenumber $\overline{\nu}$: cm^{-1}
- Emission coefficient $\varepsilon_{\overline{\nu}}$: $\mathrm{W/m^3}$–cm^{-1}–sr
- Absorption coefficient $\alpha(\overline{\nu})$: m^{-1}
- Absorption cross-section $\sigma_{\overline{\nu}}$: m^3

3.4 Core routines

The core routines of the SPARTAN code are as follows:

Spectre.m is a general routine which cycles the code database, calculates the individual spectra for the requested transitions, and superposes them to yield the overall emission and absorption spectrum.

DataAtomic1,2,3.m routines read the database files for discrete atomic and molecular transitions and handle the data to the corresponding `Excite1,2,3.m` and `Atomic1,2,3.m` routines.

Excite1,2,3.m routines calculate the variables `geE`, `NeE`, `NvE`, `geG`, `NeG`, `NvG`, considering a Boltzmann equilibrium of the internal states accounting for the individual characteristic temperatures $T_{exc}, T_{vib}, T_{rot}$ of the concerned chemical species. These routines may be decoupled from the code, and general nonequilibrium populations for `geE`, `NeE`, `NvE`, `geG`, `NeG`, `NvG` may be injected by an external function or file.

Atomic1,2,3.m routines build the spectral lines database for each calculated transition. They take as an input the spectral constants from the stored database (handled by `DataAtomic1,2,3.m` inline functions of the `Spectre.m` function), the general number densities of the different species of the cell where spectral properties are being calculated (handled by `Inputs.txt` through `IORead.m` and `Spectre.m`), and the upper/lower states populations and degeneracies (variables `geE, NeE, NvE,geG, NeG, NvG`), handled by the respective `Excite1,2,3.m` functions. The routines then handle a $5 \times n$ line matrix with the 5 fundamental line parameters: line center $\overline{\nu}_0$, emission coefficient $\varepsilon_{\overline{\nu}}$, absorption coefficient $\alpha(\overline{\nu})$, Doppler FWHM $\Delta\overline{\nu}_G$ and Lorentz FWHM $\Delta\overline{\nu}_G$.

Raies1,2,3,1D,2D,3D are subfunctions of `Atomic2.m` which generate the line lists for singlet or multiplet transitions.

Photo1,2,T.m, PhoDet.m, and Bremstr.m are routines which calculate continuum spectra for respectively monoatomic photoionization, diatomic photioinization/photodissociation, atomic photodetachement, and atomic/diatomic Bremstrahlung, and yield an individual absorption spectrum. The corresponding emission spectrum is then generated inside the function `Spectre.m` using the Planck/Kirchoff relationships of Sec. 2.3.

Lineshape.m is the routine which convolves a Voigt Lineshape to the Line-data lists of Diracs supplied by the `Atomic1,2,3.m` routines and yields a spectrum comprised of a wavenumber $\overline{\nu}$, emission coefficient $\varepsilon_{\overline{\nu}}$, and absorption coefficient $\alpha(\overline{\nu})$, over a variable width spectral grid.

Glue.m is the routine which superposes the different individual spectra to yield a global spectrum with a variable spectral grid.

GUInterface.m, GuiFunctions.m GUITrace.m, IOWrite.m Are functions specific to the GUI of the SPARTAN code. `IOWrite.m` updates the Inputs.txt file according to the user inputs from the GUI.

Integrate.m Integrates the individual radiative systems spectral dependent emission coefficients $\varepsilon_{\overline{\nu}}$ to yield to their individual and the total radiative power in $\mathrm{W/m^3}$.

Fig. 3.2 presents the flowchart of the SPARTAN code.

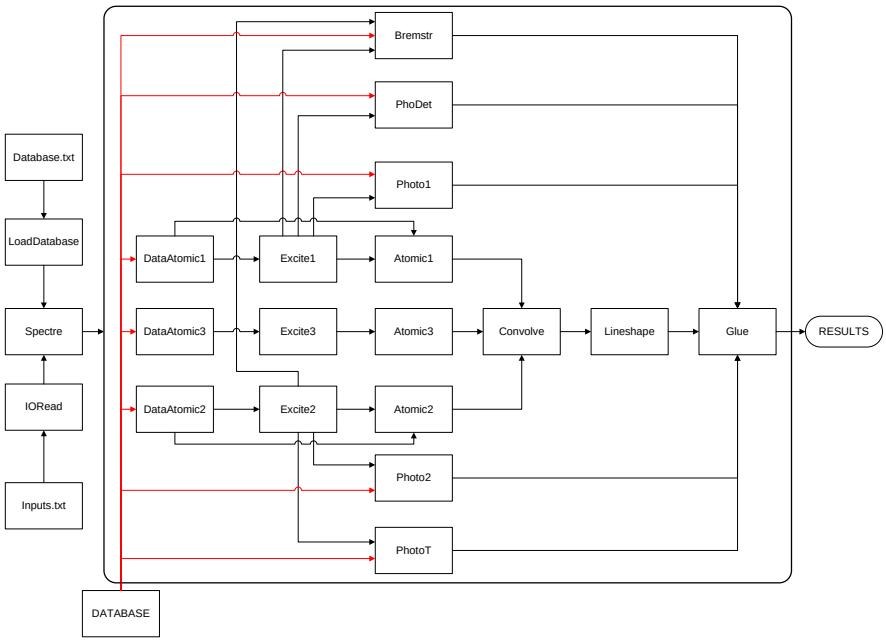

Figure 3.2: Flowchart of the SPARTAN code

3.5 The Lineshape calculation routine

This lineshape calculation routine may be considered as the "core" of the application. Indeed, even though setting up a line database may be a challenging task from a practical point of view[2], this poses no particular problem from a numerical point of view. In fact, the problem can be solved efficiently using vector programming, taking advantage of the capabilities of the MATLAB language. However, the convolution of a large number of lines with a Voigt profile is a very intensive operation. Therefore, great care was exerted when developing the line convolution routine, in order to achieve the shortest calculation times alongside with a maximal precision of the calculated lineshapes. Furthermore, the program routine has been built so as to allow the user to adjust a large array of parameters defining among others the number of points of the calculated lineshapes. Still, the ratio of the time needed for the lines convolution and the time needed for building up the line database is higher than 100 and increases as the precision of the calculated lineshapes is increased.

In short, the user can define itself which is the level of precision required in his calculations. More accurate lineshapes will require a large spectral grid and larger computation times. Less precise calculations will allow defining preliminary calculations, or even allow affordable large-scale computations over a fluid dynamics calculation grid. Some of the routine parameters can be easily adjusted by users with a limited background on spectral lineshapes, others require a more extensive knowledge on the lineshape calculation methods and are recommended to be kept at their default values.

The routine for the calculation of the computed spectra lineshapes, as well as the overall user-defined parameters are described below. The user-defined parameters can be adjusted editing the file `Lineshape.txt` in the `INPUTS` directory.

The `Lineshape.m` routine accepts as an input a matrix of size $n \times 5$ containing the parameters for the calculation of n lines: wavenumber $\overline{\nu}$, emission coefficient $\varepsilon_{\overline{\nu}}$, absorption coefficient $\alpha(\overline{\nu})$, Lorentz full width at half maximum (FWHM) $\Delta\overline{\nu}_L$, and Doppler full width at half maximum (FWHM) $\Delta\overline{\nu}_G$. The routine then outputs the overall spectra wavenumber, emission and absorption coefficients. The routine works as follows:

1. Separates the lines among three different categories: strong, weak, and very weak (according to the parameters LinPar.[threshold1, threshold2])

2. Defines which lines are to be explicitly calculated, and which are to be calculated as a "pseudo-continuum". strong lines are calculated explicitly, very weak lines are calculated as a "pseudo-continuum", weak lines are calculated explicitly if they are not covered by a strong line. If the "pseudo-continuum" is not selected (LinPar.contmethod=0) we have two possibilities:

   (a) The emission and absorption intensities of the explicitly calculated lines are multiplied by a constant factor to account for the intensities of the discarded lines and enforce energy conservation.

[2] adequate spectroscopic constants for the calculation of line positions and intensities need to be selected, along with the adequate expressions issued from spectroscopic theory.

(b) No further action is carried aside from discarding the weak lines.

In either cases steps **3** and **8** are overrided.

3. Intensities of the lines calculated as a "pseudo-continuum" are distributed in slots over a fixed step wavelength (LinPar.ContStep) ranging from the "pseudo-continuum" lines lower to higher wavenumber.

4. For each line calculated explicitly:

   (a) Checks if the Doppler and Lorentz broadening widths of the current and former calculated line differ from more than a user-defined parameter (LinPar.diff).

   (b) YES: Calculates the line center distance and intensity for each of the user-defined (LinPar.[ksi, beta, ksi1, beta1, num_c, num_w, par_c, par_w, par_w_FG]) lineshape points, using a Voigt profile.

   (c) NO: Uses the former calculated line gridpoints, sparing calculation time.

5. Stores the overall points in ascending order (from lower to higher wavenumbers) for the determination of the spectral grid.

6. Removes the points which are too close (according to the user-defined parameter LinPar.minstep)

7. For each line:

   (a) Selects the grid points which fall under the calculated lineshape.

   (b) Interpolates and adds the line intensities to the new gridpoints region.

8. Interpolates and adds the "pseudo-continuum" intensities to the calculated grid.

A schematic view of the selection process of the different lines, split into strong, weak, and very weak categories, is presented in Fig. 3.3

The user-defined parameters are:

LinPar.interp: This parameter defines the point's interpolation method used for the routine. The two possibilities are **linear** and **cubic**. linear interpolations are fastest but less accurate than cubic. It is recommender to use cubic interpolations.

LinPar.shape: This parameter allows the user to allow the calculation of a general Voigt lineshape (parameter **99**), computed with a user-defined number of points for the lineshape core and the wings (LinPar.num_c and LinPar.num_w=6), or to allow the calculation of a simplified Voigt profile with 5, 7, 9 or 11 points (respectively parameters **5**, **7**, **9**, or **11**). For more details on the calculation of the Voigt profile see section 3.5.1.

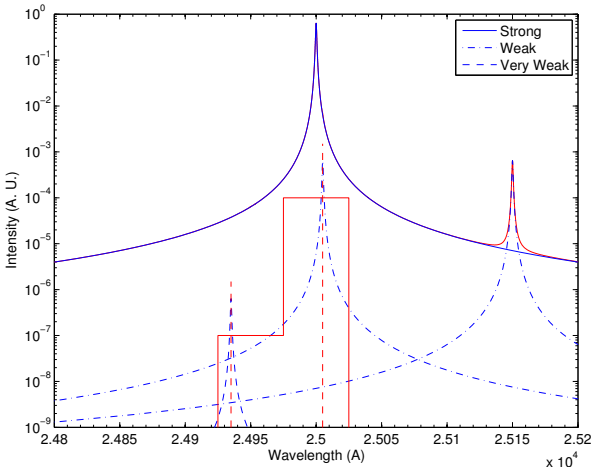

Figure 3.3: Example of Strong, Weak, and Very weak lines

LinPar.LineBound: Parameter which defines the boundary inside which a high resolution lineshape is calculated and core and wings points are distributed (see section 3.5.1 for more details). This parameter is dependent on parameter LinPar.threshold1. 20 is recommended for LinPar.threshold1=1e3, higher values are recommended for higher thresholds.

LinPar.ksi: Parameter which defines the Lorentz weight parameter defining the boundary between the lineshape core and wings regions (see section 3.5.1 or [1] for more details). The recommended value for this parameter is **1.8**.

LinPar.beta: Parameter which defines the Gauss weight parameter defining the boundary between the lineshape core and wings regions (see section 3.5.1 or [1] for more details). The recommended value for this parameter is **1**.

LinPar.ksi1: Parameter which defines the Lorentz weight parameter defining the boundary between the lineshape wing and far wings regions. (see section 3.5.1 or [1] for more details). The recommended value for this parameter is **5.8**.

LinPar.beta1: Parameter which defines the Gauss weight parameter defining the boundary between the lineshape wing and far wings regions. (see section 3.5.1 or [1] for more details). The recommended value for this parameter is **5.8**.

LinPar.num_c: Number of points of the lineshape half core region (including line maximum). Total number of points in the core region of the lineshape: $2 \times LinPar.num_c - 1$. Recommended values: from **3** to **6**.

LinPar.num_w: Number of points of the lineshape half wing region. Total number of points in the wings region of the lineshape: $2 \times LinPar.num_w$. Recommended values: from **6** to **12**.

LinPar.par_c: Parameter defining the core points distribution spacing (see section 3.5.1 or [1] for more details).

LinPar.par_w: Parameter defining the Lorentz contribution for wings points distribution spacing (see section 3.5.1 or [1] for more details).

LinPar.par_w_FG: Parameter defining the Gauss contribution for wings points distribution spacing (see section 3.5.1 or [1] for more details).

LinPar.diff: Maximum difference among the Gauss and Lorentz lineshapes of two different lines for which the Voigt profile is not recalculated for the second line. Recommended value: **0.1** corresponding to a 10% difference.

LinPar.Lorentz: $LinPar.Lorentz \times FWHM$ is the minimum distance from the line center where the line profile is considered to be Lorentzian. Recommended value: **64**.

LinPar.cutoff: $LinPar.cutoff \times FWHM$ is the distance from the line center where the line intensity is considered to be negligible (Intensity=0). Recommended value: **1000**.

LinPar.minstep: Minimum interval between two adjacent lineshape points ($FWHM \times LinPar.minstep$). This parameter is useful for defining the accuracy of the calculated line peaks. If the parameter is set to 99, it will be equivalent to the minimum distance between adjacent points of the computed Voigt profile. Recommended value: **99**.

LinPar.intstep: Grid size for the calculation of the lineshape integral in the core region. Recommended value: **120**

LinPar.integral: Line normalization carried over the integral of a high resolution Voigt lineshape **1** or the integral of the selected lineshape for the overall calculations. When computing a low resolution profile, setting this option to **0** will allow the line peaks will have the correct intensities, but the overall line energy will not be accurate. Setting this option to **1** will yield less accurate line peak intensities, but will allow the correct overall line energy. For higher resolution lineshapes ($LinPar.shape = 99$) it is recommended to keep the value at **0**.

LinPar.contmethod: Method used for accounting for the presence of weak lines. Setting this option to **1** uses the "pseudo-continuum" method. Setting this option to **0** discards the lines not calculated by the "Line-by-Line" method.

LinPar.addWeakLines: Setting this option to **1** homogeneously adds the discarded lines intensities to the calculated lines intensities $\left[I^{weak}_{emi,abs} = I^{weak}_{emi,abs} \times \left(1 + \sum I^{weak}_{emi,abs} / \sum I^{strong}_{emi,abs}\right)\right]$. Setting this option to **0** simply discards the lines.

LinPar.threshold1: Threshold (normalized to the maximum line emission intensity **OR** the maximum line absorption intensity) above which a line is selected to be calculated using the "Line-by-Line" method. Recommended values: $10^3 - 10^6$ Higher values will have more lines included in the overall calculation, yielding more accurate spectra, at the cost of larger memory an computation time overheads. Note that for consistency, one must have $LinPar.threshold1 \leq LinPar.threshold2$

LinPar.threshold2: Threshold (normalized to the maximum line emission intensity **AND** the maximum line absorption intensity) below which a line intensity contribution is added as a "pseudo-continuum" to the overall spectrum. Recommended values: $10^4 - 10^7$ Higher values will have less lines quickly calculated as a "pseudo-continuum, yielding more accurate spectra, at the cost of larger memory and computation time overheads. Note that for consistency, one must have $LinPar.threshold1 \leq LinPar.threshold2$

LinPar.dnu: $LinPar.dnu \times FWHM_{med}$ is the boundary (from the line center) defining the region were a weak line is covered by a strong line (making it's calculation as a "pseudo continuum" viable). Recommended value: **20** if $\frac{LinPar.threshold2}{LinPar.threshold1} = 10^3$. For higher values of this ratio, it is recommended to increase $LinPar.dnu$.

LinPar.contstep: $LinPar.dnu \times FWHM_i$ is the fixed spectral width step of the grid used for the calculation of the "pseudo-continuum" spectrum. Recommended value: **20**.

3.5.1 Calculation of a Voigt lineshape

This subsection presents a more detailed description of the Voigt lineshape calculations carried in step 4.b (see section 3.5).

The main objective is to ensure the calculation of a line profile as close to Eq. 2.36 as possible, while retaining a minimum number of points. The method implemented in the SPARTAN code yields profiles which are found to adequately approximate the Voigt profile of Whiting & Olivero to a user-defined precision which will depend on the number of considered grid points. The routine discriminates two sets of Voigt line profiles: a low resolution set which allows quick spectral calculations yielding a compact overall spectral grid, and a high resolution set for more smooth and detailed line profiles, at the cost of larger spectral grids.

Four low-resolution Voigt line profiles with respectively 5, 7, 9 and 11 grid points have been defined, introducing the parameters W and FW which define the boundaries between the line center region, the "near" line wings, and the "far" line wings respectively. The expression for those parameters, for a given Voigt profile, is proposed by Zhu [32]:

$$[W, FW] = \frac{2}{\pi}(1+\zeta)\Delta\overline{\nu}_L + \beta\Delta\overline{\nu}_D \tag{3.1}$$

the $[\zeta, \beta]$ constants are held at [1,1.8] for the calculation of the parameter W, as proposed by Smith [33], and held at [2.6,5.8] for the calculation of the

parameter FW according to a critical analysis carried by Lino da Silva on sample Lorentz, Doppler, and Voigt profiles. The different grid points have been defined accordingly[3], and are presented in Table 3.1.

Number of Points	Selected Points					
	$\overline{\nu}_0$	V/8	V/2	W	FW	25V/2
5	×			×		×
7	×			×	×	×
9	×		×	×	×	×
11	×	×	×	×	×	×

Table 3.1: Gridpoints for 5, 7, 9, and 11 points lineshapes. An × defines a specific point being accounted for in the given lineshape

A different method has been devised for the calculation of high resolution profiles. Two line parameters par_c and par_w have firstly been defined, related to the line center and line wings respectively. The line center being identical whether the profile is Lorentz or Doppler, par_c will be independent of the parameters $\Delta\overline{\nu}_L$ and $\Delta\overline{\nu}_D$.

The lineshape wings will however be very different regarding whether the line profile is Doppler or Lorentz. par_w will therefore have a strong dependence on the parameters $\Delta\overline{\nu}_L$ and $\Delta\overline{\nu}_D$, and such dependence has been acknowledged in the following way:

$$par_w = par_{wL} + \frac{\Delta\overline{\nu}_D}{\Delta\overline{\nu}_D + \Delta\overline{\nu}_L} par_{wD} \tag{3.2}$$

such that for a Lorentz lineshape we have $par_w = par_{wL}$ and for a Doppler lineshape we have $par_w = par_{wL} + par_{wD}$.

A series of monotonous points has then been defined such as

$$i_0 = [0 : max/(num_c - 1) : max] \tag{3.3}$$

and a geometrical transform is applied such that

$$i = \frac{1 - \exp\left(par_{(c,w)} \times i_0(1)\right) / \exp\left(par_{(c,w)} \times i_0(max)\right)}{1 - \exp\left(par_{(c,w)} \times i_0(1)\right) / \exp\left(par_{(c,w)} \times i_0(max)\right)} \tag{3.4}$$

We then define $i_c = i$ and $i_w = 1 - i$. An example of the geometrical transforms i_c and i_w, obtained for specific par_c and par_w values, is presented in Fig. 3.4. Practically speaking, such transformations return two grids more or less tightened around the values 0 or 1.

These two grids need now to be put to use. Firstly, for distributing the grid points in the line center region, the second derivative of the Voigt profile is firstly calculated. Then the line profile points $\overline{\nu}_i$ are determined according to the following relation:

$$i_c = \frac{v''(\overline{\nu}_i)_c}{max[v''(\overline{\nu}_i)_c]} \tag{3.5}$$

[3]Considering a zero line intensity for the last grid point

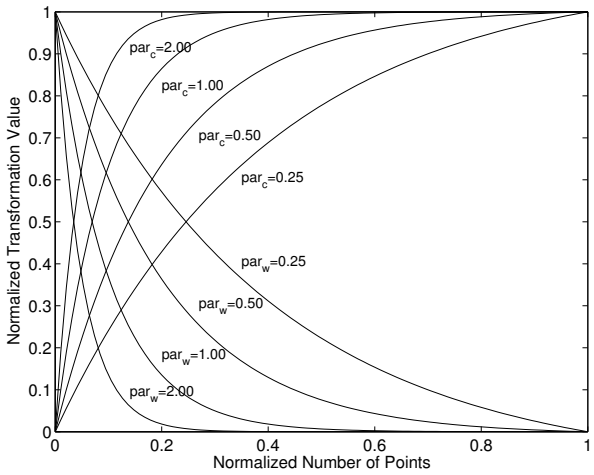

Figure 3.4: Plot of the numerical transforms yielding the unevenly-spaced gridpoints i_c and i_w from the evenly-spaced gridpoints i, for different values of the adjustable parameters par_c and par_w.

Which means that the spectral grid will be tighter in the profile regions with large second derivatives (near the line center). Here, the second derivative is a good variational parameter as it allows an optimum distribution of lineshape points, ensuring an adequate reproduction of the exact lineshape through the linear connection of such points.

The line wings structure is such that the optimal grid points distribution is considered to be given by the relation

$$i_w = \frac{v(\overline{\nu}_i)_w}{max[v(\overline{\nu}_i)_w]} \tag{3.6}$$

Which allows distributing the grid points efficiently in the "far" wings regions where the intensity decrease is very slow (thus explaining the tightening of the parameter i_w near 0).

We may now assign a given number of points to be distributed near the line center and the line wings. The calculation routine then proceeds according to the described method in order to optimally distribute such points. More precise line profiles will be obtained for a larger number of assigned grid points, at the cost of increased spectral grids and calculation times.

Different low and high resolution lineshapes have been compared with the exact Voigt profiles (Eq. 2.36) with $\Delta\overline{\nu}$=5 cm^{-1}. The differences to the exact profile have also been determined for each of such profiles. The obtained results are presented in Fig. 5 for low resolution profiles, and in Fig. 6 for high resolution profiles.

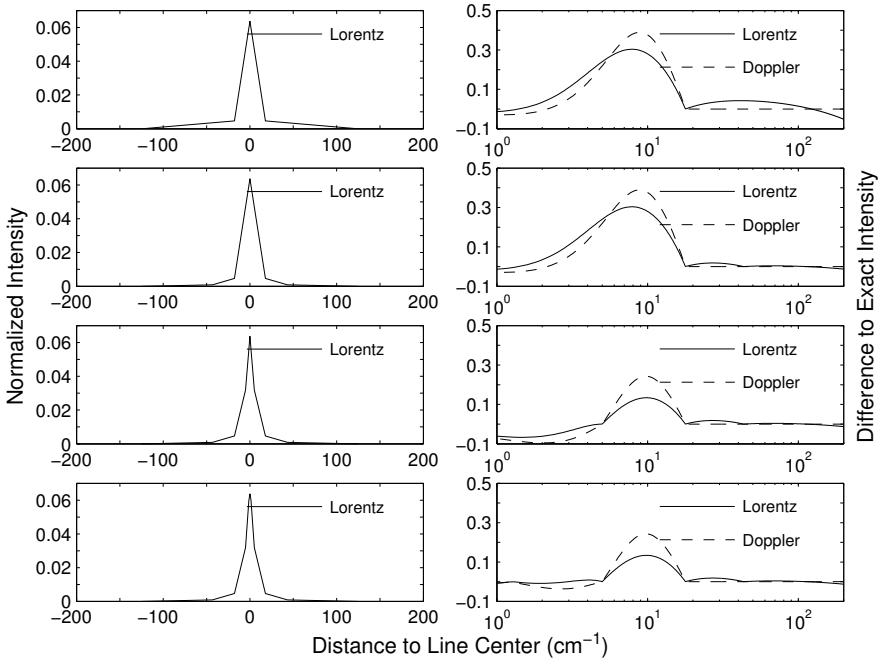

Figure 3.5: Plot of low resolution Lorentz lineshapes (left; 5, 7, 9 and 11 points from top to bottom; $\Delta\overline{\nu}$=5 cm^{-1}) and plot of the normalized difference of Lorentz (full line; $\Delta\overline{\nu}$=5 cm^{-1}) and Doppler (dotted line; $\Delta\overline{\nu}$=5 cm^{-1}) lineshapes to the exact lineshapes (right; 5, 7, 9 and 11 points from top to bottom).

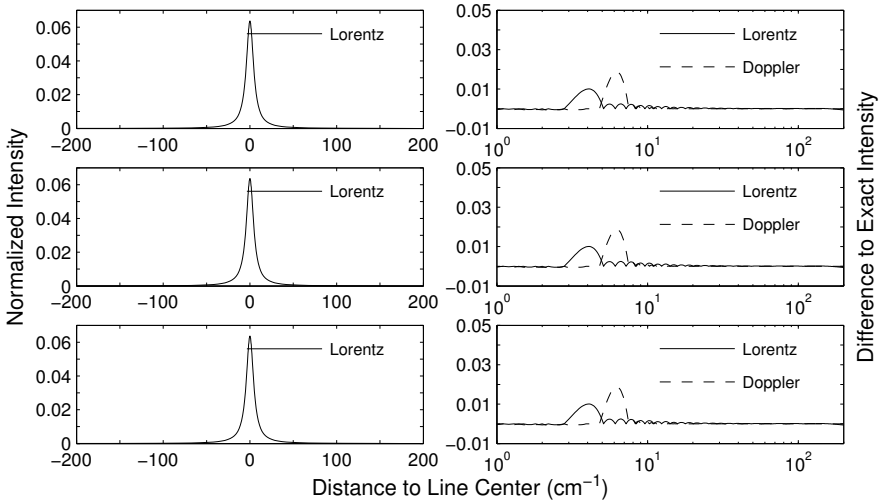

Figure 3.6: Plot of high resolution Lorentz lineshapes (left; 21, 37, and 73 points from top to bottom; $\Delta\overline{\nu}$=5 cm^{-1}) and plot of the normalized difference of Lorentz (full line; $\Delta\overline{\nu}$=5 cm^{-1}) and Doppler (dotted line; $\Delta\overline{\nu}$=5 cm^{-1}) lineshapes to the exact lineshapes (right; 21, 37, and 73 points from top to bottom).

3.5.2 Handling and Overlay of Individual Lineshapes

Following the definition of a method for adaptively calculating individual lineshapes, one may apply it to the calculation of the individual lineshapes for each of the calculated radiative transitions (with their accompanying Doppler and Lorentz FWHM). However doing so for a large number of lines (typically more than 10^4) might still yield large calculation times. One can acknowledge that the systematic evaluation of exponential terms of Eq. 2.36 for the calculation of several thousand lines might be an ineffective method. Instead, one can take advantage of the fact that the different lineshapes Doppler and Lorentz FWHM remain very close over a large spectral range. The calculated lineshapes are then nearly equivalent and there is no need to systematically recalculate them.

As an example, the differences between two Voigt lineshapes, for a 10% variation of their Lorentz and Doppler FWHM, is presented in Fig. 3.7. Given the small differences between such spectra, one may chose not to recalculate a spectral lineshape if both the Lorentz and Doppler FWHM differ less than by a given percentage (10% being an adequate value).

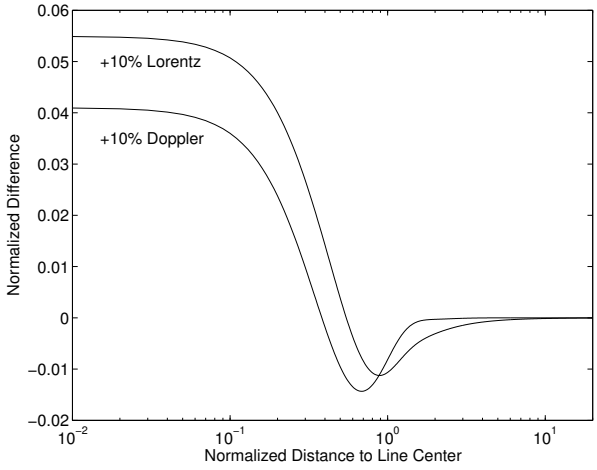

Figure 3.7: Normalized difference between two Voigt lineshapes with $\Delta\overline{\nu}'_L = 1.1\Delta\overline{\nu}_L$ & $\Delta\overline{\nu}'_D = 1.1\Delta\overline{\nu}_D$, and an initial Voigt lineshape with $\Delta\overline{\nu}_{L,D} = 5\text{cm}^{-1}$.

Such approach further improves computational efficiency, as for most of the transitions to be simulated, the calculation routine merely replicates the previous lineshape spectral grid points and relative intensities, simply multiplying the relative line intensities by the line strength to yield the absolute line intensities.

Once that the spectral lineshapes have been calculated for each of the overall database transitions, such individual lineshapes have then to be combined to yield an overall spectra.

This is firstly done considering the overall calculated grid points and grouping them in an increasing order. Secondly, the spectral points too close to each other by a defined parameter (named *minstep* and typically 1/40 of the FWHM) are grouped. Finally, each individual lineshape is interpolated over the boundaries of the overall spectral grid which falls inside the first and last grid points

of the individual lineshape. The overall discrete spectrum is then overlaid to the previously calculated "pseudo-continuum" spectrum to yield the final spectrum.

In brief, this proposed adaptive grid method represents an approach where a series of approximations ("pseudo-continuum", calculation of Voigt lineshapes with a minimum number of points, non-systematic lineshape recalculation) are carried in order to achieve consequent reduction of calculation times and spectral grids. One more advantage of the proposed method is the fact that it is fully user-parameterizable, and allows one to chose the level of accuracy (with the associated memory and computational overheads) when carrying spectral calculations.

Chapter 4

Modifying the Code Spectral Database

.

"With Great Power comes Great Responsibility"

Voltaire

4.1 Introduction

This Chapter provides an in-depth description of the spectral database structure of the SPARTAN code, with the description of the necessary steps for its update or upgrade, according to the user needs.

The capabilities of the SPARTAN code are summarized in Table 4.1. Bound-Bound transitions are all treated through its own subroutines (`AtomicX.m`), which implement the theoretical models described in Chapter 3. Bound-Free transitions are subdivided in photoionization, photodissociation (for diatomic and triatomic molecules) and photodetachment transitions, which can either use total or state-specific cross-sections. Finally Free–Free transitions are hard-coded in their own routine (`Bremstr.m`).

Discrete transitions from diatomic species play a predominant part in the spectral features of gases and plasmas. As such, the databases for the simulation of these transitions are the most liable to be the subject of extensions and updates. Accordingly, we will begin this section by providing some guidelines for the selection of an appropriate spectral database for any given bound diatomic transition. We will then follow with the description of the steps necessary for the construction of the datafiles for the calculation of bound diatomic spectra. Next we will describe how to update the databases for the other transitions (bound transitions for atomic and linear triatomic species, and continuum transitions, including a description of the hard-coded Free–Free transitions). Finally we will close this tutorial Chapter through the description on how to link any new spectral databases to the SPARTAN code.

			Atomic	Diatomic	Triatomic Linear
Bound–Bound			User-defined (`Atomic1.m`)	User-defined (`Atomic2.m`)	User-defined (`Atomic3.m`)
Bound–Free	Photoionization	Total	–	User-defined (`PhotoT.m`)	–
		Level Specific	User-defined (`Photo1.m`)	User-defined (`Photo2.m`)	
	Photodissociation	Total	–	User-defined (`PhotoT.m`)	
		Level Specific	–	User-defined (`Photo2.m`)	
	Photodetachment	Total	–	User-defined (`PhoDet.m`)	
Free–Free (Bremstrahlung)			Hard-coded (`Bremstr.m`)	Hard-coded (`Bremstr.m`)	–

Table 4.1: Transitions modeled by the SPARTAN code, corresponding numerical routines, and spectral datafile types

4.2 Building spectral datafiles for diatomic transitions

This section provides an in-depth description on how to create and modify spectroscopic constant files in a format compatible with the SPARTAN code, and provides some guidelines for the appropriate selection of spectral data which is consistent with the user needs.

4.2.1 Guidelines for the selection of appropriated spectral constants

When deciding to develop a new spectral database for a specific diatomic transition, one first needs to examine the degree of accuracy of the spectral constants that can be found in the literature. It is then necesary to inquire up to which degree the spectra might be affected by perturbations by another states.

As discussed briefly in Chapter 2, three levels of detail can be considered when creating/modifying the spectral database for a specific diatomic transition:

1. Selection of a Dunham matrix providing the expressions for the rovibronic energies for any arbitrary values of v and J, according to the expressions of Eq. 2.10.

2. Selection of a set of vibrationally-specific constants B_v, D_v, ... for a given set of vibrational levels v_i, allowing the calculation of the level energies for any arbitrary rotational quantum level J (see Eqs. 2.11).

3. Selection of the energy shifts around a specific rotational quantum number J_i, for a given vibrational quantum number v_i. This treatment is necessary for the accounting for rotational perturbation effects and is carried in addition to considering either a set of equilibrium or vibrationally-specific spectroscopic constants.

Usually, selecting an appropriate Dunham matrix with up-to-date spectroscopic constants is sufficient for most general radiative transfer applications. For the accurate reproduction of measured spectra (with FWHM<1Å) it is sometimes necessary to supply level-specific spectroscopic constants to complement the equilibrium constants.

Another aspect to take into consideration is the order of the spectroscopic constants that are selected. Due to the inherent oscillatory characteristics of polynomial expansions such as those depending on $v + 1/2$ for vibrational levels, and $J(J + 1)$ for rotational levels, a dataset with larger order corrective spectroscopic constants will be able to reproduce a broader range of vibrational/rotational quantum numbers v/J, but a dataset with lower order corrections will usually provide better extrapolations beyond the initial fit validity range. Therefore, as a rule of thumb, the higher the order of the spectral constants corrections (in polynomial form), the most likely that the level energies above the range of the fitted v and J numbers will strongly diverge from their exact values.

The selection of an appropriate Dunham matrix can by itself allow the calculation of a synthetic spectrum which accurately reproduces experimental results. Spectroscopy techniques have known almost spectacular developments over the last 50 decades, and increasingly accurate data, valid for a broad range of vibrational and rotational levels, has been made available in the most recently years, usually as the result of the application of very detailed Fourier transform spectroscopy methods. A striking example for such developments can be provided for the CN Violet $\Delta v = 0$ spectrum, who is ubiquitous in most of air and carbon chemistry plasmas. This system has a very clear bandhead structure which can be detected up to $v = 8 - 9$, with a band reversal from the ultraviolet direction towards the infrared direction starting at $v = 4 - 5$, whose bandheads are experimentally overlapped. In Fig. 4.1, an experimental spectrum issued from an arcjet low-pressure wind-tunnel [1] is compared against several synthetic spectra produced using the best-fit vibrational and rotational temperatures $T_{vib} = 10800 \pm 100\,\mathrm{K}$ and $T_{rot} = 4900 \pm 100\,\mathrm{K}$, and applying several sets of Dunham coefficients.

One may verify that the reproduction of the higher vibrational number bands is increasingly poorer when resorting to older spectral datasets. Namely, the $v = 4 - 5$ bandheads can only be accurately reproduced with the most recent datasets issued from Fourier transform spectroscopy techniques[1].

In some specific cases, equilibrium constants will not provide sufficient accuracy for the reproduction of experimental spectra. Sometimes, this might be related to the extra loss of precision resulting from the extra fit from level-

[1] However, even such techniques may sometimes not be adapted for the reproduction of high-temperature spectra in such cases where lower temperatures of the gas/plasma are imposed so as to have very little Doppler broadening of the measured lines, which comes at a cost of a lower J_{max} of the fit, since higher rotational levels will not be sufficiently populated at such values for T.

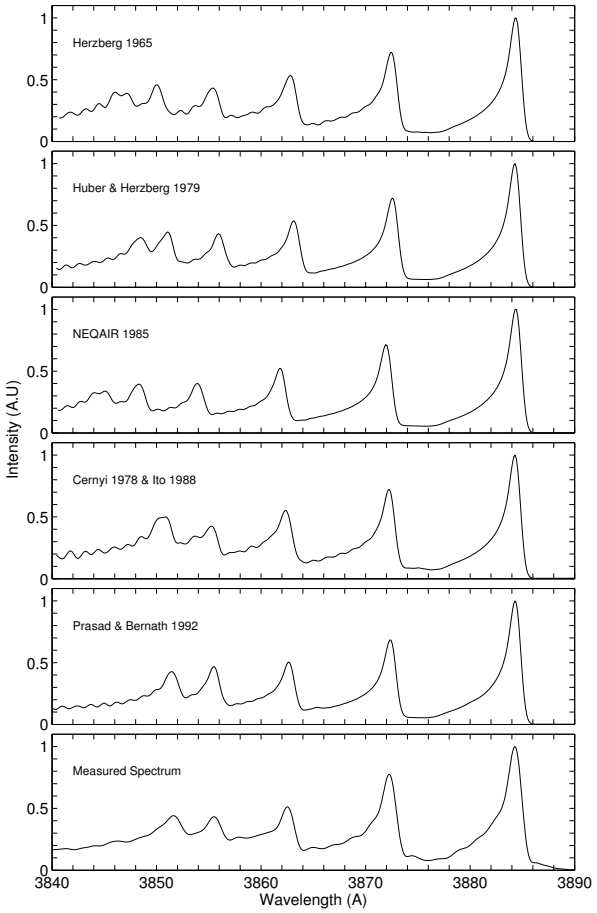

Figure 4.1: Comparison between a CN Violet Δv=0 spectrum measured in a high-temperature arcjet facility and several spectra using different sets of spectroscpic constants

dependent spectroscopic constants to the more "universal" Dunham spectroscopic coefficients. More often, this is the result of vibrational perturbations in the upper or lower levels of the spectra, which are the results from "avoided crossings" of these states rotationless potentials. In this case, the shape of the potential curve will change dramatically after a critical vibrational number v, and the level spectroscopic constants will see a sharp change in their trends, disallowing their proper reproduction through the use of polynomial expressions depending on the variable $(v + 1/2)$.

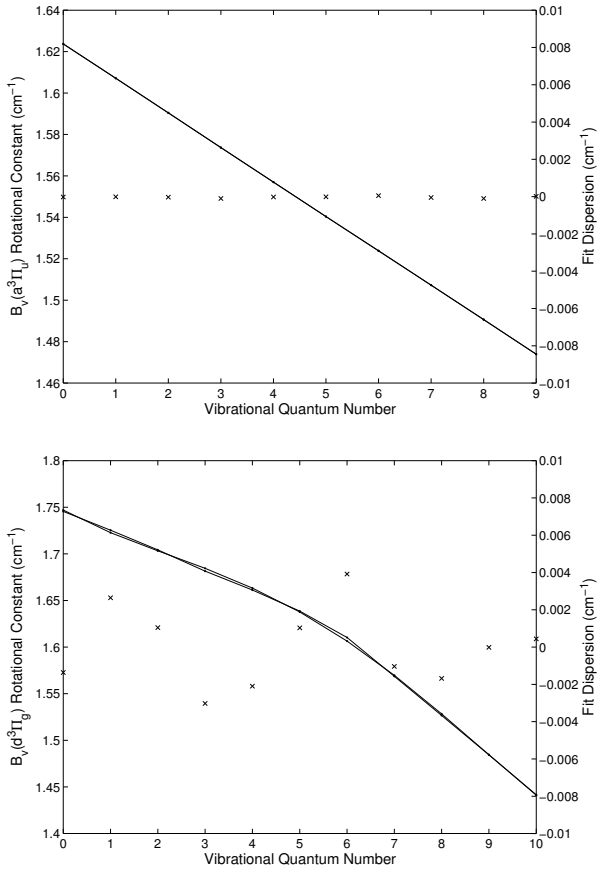

Figure 4.2: Interpolation of the level-specific rotational constants B_v for the unperturbed $a^3\Pi_u$ (top) and the perturbed $d^3\Pi_g$ (bottom) electronic states of C_2

One example can be presented for the C_2 Swan bands system, who is also generally ubiquitous in carbon-based plasmas. Fig. 4.2 shows the fit of the constants B_v for unperturbed lower a state, and for the perturbed d state. One may immediately verify that the polynomial fit will be very uncertain for the perturbed state, which helps explaining why considering level-dependent spectroscopic constants B_v, D_v, etc... will provide more accurate results than resolving to a matrix of Dunham coefficients. Such a comparison, using both methods, is presented in Fig. 4.3.

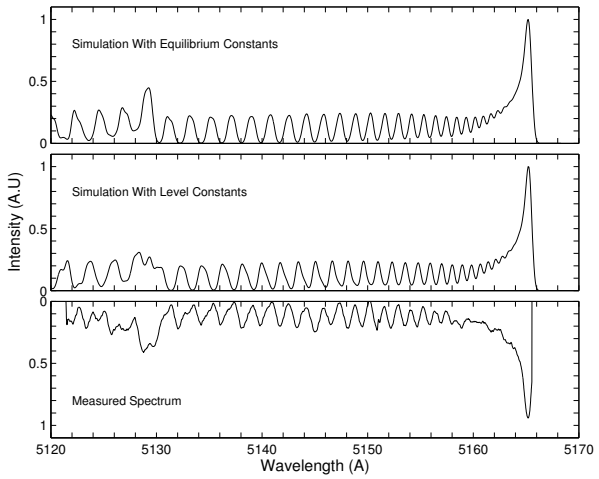

Figure 4.3: Reproduction of an experimental spectrum of the Swan bands of C_2, Δv=0 using level-dependent spectroscopic constants, and using Dunham coefficients

Finally, as discussed in Chapter 2, rotational perturbations can be modeled after using a simplified approach implemented in the SPARTAN code. In the current version of the code, this is restricted to doublet transitions, due to the necessity of modeling the perturbations in the N_2^+ First Negative System. This approach requires information on the perturbations, specifically, the central perturbed rotational quantum number J_{pert}, the value for the maximum perturbation shift dE_{pert} in absolute values, and the reference for the affected branch $F_{1,2}$. This obviously implies such values, as reported in the literature, can be retrieved. An example for the influence of perturbations is presented in Fig. 4.4, where an experimental spectrum of N_2^+ First Negative system Δv=0, obtained in a low-pressure arcjet facility, is reproduced by synthetic spectra using only de-perturbed constants, and using perturbed constants following the approach implemented in the SPARTAN code. We verify that even the addition of this simplified treatment for perturbations may significantly improved the reproduction of experimental spectra.

4.2.2 Step-by-step instructions

Here we will describe how a spectral database file compatible with the format utilized by the SPARTAN code can be created, therefore allowing the simulation of any arbitrary multiplet radiative transition for a diatomic species AB

Step 1: Create a definition file with the radiative transitions of the species

First of all, a new definition file for the calculation of the radiative transitions of the species must be created. For simplicity, we will consider a molecular species assuming transitions between singlet states $A^1\Pi$–$X^1\Sigma$ such as the ones

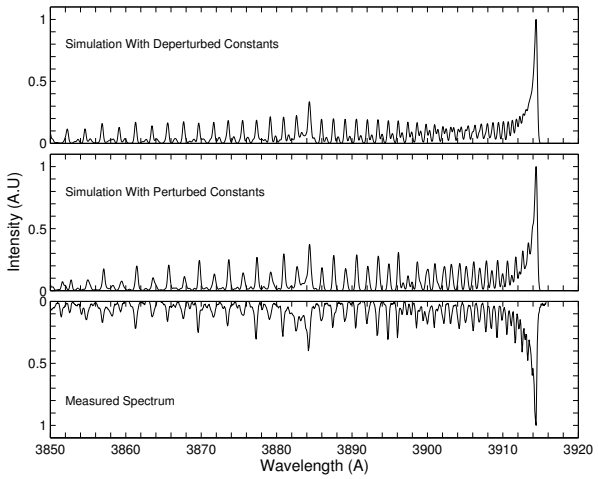

Figure 4.4: Comparison between a measured N_2^+ First Negative System, Δv=0 spectrum, and synthetic spectra obtained using both deperturbed and perturbed rotational constants

defined in the `CO-4P.txt` file. In fact, we suggest opening that file and editing it for the new species (at the end, do not forget to save the modifications as a new file).

Step 2: Edit the Dunham matrix

The correspondence between the Dunham coefficients and the "traditional" spectral constants is given in Table 4.2. Open the `CO-4P.txt` file. At the top of the file, there are two Dunham matrix: one for the upper energy level $A^1\Pi$ and another for the lower energy level $X^1\Sigma$. The bibliographic references for the spectral constants are typically indicated in the file. The size of the matrix must always be 7×10 and only the spectral constants values must be edited for the new species. Set all the matrix components to zero and then introduce the constants for the new species.

Step 2.a: Add fine-structure constants for doublet or triplet states

In this tutorial we have considered the implementation of a new molecular species assuming transitions between singlet states. If you want to implement transitions considering doublet or triplet states, you must consider fine-structure corrections shown in Table 4.3. After the Dunham matrix for the upper and lower level respectively, add a new line with four columns where you introduce the four fine-structure terms. Again if you have no values, put zero (the insertion of four values is mandatory).

To see an example of how the fine-structure constants are inserted after the states Dunham matrix, please refer to file `N2-1P.txt` describing a $^3\Pi - ^3\Sigma$ transition.

	Y_{ij}	0	1	2	3	4	5	6	7	8	9
G(v)	0	T(e)	ω_e	$-\omega_e x_e$	$\omega_e y_e$	$\omega_e z_e$	$\omega_e a_e$	$\omega_e b_e$	$\omega_e c_e$	×	×
B_v	1	B_e	$-\alpha_e$	γ_e	δ_e	η_e	×	×	×	×	×
-D_v	2	-D_e	$-\beta_e$	×	×	×	×	×	×	×	×
H_v	3	H_e	αH	×	×	×	×	×	×	×	×
L_v	4	×	×	×	×	×	×	×	×	×	×
M_v	5	×	×	×	×	×	×	×	×	×	×
N_v	6	×	×	×	×	×	×	×	×	×	×

Table 4.2: Correspondence between Dunham coefficients and traditional spectroscopic constants

$^1\Sigma$	–
$^1\Pi$	–
$^2\Sigma$	$\gamma_v = \gamma^{(0)} + \gamma^{(1)}(v+\frac{1}{2}) + \gamma^{(2)}(v+\frac{1}{2})^2 + \gamma^{(3)}(v+\frac{1}{2})^3$
$^2\Pi$	$A_v = A^{(0)} + A^{(1)}(v+\frac{1}{2}) + A^{(2)}(v+\frac{1}{2})^2 + A^{(3)}(v+\frac{1}{2})^3$
$^3\Sigma$	$\gamma_v = \gamma^{(0)} + \gamma^{(1)}(v+\frac{1}{2}) + \gamma^{(2)}(v+\frac{1}{2})^2 + \gamma^{(3)}(v+\frac{1}{2})^3$ $\lambda_v = \lambda^{(0)} + \lambda^{(1)}(v+\frac{1}{2}) + \lambda^{(2)}(v+\frac{1}{2})^2 + \lambda^{(3)}(v+\frac{1}{2})^3$
$^3\Pi$	$A_v = A^{(0)} + A^{(1)}(v+\frac{1}{2}) + A^{(2)}(v+\frac{1}{2})^2 + A^{(3)}(v+\frac{1}{2})^3$

Table 4.3: Fine-structure constants for doublet and triplet states

Step 3: Provide the Species Nuclear Spin statistical weight

If the species is heteronuclear (AB), this parameter is meaningless and the value **99** is mandatory.

If the species is homonuclear (AA), the values tabulated in Table 4.4 have to be included, depending on whether the molecule is a symmetric/antisymmetric boson/fermion.

Step 4 (optional): Define vibrationally-specific constants for each upper and lower electronic states

	Symmetric	Antisymmetric
Boson	1	-1
Fermion	0	-0.1

Table 4.4: Values for homonuclear molecules

If you want to introduce vibrationally-specific constants for each vibrational level of the species, consider as an example the `H2-LY.txt` file. In this file, transitions between the $B^1\Sigma$ and the $X^1\Sigma$ levels of molecular hydrogen are simulated. After defining the nuclear spin statistical weight, set the "vibrationally-specific constants" label to **1**. Then, for each state define the number of vibrational levels and then explicit the vibrational levels considered.

After this, you have to define the number of variables you want to use and specify each of them. To each specific variable corresponds a spectroscopic constant. The correspondence between the specific variables and the spectroscopic constants is shown in Table 4.5. So after defining the number of specific variables you want to use, you must specify which are the ones you are considering. Then, you must introduce the vibrationally-specific constants for each level in a $n \times m$ matrix, where n is the number of vibrational levels and m is the number of specific variables considered. In case you do not want to use vibrationally-specific constants, just set the label "vibrationally-specific constants" to **0** and proceed to the next step.

Step 5 (optional): Define the perturbations in the rotational spectra

As for the case of explicit values, if no perturbations to the rotational spectrum are to be inserted, set the "perturbations" label to **0** and proceed to the next step. Otherwise set the label to **1**. Please remember that in the current version of the code, only doublet states can be perturbed [2].

We will now list the parameters to be inserted. The first line should list the number of perturbations n, followed by a $6 \times n$ listing for each column:

1. value **1** if the electronic state is the upper excited one, **0** otherwise
2. value **1** if the spin-split level is F1, **0** otherwise (F2)
3. the perturbation rotational quantum number J
4. the perturbation maximum energy shift dE in cm^{-1} units
5. the reference for the perturbation data

It is possible to check the file `N2II-1N.txt` for an example on how the perturbations are treated.

Step 6: Define the number of rotational and vibrational levels

[2] This is likely to be updated in the future for extending the simplified modeling of perturbations to other multiplicities.

Once the other steps are finished, scroll down and define the number of rotational and vibrational levels. For simplicity, you can leave the rotational levels defined as 100 and only change the number of vibrational levels. In the next line you can define a limiter maximum vibrational level. This can be useful when you want to add a large number of vibrational transitions in the database (say a 20×20 matrix of $v' \rightarrow v''$ transitions, in case you want to make a broad and large spectral calculation, yet only wish to calculate the more intense transition for the lower states. Instead of having to crop the matrix, you can simply set this limiter ${v', v''}_{max}$ value, for example 10, which will instruct the code to do this automatically, cropping the 20×20 matrix to 10×10 versions. This way you can just adjust this value, depending on what your needs are.

After defining the number of rotational and vibrational levels, you must edit J_E^{max} and J_G^{max} which are the maximum rotational quantum numbers for each vibrational level. If you do not know the exact values for these, you can just insert a high enough number (like for example 999) and then fill as much values as there are vibrational levels (for example for 11 vibrational levels, you will need to input J_E^{max} and J_G^{max} from $v = 0$ to 10). For example, the `CO-4P.txt` file has 11 vibrational levels and so J_E^{max} and J_G^{max} have 11 terms. In any case the code will only calculate lines up to the maximum of either J_E^{max} and J_G^{max}, or the last rotational quantum number (which will be for example $J = 99$ for a number of 100 for the calculated rotational levels), whichever is lower. If you set a limiting ${v', v''}_{max}$ value below, the code will automatically crop the J_E^{max} and J_G^{max} vectors too.

Variables code	Variable
1	$\overline{\nu}_0$
2	B_v
3	$-D_v$
4	H_v
5	L_v
6	M_v
7	N_v
8	γ
9	γ_J
10	γ_{JJ}
11	A_v
12	Y
13	λ
14	λ_J
15	λ_{JJ}
16	y_1
17	y_2

Table 4.5: Correspondence between specific variables in the code and spectral constants.

Step 7: Edit the Franck–Condon factors

In this file, you can also define the Franck–Condon factors. They are displayed in a matrix form $M_{v'v''}$, where v' defines the upper vibrational levels and v'' the lower energy vibrational levels. The matrix has a size $n \times n$, where $n = max(v'_{max}, v''_{max})$. If you do not want to use the Franck–Condon factors in the code calculations, you can set all the matrix components to 1. But even if you do not use these factors, the size of the matrix must be in agreement with the number of vibrational levels defined before. The Franck–Condon factors are only utilized in the special case of a Corona distribution function calculation for the vibrational levels populations, which is seldom carried out.

Step 8: Edit the Einstein coefficients

The Einstein coefficients, also known as transition probabilities must be defined in this file in a matrix form $M_{v'v''}$, where v' defines the upper vibrational levels and v'' the lower energy vibrational levels. As for the Franck–Condon factors defined in the last step, the size of the matrix is defined by the number of vibrational levels defined before.

Once you accomplish all these steps, you have created the first definition file necessary to implement a new species in the database.

4.2.3 Special case for Homonuclear/Fermion transitions

The SPARTAN code is capable of treating a special case of homonuclear molecules for the Fermion case (nuclear spin parameter $0^+/0^-$) where one of each two subsequent even/odd rotational lines are absent. In those cases, it sometimes occurs that two sets of spectroscopic constants, obtained for both odd and even rotational states, are proposed in the literature. The SPARTAN code can account for these differentiated spectral constants (again, this is only valid for Fermions with the nuclear spin parameter $0^+/0^-$, not Bosons with $1^+/1^-$.

In this case all the data from Step 2, 2.a, and 4 is duplicated, with a datasets for even states followed by a dataset for odd states. In this case, a specific identifier has to be included in the `Database.txt` file. For example the label for a $^1\Sigma - ^1\Pi$ will no longer be `1S---1P` but `1SD-1PD` where the label `D` stands for doubled nuclear spin state. For seeing a sample file considering this case, please refer to database file `H2-WED.txt` which treats the Werner $^1\Pi - ^1\Sigma$ transition for the homonuclear H_2 molecule with two different datasets for odd and even states.

4.2.4 Testing your files

The routine `Test_DiatomicFiles.m` can be used for testing the integrity of your new spectral file. Usage is `>>Test_DiatomicFiles('filename','transition code')` Please refer

to appendix D for more details.

Furthermore, the SPARTAN code has some limited capabilities for detection of invalid files and might automatically stop the program execution displaying the message:

The input file (filename) has errors, check for typos and verify that multiplet transitions are not missing fine structure constants.
Click here to stop program execution.

Lastly, if wrong values for spectroscopic constants are inserted, some quantities might be strongly offset. The SPARTAN code makes a limited attempt at checking these inconsistencies. In its current version, the rotational energies are cross-checked. If they exceed some unphysical high value (100,000cm^{-1}; 12.4eV), a warning is displayed during execution[3]. It might be wise in such case to cross-check the obtained results for consistency, and revise the spectral constants datafile for typos.

4.3 Building the datafiles for diatomic species partition functions calculations

Partition functions for diatomic species are calculated in the `Excite2.m` routine, allowing the calculation of the level populations for any arbitrary set of characteristic temperatures $T_{rot}, T_{vib}, T_{exc}$.

We firstly express the population of a specific vibronic level as the product of the populations for each degree of freedom (electronic vibrational and rotational):

$$N_{e,v,J} = N \frac{N_e}{N} \frac{N_{e,v}}{N_e} \frac{N_{e,v,J}}{N_{e,v}} \tag{4.1}$$

In equilibrium conditions, the level populations are related to the partition functions for the different degrees of freedom according to:

$$\frac{N_e}{N} = \frac{Q^e_{el} \sum_{v,J} Q^{e,v}_{vib} Q^{e,v,J}_{rot}}{\sum_{e,v,J} Q^e_{el} Q^{e,v}_{vib} Q^{e,v,J}_{rot}} \tag{4.2a}$$

$$\frac{N_{e,v}}{N_e} = \frac{Q^{e,v}_{vib} \sum_{v,J} Q^{e,v,J}_{rot}}{\sum_{v,J} Q^{e,v}_{vib} Q^{e,v,J}_{rot}} \tag{4.2b}$$

$$\frac{N_{e,v,J}}{N_{e,v}} = \frac{Q^{e,v,J}_{rot}}{\sum_J Q^{e,v,J}_{rot}} \tag{4.2c}$$

[3]Please ignore this warning for the H_2 Lyman and Werner transitions, and the C_2 Swan Bands. The warning is due to the extrapolation of high order polynomial coefficients, but the population of these higher-lying levels is negligible and as such, this occurrence has no visible bearing on the reproduced spectra which remains physically consistent

And the exact individual partition functions for each mode may be written as:

$$Q^e_{el} = g_e \exp\left(-\frac{hc}{k_B T_{exc}} T(e)\right)$$
$$= (2 - \delta_{0,\Lambda})(2S+1) \exp\left(-\frac{hc}{k_B T_{exc}} T(e)\right) \tag{4.3a}$$
$$Q^v_{vib} = g_v \exp\left(-\frac{hc}{k_B T_{vib}} G(v)\right)$$
$$= \exp\left(-\frac{hc}{k_B T_{vib}} G(v)\right) \tag{4.3b}$$
$$Q^J_{rot} = g_J \exp\left(-\frac{hc}{k_B T_{rot}} F_v(J)\right)$$
$$= (2J+1) \exp\left(-\frac{hc}{k_B T_{rot}} F_v(J)\right) \tag{4.3c}$$

4.3.1 Approximations considered in the population routine

Two approximations are carried out in the calculation of 1) the individual vibrational partition functions, and 2) the rotational partition functions summation.

For the vibrational partition functions, we consider that the level energies follow a first-order series (harmonic oscillator approximation) with:

$$E_v = \omega_e \left(v + \frac{1}{2}\right) \tag{4.4}$$

with

$$v_{max} = \frac{D_0}{\omega_e} - \frac{1}{2} \tag{4.5}$$

Here we do not consider the second-order correction $\omega_e x_e$ for the vibrational energies (or any other higher order corrections), since if the condition $(\omega_e^2/4\omega_e x_e > D_e)$ is not met, the level energies will reach a fictious maxima below D_e (one such case is the C_2 $d^3\Pi$ perturbed state). Therefore the harmonic oscillator approximation is preferred as it does not rely in the extrapolation of corrective factors which may lead to singularities [34].

Alternatively, explicit values for the vibrational level energies, up to the dissociation limit, may be supplied, hence avoiding unreliable partition function calculations at high T_{vib}.

For the rotational partition functions sum, the approximation

$$\sum_J Q^{e,v,J}_{rot} \cong \frac{k_B T_{rot}}{hcB_v} = \frac{T_{rot}}{1.4388 B_v} \tag{4.6}$$

is considered.

This approximation holds for $T_{rot} \gg hc/k_B B_v = 1.4388 B_v$. As an example we have $T_{rot} \gg 87.5$K for the ground state of H_2 and $T_{rot} \gg 2.8$K for the ground state of N_2. For most practical applications, except a very low cryogenic temperatures, this approximation will hold easily. We consider a second-order expression for the calculation of the vibrational dependent constant B_v such that $B_v = B_e - \alpha_e (v + 1/2)$.

With these two approximations, we may write the total partition function as:

$$\sum_{e,v,J} Q_{el}^{e}, Q_{vib}^{e,v} Q_{rot}^{e,v,J} = \frac{1}{\sigma} \sum_{e} g_e \exp\left(-\frac{1.4388}{T_{exc}} T(e)\right) \sum_{v=0}^{v_{max}} \exp\left[-\frac{1.4388}{T_{vib}} \omega_e \left(v + \frac{1}{2}\right)\right] \frac{T_{rot}}{1.4388 B_v} \tag{4.7}$$

Here we have added the term $1/\sigma = 1/2$ for homonuclear molecules, accounting for the nuclear spin partition function Q_{nuc} (for heteronuclear molecules $Q_{nuc} = 1$).

4.3.2 File structure

For each diatomic species AB inserted in the code, a file for the molecular energies has to be built. The recommended naming convention for the file is `AB-LEV.txt`. Here we will shortly describe the structure of the file.

Each file starts with two lines:

- Number of molecular electronic levels
- Nuclear spin degeneracy (1 for heteronuclear molecules AB, 2 for homonuclear molecules AA

This is followed by the data required for the calculation of the rovibronic partition functions, for each electronic level.

The structure is as follows:

- Identifier of the electronic level
- Calculation mode for the vibrational partition functions (**0** for explicit energy levels, **1** for harmonic oscillator approximation
- Electronic energy (in cm^{-1})
- v_{max} for mode **0**, ω_e (in cm^{-1}) for mode **1**
- B_e (in cm^{-1})
- α_e (in cm^{-1})
- Electronic level dissociation energy D_0 (in cm^{-1}), with origin of the referential at E(v=0)
- Electronic level degeneracy ($g_e = (2 - \delta_{0,\Lambda})(2S + 1)$)
- The list of $v_{max} + 1$ vibrational energy levels (in cm^{-1})

The more the added upper molecular electronic levels, the more accurate will the calculated partition functions be at higher temperatures.

4.4 Building spectral datafiles for other transitions

This section describes how the other type of radiative transitions can be inserted in the SPARTAN code.

4.4.1 Atomic discrete and continuum transitions

The SPARTAN code adopts a general file structure for discrete (bound-bound) transitions, and the file structure from TOPbase for photoionization (bound-free) transitions.

It is important to note that most databases for Atomic radiative transitions adopt different lists of Atomic levels (whose more energetic levels are usually calculated with differing numerical approaches). Therefore, an important aspect of the atomic data implemented in the spectral database of the SPARTAN code is that **each transition file will have its associated level energies file**. For example, the Atomic Nitrogen discrete transitions file (`N-ATO.txt`) will have an associated level energies file `N-ATO-LEV.txt`), whereas the Atomic Nitrogen photoionization cross-sections file (`N-PI.txt`) will have another associated level energies file `N-PI-LEV.txt`). A comparison of both levels file (`N-ATO-LEV.txt` and `N-PI-LEV.txt`) will show that although they remain very similar for the lower energy levels, there are increasing differences for the higher energy levels.

4.4.1.1 Atomic discrete transitions file structure

Atomic discrete transitions are split into two files: a level file (`AB-ATO-LEV.txt`), and a radiative transitions file (`AB-ATO.txt`).

The structure of the level file `AB-ATO-LEV.txt` is as follows:

- the number of levels (first line)
- labels E and g_e (second line)
- Level energies (in cm^{-1}) and degeneracies

For the atomic transition file `AB-ATO.txt` we have:

- Database identifier (first line)
- Number of transitions and label (third line)
- labels for the columns (fifth line)
- Transition energy (in cm^{-1}); Einstein coefficient (s^{-1}); level index in the levels file (upper and lower state); Energies of the upper and lower states (in cm^{-1}); degeneracies of the upper and lower states

4.4.1.2 Atomic photoionization transitions file structure

For photoionization cross-section files (`AB-PI.txt`), the TOPBase format is to be used "as is", with the small difference that the header has to be removed:

```
================================================
      I  NZ  NE  ISLP  ILV        E(RYD)      NP
================================================
```

and replaced by a line with the number of individual electronic level cross-sections.

The corresponding energy level files (`AB-PI-LEV.txt`) have then to be obtained from the same TOPbase database, and modified to follow the same structure that the atomic species level energy files. **It is very important that the energy level file is issued from TOPbase and not another database such as NIST**, otherwise the program will likely crash or otherwise the results won't be consistent.

4.4.1.3 Atomic photodetachment transitions file structure

For atomic photodetachment, the structure is as follows (example for O^- photodetachment `O-PD.txt` file):

```
11819 Energy_Difference_O_Ground_Level
6 Degeneracy_state_O-(2P)

Wavenumber_(cm-1)_Cross-Section_(m^2)

1.2000e+04 0.0000e-00
...
```

You need to include the energy difference (in cm^{-1}) between the ground A^- state and the ground A state, the degeneracy of the A^- state, and the global photodetachment cross-sections, in two columns with wavenumber (in cm^{-1}) and absorption cross-section (in m^2).

4.4.1.4 Atomic Bremsstrahlung cross-sections

The semi-empirical expressions reported in Sec. 2.2.2.2 for atomic ions, N and O atomic Bremsstrahlung have been hard-coded in the `Bremstr.m` routine, and assigned the tags `N2_Bremstr` `AtoII_Bremstr` and `O2_Bremstr`. the tabulated gaunt-factor for Bremstrahlung transitions, also reported in Sec. 2.2.1.1, is hard-coded in the routine. The routine can be easily modified if new data tables are to be used.

4.4.2 Linear polyatomic discrete transitions

Linear Triatomic discrete transitions are split into two files, just like for atomic and diatomic transitions: a level file (`CO2-LEV.txt`), and a radiative transitions file (`CO2.txt`). For now only the CO2 IR transitions are included, so we will take them as an example.

The level file first three lines indicate:

- The number of isotopes (first line)
- The maximum rotational level of all the transitions (second line)
- labels for the columns (third line)

For each isotope we then have a definition line which gives the numerical reference of the isotope (e.g. 626), the number of levels (e.g. 256), and the abundance of the isotope (e.g. 0.9842)

We then have the same number of lines as the levels indicated for the isotope (e.g. 256). Each line has the following columns:

- Numerical label of the level (ISO+level number)
- Vibrational level label
- level degeneracy (2-$\delta_{0,l}$)
- Rotational constant B_v (in cm^{-1})
- Rotational constant D_v (in cm$^{-1}\times 10^7$)
- Rotational constant H_v (in cm$^{-1}\times 10^{13}$)
- Maximum rotational quantum number J_{max}

The corresponding partial section of the file `CO2-LEV.txt` is presented below

```
8 Isotopes
144 MaxRotLevel
Ref v g(2-d0,l) Gv Bv Dve7 Hve13 Jmax
626 256 0.9842
626001 00001c 1 0.000000 0.39021889 1.33338 0.077 140
...
636 126 0.01106
636001 00001c 1 0.000000 0.39023754 1.33346 0.151 122
636002 01101e 2 648.47803 0.39061133 1.35489 0.497 113
...
```

For the transitions file (such as `CO2.txt`), we have the number of vibrational bands in the first line, and the labels of the columns in the second line. The following columns stand for:

- Band origin $\overline{\nu}_0$ (in cm^{-1})
- The excited band quantum vibrational number v
- The excited band quantum vibrational number l
- Excited vibrational level degeneracy (2-$\delta_{0,l}$)
- Numerical label of the excited vibrational level (ISO+level number)
- Energy of the excited vibrational level (in cm^{-1})
- The ground band quantum vibrational number v
- The ground band quantum vibrational number l
- Ground vibrational level degeneracy (2-$\delta_{0,l}$)
- Numerical label of the ground vibrational level (ISO+level number)
- Energy of the ground vibrational level (in cm^{-1})
- Isotope of the vibrational band
- Isotope numerical label
- Hermann-Wallis coefficient A_1 (in cm^{-1})
- Hermann-Wallis coefficient A_2 (in cm$^{-1}\times 10^5$)
- Hermann-Wallis coefficient A_3 (in cm$^{-1}\times 10^5$)

- Hermann-Wallis coefficient A_Q (in $cm^{-1} \times 10^5$)
- Einstein coefficient $A_{v'v''}$ (s^{-1})

The corresponding partial section of the file `CO2.txt` is presented below

```
613 Transitions
nu0 v'l'2-d0l'Ref_Ev'Ev'v''l''   2-d0l''Ref_Ev''Ev'ISO Ref A1 A2e5
A3e5 AQe5 Avv
471.5112 20003 0 1 626015 2548.36707 11101 1  2 626012 2076.855880
626 1 0.000490 0.898 0 0 0.00831862
...
```

4.4.3 Molecular continuum transitions

4.4.3.1 Diatomic species photoionization/photodissociation cross-sections

For global cross-sections, a two-column file with wavenumber (in cm^{-1}) and absorption cross-sections (in m^2) has to be supplied, without any further data.

For vibration-specific cross-sections (such as for example the O_2 Schumann–Runge continuum (`O2-SRC.txt`), the levels populations are provided by the files `AB-LEV.txt` as for diatomic discrete transitions. The absorption cross-sections file structure is then as follows:

```
LinodaSilva:2013 ...

21 Levels

 v= 0 E(v)= 787.91  115 points

57144.41   2.350e-19
57413.90   3.039e-19
...

 v= 1 E(v)= 2344.58  116 points

55587.74   2.577e-18
55857.24   3.098e-18
...
```

The file structure can be summarized as:

- Identifier tag (first line)
- Number of vibrational quantum numbers v (third line)
- Line including the identification of the vibrational level, its energy (in cm^{-1}), and the number of points n in the cross-section
- n lines with with wavenumber (in cm^{-1}) and absorption cross-section (in m^2)

4.4.3.2 Molecular Bremsstrahlung cross-sections

The tabulated N_2 and O_2 molecular Bremsstrahlung cross-sections $\sigma(\overline{\nu}, T)$, discussed in Sec. 2.2.2.2, have been hard-coded in the `Bremstr.m` routine, and assigned the tags `N2_Bremstr` and `O2_Bremstr`. the tabulated gaunt-factor for Bremstrahlung transitions, as discussed in Sec. 2.2.1.1, is also hard-coded in the routine. The routine can be easily modified if new data tables are to be used.

4.5 Linking new spectral datafiles to the SPARTAN database

Once new spectral datafiles have been produced, there is the need to link them to the general database of the code. This sections provides a step-by-step tutorial on how to achieve this.

Step 1: Adding species to the code database folder

The first step is to place the levels and radiative transitions files in the folder named DATABASE.

Step 2: Adding transitions to the Inputs file

The new transitions of the species you wish to consider in the code must be added to the Inputs file. First open the `INPUTS` folder, then open the `Inputs.txt` file. This file contains all the input parameters for the simulation: apparatus function, minimum and maximum wavelengths (in Å), temperatures T_{rot}, T_{vib}, and T_{exc} (in K). If you are using the GUI interface, the values of these parameters are the ones you defined and you can always change them directly using the interface. If you do not wish to use the GUI interface, you must set new values by editing this file. The number density of the species (in m^{-3}) must always be defined here and you must not forget to update its value if it is set to zero. Also included in the Inputs file are the chemical symbol, the molar mass (in kg mol^{-1}) and the radius (in Å) of the species.

After the input parameters, the number of transitions considered by the code is shown. Do not forget to sum the number of transitions you are adding to the defined value. Then at the end of the file you must add the name of the transitions you want to implement (ex: `Ar_Atomic`). Right before the name you must choose if you want these transitions to be selected for calculation (set **1**) or not (set **0**). At this point it does not really matter which value you choose, you can always change it latter by editing the file or by selecting the transitions names in the GUI interface.

Step 3: Editing the GUI interface

Once you finished editing the `Inputs.txt` file, the GUI interface must be updated (see Fig. 1.1). Open and edit the `Guinterface.txt` file located in the INPUTS folder. This file defines the name, the color and the position of the transitions names in the GUI interface. In the first column you must add the name of the new transitions. The column is divided in five sections depending on the type of radiation (Atomic Discrete, Atomic continuum, etc). Scroll down and at the end of the file you will find several available places (placeholders) to add the transitions with already defined positions and colors. In this case, you just have to insert the name of the transition in the first column.

If you wish to add more than the placeholder transitions you must add a new line and define:

- the transition name
- the RGB colour of the name
- the position of the name in the window (Xpos and Ypos)
- the length (L) and width (W) of the name.

If you need to add a new label, don't forget to update the number of labels at the beginning of the `Guinterface.txt` file.

Step4: Editing the Database file

The `Database.txt` file, located in the INPUTS folder, lists and links the overall definition files. Open and you will immediately see the number of transitions considered by the code. As before, do not forget to sum the number of transitions you are adding. To add a new radiative system you must add a new line at the end of the file following the steps:

- **Column 1**: Introduce the name of the transition
- **Column 2**: Write the chemical symbol of the species
- **Column 3**: Introduce the molar mass of the species (in kg mol^{-1})
- **Column 4**: Introduce the name of the file defining all the radiative transitions of the species (see step 1)
- **Column 5**: Introduce the name of the file containing all the energy levels of the species (see step 1)
- **Column 6**: Introduce the identifier of the upper level of the transition in the levels file, referred to in column 5. It corresponds to the number of the row of the upper level (ex: the level with the lowest energy is indicated in the first row, and so the identifier is 1)
- **Column 7**: Introduce the identifier of the lower level of the transition in the levels file. It is defined as the previous identifier
- **Column 8**: Define the type of transition (ex: `BoundMO`, `BoundDI`, `PhoIoMO`, `Bremstr`, etc)
- **Column 9**: Define a detailed identifier of the transition (ex: `ATO-ATO`, `2S---2P`, `BremsDI`, etc)
- **Column 10**: Define the population of the levels (only `Boltzmann` in the current version)

Labels Col. 8	Transitions type	Labels Col. 9	Transitions type
`BoundMO`	Bound Monoatomic	`ATO-ATO`	Bound Monoatomic
`BoundDI`	Bound Diatomic	`1S---1S, 1SD-1SD`	$^1\Sigma$–$^1\Sigma$
		`1S---1P, 1SD-1PD`	$^1\Sigma$–$^1\Pi$
		`1P---1S, 1PD-1SD`	$^1\Pi$–$^1\Sigma$
		`1P---1P, 1PD-1PD`	$^1\Pi$–$^1\Pi$
		`1P---1D, 1PD-1DD`	$^1\Pi$–$^1\Delta$
		`1D---1P, 1DD-1PD`	$^1\Delta$–$^1\Pi$
		`1D---1D, 1DD-1DD`	$^1\Delta$–$^1\Delta$
		`2S---2S, 2SD-2SD`	$^2\Sigma$–$^2\Sigma$
		`2S---2P, 2SD-2PD`	$^2\Sigma$–$^2\Pi$
		`2P---2S, 2PD-2SD`	$^2\Pi$–$^2\Sigma$
		`2P---2P, 2PD-2PD`	$^2\Pi$–$^2\Pi$
		`3S---3S, 3SD-3SD`	$^3\Sigma$–$^3\Sigma$
		`3S---3P, 3SD-3PD`	$^3\Sigma$–$^3\Pi$
		`3P---3S, 3PD-3SD`	$^3\Pi$–$^3\Sigma$
		`3P---3P, 3PD-3PD`	$^3\Pi$–$^3\Pi$
`BoundPO`	Bound Polyatomic	`POL-POL`	Bound Polyatomic
`PhoIoMO`	Photoionization Monoatomic	`TOPBASE`	Topbase Cross-sections
`PhoDeMO`	Photodetachment Monoatomic	`PhoDeSa`	Photodetachment, Saha equilibrium
`PhoIoDI`	Photoionization Diatomic	`PhotoTo`	Photoionization, global cross-section
		`PhotoVi`	Photoionization, v-dependent cross-section
`PhoDiDI`	Photodissociation Diatomic	`PhotoTo`	Photodissociation, global cross-section
		`PhotoVi`	Photodissociation, v-dependent cross-section
`Bremstr`	Bremsstrahlung	`BremsMO`	Bremsstrahlung Monoatomic
		`BremsDI`	Bremsstrahlung Diatomic

Table 4.6: Label identifiers of the different transition types encoded in the SPARTAN code

The different possible labels are summarized in Table 4.6.

Once you accomplish all these steps, you are ready to run the code and simulate radiative transitions of the new species. If error messages are displayed when running the code, verify if the number of transitions is correct and has been updated in the `Inputs.txt` and in the `Database.txt` files. If the code runs normally but does not calculate a simulated spectrum of the species, check if the number density of the species in the `Inputs.txt` file has been given a value different from zero.

4.6 Summary

At the outset of this section, one should be capable to fully customize the SPARTAN code and update its spectral database. In practice though, it is likely that a great deal of trial and error should be expected from someone not familiarized with the code. Furthermore, the disparity of values that are found when updating a spectroscopic database (from the Einstein coefficients with powers up to 10^8 to higher order polynomial corrections to level energies with powers down to 10^{-10} and below) generally means that most typos will be fatal and will make the program crash. As with the general topic of reproducing experimental spectra through numerical models, familiarizing oneself and updating the database of the SPARTAN code could well become a so-called "labor of love" at first. Yet, as the saying goes, there is no gain without pain. Best of luck to everyone!

Appendix A

References for the SPARTAN Spectral Database

In this appendix, the references for the datasets included in the current version of the SPARTAN database are presented, except for the bound diatomic transitions, which have self-contained information on the spectral data references.

Table A.1 presents all the simulated transitions in the current version of the SPARTAN code and their corresponding references. Table A.2 presents all the references that have been consulted for building the partition function files `AB-LEV.txt` for each radiative species. The reader should consult the files comments for more details on the each spectroscopic constant reference.

Transition	Reference
Bound Atomic Transitions	
H, C, C^+, N, N^+, O, O^+, Ar, Ar^+, Hg, Xe, Xe^+	NIST database, [36]
Bound Diatomic Transitions	
H_2 Lyman, Werner	See database file headers
C_2 Swan, Philips, Mulliken, Deslandres–D'Azambuja, Fox–Herzberg, Ballik–Ramsay	
CN Violet, Red	
CO Infrared, 4^{th} Positive, Angstrom, 3^{rd} Positive, Triplet, Asundi	
CO^+ Comet Tail	
N_2 1^{st}, 2^{nd} Positive	
N_2^+ 1^{st} Negative	
NH AX	
NO γ, β, δ, ϵ, β', γ'	
O_2 Schumann–Runge	
OH AX	
Bound Linear Polyatomic Transitions	
CO_2 Infrared	[16, 1]
Atomic Photoionization Transitions	
H, C, C^+, N, N^+, O, O^+, Ar, Ar^+	TOPBase database, [37]
Atomic Photodetachment Transitions	
C^-, N^-, O^-	[38], [28], [28]
Molecular Photoionization Transitions	
CO_2, CO, CN, C_2, N_2, O_2, NO	[39], [40, 41], [40], [40], [42], [40, 43]
Molecular Photodissociation Transitions	
O_2 Schumann-Runge Continuum	Lino da Silva (2013), unpublished
Atomic and Molecular Bremsstrahlung Transitions	
Atomic Ions, N, O, N_2, O_2	[26], [27], [27], [28], [28]

Table A.1: List of Radiative Systems included in the current version of the SPARTAN code Database

Species	References
H_2	[44, 45, 46]
C_2	[44, 47, 48, 49]
CN	Lino da Silva, unpublished, [44]
CO	[44, 50, 51, 52, 53, 54, 55]
CO^+	[44, 53]
N_2	[34, 28, 56, 57]
N_2^+	[28, 56]
NH	[44, 58]
NO	[28, 56]
O_2	[28, 56]
O_2^+	[28, 56]
OH	[44, 59, 60]

Table A.2: List of Radiative Systems included in the current version of the SPARTAN code Database

Appendix B

Expressions and Approximations for the Computed Hönl–London Factors

This appendix describes the approaches that have been implemented in the SPARTAN code for the calculation of the Hönl–London Factors for bound diatomic transitions.

Depending on the spin multiplicity of the upper and lower electronic states of the diatomic molecule, the number of rotational branches may go from the 3 single (P, Q, R) branches for singlet transitions, up to 12 branches for doublet transitions (6 main branches P_1, P_2, Q_1, Q_2, R_1, R_2 and 6 satellite branches ${}^{O}P_{12}$, ${}^{Q}P_{21}$, ${}^{P}Q_{12}$, ${}^{R}Q_{21}$, ${}^{Q}R_{12}$, ${}^{S}R_{21}$), and up to 27 branches for triplet transitions (9 main branches P_1, P_2, P_3, Q_1, Q_2, Q_3, R_1, R_2, R_3 and 18 satellite branches ${}^{Q}P_{21}$, ${}^{R}Q_{21}$, ${}^{S}R_{21}$, ${}^{R}P_{31}$, ${}^{S}Q_{31}$, ${}^{T}R_{31}$, ${}^{O}P_{12}$, ${}^{P}Q_{12}$, ${}^{Q}R_{12}$, ${}^{Q}P_{32}$, ${}^{R}Q_{32}$, ${}^{S}R_{32}$, ${}^{N}P_{13}$, ${}^{O}Q_{13}$, ${}^{P}R_{13}$, ${}^{O}P_{23}$, ${}^{P}Q_{23}$,${}^{Q}R_{23}$).

Some special cases are considered in the SPARTAN code. Firstly, some branches have very low transition probabilities and may be safely neglected, and secondly, some branches may be indistinguishable except at very high spectral resolution (for example, Σ states fine-structure constants have values typically below 0.01cm^{-1} and appear superposed in practice. The SPARTAN code takes advantage of this, so that only the 6 and 9 main branches for doublet and triplet transitions are in practice calculated. This has been verified to have no noticeable effect on the obtained results, but future versions of the code might levy such a restriction, as improved computational power becomes available.

B.1 Applied approximations

B.1.1 Neglecting line spin-splitting effects for satellite lines involving Σ states

If the separation of multiplet lines is much smaller than their widths, such lines can be accurately superposed into one singlet line. The SPARTAN code takes advantage of this for coalescing perpendicular transitions (transitions with a change of fine-structure state, e.g. ${}^{R}Q_{32}$) with the corresponding parallel transitions (e.g. R_2).

This approach is usually valid for multiplet Σ states, which have small spin-splitting factors allowing transitions between such states to be accurately modeled as singlet states.

A good example can be given for a ${}^{2}\Sigma - {}^{2}\Sigma$ transition. For this case, the separation between two doublet lines (in Å) is given by:

$$\Delta\lambda \simeq 10^{8} \frac{(\gamma_E - \gamma_G)(J + \frac{1}{2})}{\bar{\nu}_0^2} \tag{B.1}$$

For the CN violet system[1], this is equivalent to a line splitting of 0.14 Å for a rotational value as high as J=100. In classical spectrometry applications, this transition can be accurately simulated as a singlet transition, reducing calculation times without a loss of accuracy. For triplet Σ transitions, a slightly more complicated relationship can also be determined to evaluate whether the analyzed transitions can be accurately modeled as singlet transitions (according to the transition γ and λ constants).

The limits of this assumption occur when the spin-splitting of the studied states is no more negligible, and self-absorption of the spectra is high. In this case, a comparison of a simulated spectrum using this simplification with a simulated spectrum accounting for spin-splitting shows non-negligible differences. Therefore this approximation is in general no longer valid for multiplet states with larger spin-splitting values such as Π and Δ.

Table B.1 lists the branches that can be coalesced when the spin-splitting of the Σ state is neglected.

B.1.2 Neglecting weaker rotational branches

Assuming a Boltzmann equilibrium of the rotational levels, a line rotational intensity may be written as

$$S(J) = \frac{(2J+1)\exp\left(-\frac{hc}{kT_{rot}}F(J)\right)}{Q_{rot}} \frac{S^{\Lambda' J'}_{\Lambda'' J''}}{2J+1} \tag{B.2}$$

Because each rotational state has a $g_J = 2J+1$ degeneracy, the ground state will not be the most populated state. As an example, at room temperature, typically the most populated rotational level is around $J = 7 - 10$, whereas at a 2000 K temperature, the most populated level is around $J = 20$.

[1] the spin-spin correction is $\gamma = 7.26 \cdot 10^{-3}\text{cm}^{-1}$ for the ($X^2\Sigma$,v=0) state, and $\gamma = 17.16 \cdot 10^{-3}\text{cm}^{-1}$ for the ($B^2\Sigma$,v=0) state [35]

$^2\Sigma - ^2\Pi$	$^2\Pi - ^2\Sigma$	$^3\Sigma - ^3\Pi$	$^3\Pi - ^3\Sigma$
$^PQ_{12} = P_2$	$^PQ_{12} = P_1$	$^TR_{31} = P_1$	$^RQ_{21} = P_2$
$^QP_{21} = Q_1$	$^QR_{12} = Q_1$	$^RQ_{21} = P_1$	$^RQ_{32} = P_3$
$^QR_{12} = Q_2$	$^QP_{21} = Q_2$	$^RQ_{32} = P_2$	$^TR_{31} = P_3$
$^RQ_{21} = R_1$	$^RQ_{21} = R_2$	$^SR_{21} = Q_1$	$^OP_{12} = Q_1$
		$^OP_{12} = Q_2$	$^OP_{23} = Q_2$
		$^SR_{32} = Q_2$	$^SR_{21} = Q_2$
		$^OP_{23} = Q_3$	$^SR_{32} = Q_3$
		$^PQ_{12} = R_2$	$^NP_{13} = R_1$
		$^NP_{13} = R_3$	$^PQ_{12} = R_1$
		$^PQ_{23} = R_3$	$^PQ_{23} = R_2$

Table B.1: Coalesced rotational branches for multiplet $\Sigma - \Pi$ transitions when neglecting spin-splitting for the Σ state

As some rotational branches have smaller magnitudes than others, only reaching equivalent magnitudes for the first rotational levels (typically $J \leq 5$), we may examine the expression for the rotational line strength to check whether these may be safely neglected. An example for a $^3\Sigma \leftrightarrow ^3\Pi$ transition at a 300 K gas temperature is presented in Fig. B.1

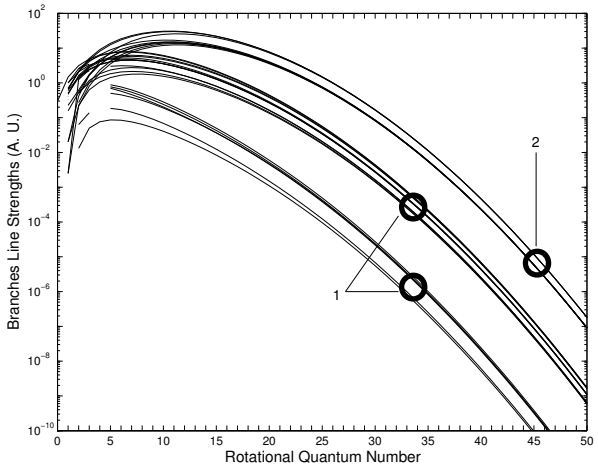

Figure B.1: Rotational line strengths of the different branches of a $^3\Sigma \leftrightarrow ^3\Pi$ transition for a Boltzmann distribution of the rotational levels at a characteristic temperature of 300 K.

The ratio of the peak intensities between the second and first group of rotational branches is 3.3 for this case. For a 2000 K temperature, the same calculation results in a 15.8 ratio. Therefore omitting such weaker rotational branches for spectral calculations of high temperature gases has in most cases a negligible effect on the simulated spectra.

Table B.2 lists the weaker rotational branches that can be neglected for

doublet and triplet transitions.

${}^2\Delta' \leftrightarrow {}^2\Delta''$	${}^3\Delta' \leftrightarrow {}^3\Delta''$		
${}^OP_{12}$	${}^QP_{21}$	${}^RP_{31}$	${}^OP_{12}$
${}^QR_{12}$	${}^RQ_{21}$	${}^SQ_{31}$	${}^PQ_{12}$
${}^QP_{21}$	${}^SR_{21}$	${}^TR_{31}$	${}^QR_{12}$
${}^SR_{21}$	${}^OP_{23}$	${}^QP_{32}$	${}^NP_{13}$
	${}^PQ_{23}$	${}^RQ_{32}$	${}^OQ_{13}$
	${}^QR_{23}$	${}^SR_{32}$	${}^PR_{13}$

Table B.2: Weak rotational branches for doublet and triplet transitions

B.2 First Rotational Lines intensities

For $J < \Lambda + S$, Hönl-London Factors have to be calculated taking into account a less than $2S+1$ dimensional space. For such so-called "First Rotational Lines", the usual expressions for the Hönl–London Factors do not apply, and specific expressions, proposed by Schadee [61], have to be considered. These specific expressions are accounted for in the SPARTAN code, for the corresponding first rotational lines.

B.3 Expressions for the intermediary a–b case Hönl-London Factors utilized in the SPARTAN code

The SPARTAN code always considers a set of Hönl-London Factors for an intermediary Hünd $a-b$ case. This allows the code to accurately describe radiative processes at both low temperatures (typically Hünd case a) and high temperatures (typically Hünd case b).

General expressions for multiplet transitions for an intermediary Hünd $a-b$ case are provided by Kovacs [62]. We use these expressions overall, except for ${}^2\Sigma \leftrightarrow {}^2\Sigma$ transitions, which always belong to Hünd b case, with simplified expressions provided by Schadee [63]. Expressions for ${}^2\Sigma \leftrightarrow {}^2\Pi$ transitions, for an intermediary Hünd $a-b$ case are provided by Arnold [64]. Simplified expressions for the ${}^3\Sigma \leftrightarrow {}^3\Sigma$ transitions, which always belong to Hünd b case, are provided by Tatum [65]. Finally, expressions for ${}^3\Sigma \leftrightarrow {}^3\Pi$ transitions for the intermediary Hünd $a-b$ case are provided by Budò [66].

The analytical expressions are presented in Tabs. B.3–B.9. Whenever the specific upper and lower levels index $'$ and $''$ are not specifically reported, it is to be assumed that the variables report to the lower state $''$. The normalisation factor for the presented Hönl-London Factors is $(2-\delta_{0,\Lambda'})(2S+1)(2J+1)$

	$\Delta\Lambda = -1$	$\Delta\Lambda = 0$	$\Delta\Lambda = +1$
$P(J)$	$\frac{(J+\Lambda)(J+\Lambda-1)}{2J}$	$\frac{(J+\Lambda)(J-\Lambda)}{J}$	$\frac{(J-\Lambda-1)(J-\Lambda)}{2J}$
$Q(J)$	$\frac{(J+\Lambda)(J-\Lambda+1)(2J+1)}{2J(J+1)}$	$\frac{\Lambda^2(2J+1)}{J(J+1)}$	$\frac{(J-\Lambda)(J+\Lambda+1)(2J+1)}{2J(J+1)}$
$R(J)$	$\frac{(J-\Lambda+2)(J-\Lambda+1)}{2(J+1)}$	$\frac{(J+\Lambda+1)(J-\Lambda+1)}{J+1}$	$\frac{(J+\Lambda+1)(J+\Lambda+2)}{2(J+1)}$

Table B.3: Hönl-London factors for singlet transitions

Transitions	Hönl-London Factors	
$P_{1,2}(J)$	$\frac{J(J+1)}{2J+1}$	$\frac{J(J-1)}{2J-1}$
$R_{1,2}(J)$	$\frac{(J+1)(J+2)}{2J+3}$	$\frac{J(J+1)}{2J+1}$
${}^{R}Q_{21}(J)$, ${}^{Q}R_{12}(J)$	$\frac{(J+1)}{(2J+1)(2J+3)}$	$\frac{J}{(2J-1)(2J+1)}$

Table B.4: Hönl-London factors for ${}^2\Sigma - {}^2\Sigma$ transitions

Transition		Hönl-London Factors
${}^2\Sigma - {}^2\Pi$	${}^2\Pi - {}^2\Sigma$	
$P_2\ (J)$	$R_2\ (J-1)$	$\frac{(2J+1)^2 \pm (2J+1)U(4J^2+4J-7+2Y)}{16J}$
${}^{Q}P_{21}(J)$	${}^{Q}R_{12}(J-1)$	
${}^{O}P_{12}(J)$	${}^{S}R_{21}(J-1)$	$\frac{(2J+1)^2 \mp (2J+1)U(4J^2+4J+1-2Y)}{16J}$
$P_1\ (J)$	$R_1\ (J-1)$	
$Q_2\ (J)$	$Q_2\ (J)$	$\frac{(2J+1)[(4J^2+4J-1) \pm U(8J^3+12J^2-2J+1-2Y)]}{16J(J+1)}$
${}^{R}Q_{21}(J)$	${}^{P}Q_{12}(J)$	
${}^{P}Q_{12}(J)$	${}^{R}Q_{21}(J)$	$\frac{(2J+1)[(4J^2+4J-1) \mp U(8J^3+12J^2-2J-7+2Y)]}{16J(J+1)}$
$Q_1\ (J)$	$Q_1\ (J)$	
$R_2\ (J)$	$P_2\ (J+1)$	$\frac{(2J+1)^2 \pm (2J+1)U(4J^2+4J+1-2Y)}{16(J+1)}$
${}^{S}R_{21}(J)$	${}^{O}P_{12}(J+1)$	
${}^{Q}R_{12}(J)$	${}^{Q}P_{21}(J+1)$	$\frac{(2J+1)^2 \mp (2J+1)U(4J^2+4J-7+2Y)}{16(J+1)}$
$R_1\ (J)$	$P_1\ (J+1)$	
$Y = \frac{A_v}{B_v}$		
$U = [Y^2 - Y + (2J+1)^2]^{-1/2}$		

Table B.5: Hönl-London factors for ${}^2\Sigma - {}^2\Pi$ transitions

Transition	Hönl-London Factors
$P_1\ (J)$	$\frac{(J-\frac{3}{2})(J+\frac{3}{2})}{4JC'^{-}(J-1)C''^{-}(J)}[u'^{-}(J-1)u''^{-}(J)+4(J-\frac{1}{2})(J+\frac{1}{2})]^2$
$Q_1\ (J)$	$\frac{J+\frac{1}{2}}{2J(J+1)C'^{-}(J)C''^{-}(J)}[\frac{3}{2}u'^{-}(J)u''^{-}(J)+2(J-\Lambda+\frac{1}{2})(J+\frac{3}{2})]^2$
$R_1\ (J)$	$\frac{(J-\frac{1}{2})(J+\frac{5}{2})}{4(J+1)C'^{-}(J+1)C''^{-}(J)}[u'^{-}(J+1)u''^{-}(J)+4(J+\frac{1}{2})(J+\frac{3}{2})]^2$
${}^{Q}P_{21}(J)$	$\frac{(J-\frac{3}{2})(J+\frac{3}{2})}{4JC'^{+}(J-1)C''^{-}(J)}[u'^{+}(J-1)u''^{-}(J)-4(J-\frac{1}{2})(J+\frac{1}{2})]^2$
${}^{R}Q_{21}(J)$	$\frac{J+\frac{1}{2}}{2J(J+1)C'^{+}(J)C''^{-}(J)}[\frac{3}{2}u'^{+}(J)u''^{-}(J)-2(J-\frac{1}{2})(J+\frac{3}{2})]^2$
${}^{S}R_{21}(J)$	$\frac{(J-\frac{1}{2})(J+\frac{5}{2})}{4(J+1)C'^{+}(J+1)C''^{-}(J)}[u'^{+}(J+1)u''^{-}(J)-4(J+\frac{1}{2})(J+\frac{3}{2})]^2$
${}^{O}P_{12}(J)$	$\frac{(J-\frac{3}{2})(J+\frac{3}{2})}{4JC'^{-}(J-1)C''^{+}(J)}[u'^{-}(J-1)u''^{+}(J)-4(J-\frac{1}{2})(J+\frac{1}{2})]^2$
${}^{P}Q_{12}(J)$	$\frac{J+\frac{1}{2}}{2J(J+1)C'^{-}(J)C''^{+}(J)}[\frac{3}{2}u'^{-}(J)u''^{+}(J)-2(J-\frac{3}{2})(J+\frac{3}{2})]^2$
${}^{Q}R_{12}(J)$	$\frac{(J-\frac{1}{2})(J+\frac{5}{2})}{4(J+1)C'^{-}(J+1)C''^{+}(J)}[u'^{-}(J+1)u''^{+}(J)-4(J+\frac{1}{2})(J+\frac{3}{2})]^2$
$P_2\ (J)$	$\frac{(J-\frac{3}{2})(J+\frac{3}{2})}{4JC'^{+}(J-1)C''^{+}(J)}[u'^{+}(J-1)u''^{+}(J)+4(J-\frac{1}{2})(J+\frac{1}{2})]^2$
$Q_2\ (J)$	$\frac{J+\frac{1}{2}}{2J(J+1)C'^{+}(J)C''^{+}(J)}[\frac{3}{2}u'^{+}(J)u''^{+}(J)+2(J-\frac{1}{2})(J+\frac{3}{2})]^2$
$R_2\ (J)$	$\frac{(J-\frac{1}{2})(J+\frac{5}{2})}{4(J+1)C'^{+}(J+1)C''^{+}(J)}[u'^{+}(J+1)u''^{+}(J)+4(J-\frac{1}{2})(J+\frac{3}{2})]^2$
$u^{\pm}(J)=\sqrt{Y(Y-4)+4\left(J+\frac{1}{2}\right)^2}\pm(Y-2)$	$u'\leftrightarrow Y'\ -\ u''\leftrightarrow Y''$
$C^{\pm}(J)=\frac{1}{2}\left\{u^{\pm}(J)^2+4\left[\left(J+\frac{1}{2}\right)^2-1\right]\right\}$	$C'\leftrightarrow u'\ -\ C''\leftrightarrow u''$

Table B.6: Hönl-London factors for ${}^2\Pi-{}^2\Pi$ transitions

Transitions	Hönl-London Factors		
$P_{1,2,3}(J)$	$\frac{(J-1)(2J+1)}{2J+1}$	$\frac{(J-1)(J+1)}{J}$	$\frac{(J+1)(2J-1)}{2J+1}$
$R_{1,2,3}(J)$	$\frac{J(2J+3)}{2J-1}$	$\frac{J(J+2)}{J+1}$	$\frac{(J+2)(2J+1)}{2J+3}$
${}^{P}R_{13}(J),\ {}^{P}Q_{12}(J)$	$\frac{1}{(J+1)(2J+1)(2J+3)}$	$\frac{1}{J}$	
${}^{P}Q_{23}(J),\ {}^{R}Q_{21}(J)$	$\frac{1}{(J+1)}$	$\frac{1}{J}$	
${}^{R}Q_{32}(J),\ {}^{R}P_{31}(J)$	$\frac{1}{(J+1)}$	$\frac{1}{J(2J-1)(2J+1)}$	

Table B.7: Hönl-London factors for ${}^3\Sigma-{}^3\Sigma$ transitions

Transition		Hönl-London Factors
$^3\Sigma - ^3\Pi$	$^3\Pi - ^3\Sigma$	
$P_1\ (J)$	$R_1\ (J-1)$	$\frac{(J^2-1)[(J+1)u_1-Y+2J^2]^2}{(2J-1)C_1(J)}$
$Q_1\ (J)$	$Q_1\ (J)$	$\frac{[(J^2+J-1)u_1+(Y-2)+2J(J^2-1)]^2}{JC_1(J)}$
$R_1\ (J)$	$P_1\ (J+1)$	$\frac{J[J(J+2)u_1+(J+2)(Y-2)+2(J-1)(J+1)^2]^2}{(J+1)(2J+3)C_1(J)}$
$^QP_{21}(J)$	$^QR_{12}(J-1)$	$\frac{(J^2-1)[(J+1)(Y-2)-u_1]^2}{JC_1(J)}$
$^RQ_{21}(J)$	$^PQ_{12}(J)$	$\frac{(2J+1)[(J^2+J-1)(Y-2)+u_1)]^2}{J(J+1)C_1(J)}$
$^SR_{21}(J)$	$^OP_{12}(J+1)$	$\frac{J(J+2)[J(Y-2)+u_1]^2}{(J+1)C_1(J)}$
$^RP_{31}(J)$	$^PR_{13}(J-1)$	$\frac{(J-1)^2(J+1)[(J+1)u_1-(Y-2)-2J(J+1)]^2}{J(2J-1)C_1(J)}$
$^SQ_{31}(J)$	$^OQ_{13}(J)$	$\frac{[(J^2+J-1)u_1+(Y-2)-2(J-1)(J+1)^2]^2}{(J+1)C_1(J)}$
$^TR_{31}(J)$	$^NP_{13}(J+1)$	$\frac{J(J+2)[Ju_1+Y-2J^2]^2}{(2J+3)C_1(J)}$
$^OP_{12}(J)$	$^SR_{21}(J-1)$	$\frac{2(J^2-1)Y^2}{(2J-1)C_2J}$
$^PQ_{12}(J)$	$^RQ_{21}(J)$	$\frac{2[J(Y-2)-2]^2}{JC_2(J)}$
$^QR_{12}(J)$	$^QP_{21}(J+1)$	$\frac{2J[(J+1)Y-2(2J+3)]^2}{(J+1)(2J+3)C_2(J)}$
$P_2\ (J)$	$R_2\ (J-1)$	$\frac{(8J-1)(J+1)^3)}{JC_2(J)}$
$Q_2\ (J)$	$Q_2\ (J)$	$\frac{8(2J+1)(J^2+J-1)^2}{J(J+1)C_2(J)}$
$R_2\ (J)$	$P_2\ (J+1)$	$\frac{8J^3(J+2)}{(J+1)C_2(J)}$
$^QP_{32}(J)$	$^QR_{23}(J-1)$	$\frac{2(J+1)[J(Y-4)+2]^2}{J(2J-1)C_2(J)}$
$^RQ_{32}(J)$	$^PQ_{23}(J)$	$\frac{2[(J+1)Y-2J]^2}{(J+1)C_2(J)}$
$^SR_{32}(J)$	$^OP_{23}(J+1)$	$\frac{2J(J+2)Y^2}{(2J+3)C_2(J)}$
$^NP_{13}(J)$	$^TR_{31}(J-1)$	$\frac{(J^2-1)[(J+1)u_3+(Y-2)-2J(J+2)]^2}{(2J-1)C_3(J)}$
$^OQ_{13}(J)$	$^SQ_{31}(J)$	$\frac{[(J^2+J-1)u_3-(Y-2)-2J^2(J+2)]^2}{JC_3(J)}$
$^PR_{13}(J)$	$^RP_{31}(J+1)$	$\frac{J(J+2)^2[Ju_3-(Y-2)-2J(J+1)]^2}{(J+1)(2J+3)C_3(J)}$
$^OP_{23}(J)$	$^SR_{32}(J-1)$	$\frac{(J^2-1)[u_3+(J+1)(Y-2)]^2}{JC_3(J)}$
$^PQ_{23}(J)$	$^RQ_{32}(J)$	$\frac{(2J+1)[(J^2+J+1)(Y-2)-u_3]^2}{J(J+1)C_3(J)}$
$^QR_{23}(J)$	$^QP_{32}(J+1)$	$\frac{J(J+2)[J(Y-2)-u_3]^2}{(J+1)C_3(J)}$
$P_3\ (J)$	$R_3\ (J-1)$	$\frac{(J+1)[(J^2-1)u_3+(J-1)(Y-2)+2J^2(J+2)]^2}{J(2J-1)C_3(J)}$
$Q_3\ (J)$	$Q_3\ (J)$	$\frac{[(J^2+J-1)u_3-(Y-2)+2J(J+1)(J+2)]^2}{(J+1)C_3(J)}$
$R_3\ (J)$	$P_3\ (J+1)$	$\frac{J(J+2)[Ju_3-(Y-2)+2J(J+2)]^2}{(2J+3)C_3(J)}$

$$u_1(J) = \sqrt{Y(Y-4)+4J^2}$$
$$u_3(J) = \sqrt{Y(Y-4)+4(J+1)^2}$$
$$C_1(J) = J(J+1)Y(Y-4)+2(2J+1)(J-1)J(J+1)$$

$$C_2(J) = Y(Y-4) + 4J(J+1)$$
$$C_3(J) = (J-1)(J+2)Y(Y-4) + 2(2J+1)J(J+1)(J+2)$$

Table B.8: Hönl-London factors for $^3\Sigma - ^3\,\Pi$ transitions

Transition	Hönl-London Factors
$P_1\ (J)$	$\frac{(J-1)(J+1)}{16JC_1'(J-1)C_1''(J)}\left[\begin{array}{c} J^2u_1'^+(J-1)u_1''^+(J) \\ +\ (J-2)(J+2)u_1'^-(J-1)u_1''^-(J) \\ +8J(J-2)(J-1)(J+1)\end{array}\right]^2$
$Q_1\ (J)$	$\frac{2J+1}{4J(J+1)C_1'(J)C_1''(J)}\left[(J-1)(J+2)u_1'^-(J)u_1''^-(J) + 4(J-1)^2(J+1)^2\right]^2$
$R_1\ (J)$	$\frac{J(J+2)}{16(J+1)C_1'(J+1)C_1''(J)}\left[\begin{array}{c} (J+1)^2u_1'^+(J+1)u_1''^+(J) \\ +\ (J-1)(J+3)u_1'^-(J+1)u_1''^-(J) \\ +8J(J-1)(J+1)(J+2)\end{array}\right]^2$
${}^QP_{21}(J)$	$\frac{(J-1)(J+1)}{2JC_2'(J-1)C_1''(J)}\left[\begin{array}{c} J^2u_1''^+(J) - (J-2)(J+2)u_1''^-(J) \\ -2(J-1)(J+1)(Y'-2)\end{array}\right]^2$
${}^RQ_{21}(J)$	$\frac{2(2J+1)}{J(J+1)C_2'(J)C_1''(J)}\left[(J-1)(J+2)u_1''^-(J) + (J-1)(J+1)(Y'-2)\right]^2$
${}^SR_{21}(J)$	$\frac{J(J+2)}{2(J+1)C_2'(J+1)C_1''(J)}\left[\begin{array}{c} (J+1)^2u_1''^+(J) - (J-1)(J+3)u_1''^-(J) \\ -2(J-1)(J+1)(Y'-2)\end{array}\right]^2$
${}^RP_{31}(J)$	$\frac{(J-1)(J+1)}{16JC_3'(J-1)C_1''(J)}\left[\begin{array}{c} J^2u_3'^-(J-1)u_1''^+(J) \\ +\ (J-2)(J+2)u_3'^+(J-1)u_1''^-(J) - 8(J-1)^2(J+1)^2\end{array}\right]^2$
${}^SQ_{31}(J)$	$\frac{2J+1}{4J(J+1)C_3'(J)C_1''(J)}\left[(J-1)(J+2)u_3'^+(J)u_1''^-(J) - 4J(J-1)(J+1)(J+2)\right]^2$
${}^TR_{31}(J)$	$\frac{J(J+2)}{16(J+1)C_3'(J+1)C_1''(J)}\left[\begin{array}{c} (J+1)^2u_3'^-(J+1)u_1''^+(J) \\ +\ (J-1)(J+3)u_3'^+(J+1)u_1''^-(J) \\ -8(J-1)(J+1)^2(J+3)\end{array}\right]^2$
${}^OP_{12}(J)$	$\frac{(J-1)(J+1)}{2JC_1'(J-1)C_2''(J)}\left[\begin{array}{c} J^2u_1'^+(J-1) - (J-2)(J+2)u_1'^-(J-1) \\ -2J(J-2)(Y''-2)\end{array}\right]^2$
${}^PQ_{12}(J)$	$\frac{2(2J+1)}{J(J+1)C_1'(J)C_2''(J)}\left[(J-1)(J+2)u_1'^-(J) + (J-1)(J+1)(Y''-2)\right]^2$
${}^QR_{12}(J)$	$\frac{J(J+2)}{2(J+1)C_1'(J+1)C_2''(J)}\left[\begin{array}{c} (J+1)^2u_1'^+(J+1) - (J-1)(J+3)u_1'^-(J+1) \\ -2J(J+2)(Y''-2)\end{array}\right]^2$
$P_2\ (J)$	$\frac{4(J-1)(J+1)}{JC_2'(J-1)C_2''(J)}\left[\frac{1}{2}(Y'-2)(Y''-2) + (J-2)(J+2) + J^2\right]^2$
$Q_2\ (J)$	$\frac{4(2J+1)}{J(J+1)C_2'(J)C_2''(J)}\left[\frac{1}{2}(Y'-2)(Y''-2) + 2(J-1)(J+2)\right]^2$
$R_2\ (J)$	$\frac{4J(J+2)}{(J+1)C_2'(J+1)C_2''(J)}\left[\frac{1}{2}(Y'-2)(Y''-2) + (J-1)(J+3) + (J+1)^2\right]^2$
${}^QP_{32}(J)$	$\frac{(J-1)(J+1)}{2JC_3'(J-1)C_2''(J)}\left[\begin{array}{c} J^2u_3'^-(J-1) \\ -\ (J-2)(J+2)u_3'^+(J-1) + 2(J-1)(J+1)(Y''-2)\end{array}\right]^2$
${}^RQ_{32}(J)$	$\frac{2(2J+1)}{J(J+1)C_3'(J)C_2''(J)}\left[(J-1)(J+2)u_3'^+(J) - J(J+2)(Y''-2)\right]^2$
${}^SR_{32}(J)$	$\frac{J(J+2)}{2(J+1)C_3'(J+1)C_2''(J)}\left[\begin{array}{c} (J+1)^2u_3'^-(J+1) - (J-1)(J+3)u_3'^+(J+1) \\ +2(J+1)(J+3)(Y''-2)\end{array}\right]^2$
${}^NP_{13}(J)$	$\frac{(J-1)(J+1)}{16JC_1'(J-1)C_3''(J)}\left[\begin{array}{c} J^2u_1'^+(J-1)u_3''^-(J) \\ +(J-2)(J+2)u_1'^-(J-1)u_3''^+(J) - 8(J-2)J^2(J+2)\end{array}\right]^2$
${}^OQ_{13}(J)$	$\frac{2J+1}{4J(J+1)C_1'(J)C_3''(J)}\left[(J-1)(J+2)u_1'^-(J)u_3''^+(J) - 4J(J-1)(J+1)(J+2)\right]^2$
${}^PR_{13}(J)$	$\frac{J(J+2)}{16(J+1)C_1'(J+1)C_3''(J)}\left[\begin{array}{c} (J+1)^2u_1'^+(J+1)u_3''^-(J) \\ +(J-1)(J+3)u_1'^-(J+1)u_3''^+(J) - 8J^2(J+2)^2\end{array}\right]^2$
${}^OP_{23}(J)$	$\frac{(J-1)(J+1)}{2JC_2'(J-1)C_3''(J)}\left[J^2u_3''^-(J) - (J-2)(J+2)u_3''^+(J) + 2J(J+2)(Y'-2)\right]^2$
${}^PQ_{23}(J)$	$\frac{2(2J+1)}{J(J+1)C_2'(J)C_3''(J)}\left[(J-1)(J+2)u_3''^+(J) - 2J(J+2)(Y'+2)\right]^2$

$$
\begin{array}{ll}
{}^{Q}R_{23}(J) & \frac{J(J+2)}{2(J+1)C_2'(J+1)C_3''(J)}\left[\begin{array}{c}(J+1)^2u_3''^{-}(J)-(J-1)(J+3)u_3''^{+}(J)\\ +2J(J+2)(Y'-2)\end{array}\right]^2 \\
P_3\ (J) & \frac{(J-1)(J+1)}{16JC_3'(J-1)C_3''(J)}\left[\begin{array}{c}J^2u_3'^{-}(J-1)u_3''^{-}(J)\\ +\quad (J-2)(J+2)u_3'^{+}(J-1)u_3''^{+}(J)\\ +8J(J-1)(J+1)(J+2)\end{array}\right]^2 \\
Q_3\ (J) & \frac{2J+1}{4J(J+1)C_3'(J)C_3''(J)}\left[(J-1)(J+2)u_3'^{+}(J)u_3''^{+}(J)48J^2(J+2)^2\right]^2 \\
R_3\ (J) & \frac{J(J+2)}{16(J+1)C_3'(J+1)C_3''(J)}\left[\begin{array}{c}(J+1)^2u_3'^{-}(J+1)u_3''^{+}(J)\\ +\quad (J-1)(J+3)u_3'^{+}(J+1)u_3''^{+}(J)\\ +8J(J+1)(J+2)(J+3)\end{array}\right]^2
\end{array}
$$

$$
\begin{array}{c}
u_1^{\pm}(J)=\sqrt{Y(Y-4)+4J^2}\pm(Y-2)\qquad u'\leftrightarrow Y'\ -\ u''\leftrightarrow Y'' \\
u_3^{\pm}(J)=\sqrt{Y(Y-4)+4\left(J+1\right)^2}\pm(Y-2) \\
C_1(J)=Y(Y-4)(J+2)(J-1)+2J(2J+1)(J+1)(J-1) \\
C_2(J)=Y(Y-4)+4J(J+1)\qquad C'\leftrightarrow u'\ -\ C''\leftrightarrow u'' \\
C_3(J)=Y(Y-4)J(J+1)+2J(2J+1)(J+2)(J+1)
\end{array}
$$

Table B.9: Hönl-London factors for ${}^3\Pi-{}^3\,\Pi$ transitions

Appendix C

Potential Energies and Wavefunctions Reconstruction With the RKR_SCH Routine

This section describes the associated `RKR_SCH.m` routines that are either used to yield values for the transition Einstein coefficients $A_{v'v''}$, or to achieve an accurate list of the overall rovibrational levels for a specific electronic state, including quasi-bound states. This suite of routines is located in the `RKR_SCH*` directory

C.1 Theory

As discussed in Chapter 2, for a given electronic state e, and neglecting fine-structure, the energy levels of a diatomic molecule are usually expressed in the form of a Dunham expansion (See Eq. 2.11). However, as already discussed in Chapter 4, the adequacy of the Dunham expansion is directly associated with the validity of the spectroscopic constants which are obtained by fitting a given set of measured rovibrational levels with the expansion (2.11). Rigorously, such an expansion can only be accurate at describing the initial set of rovibrational levels over which the spectroscopic constants have been interpolated, but unfortunately some compilations of spectroscopic data do not clearly include the range of the rotational and vibrational quantum numbers over which the expansion is strictly valid. This means that in most cases we do not know whether we are using a set of Dunham coefficients within its validity range or beyond it. In this latter case, and since the Dunham expansion is essentially a polynomial expansion, the predicted energies of higher-lying levels may increasingly diverge from the exact energies, due to the typical instability of extrapolations by polynomials. The expansion becomes hence increasingly inaccurate as the quantum numbers v and J become large.

One may instead consider reconstructing the electronic state radial poten-

tial curve, which is achieved through the Rydberg–Klein–Rees (RKR) method [67, 68, 69, 70], a widely used first-order semiclassical inversion procedure for reconstructing the potential energy curve of a diatomic molecule electronic state, provided that the spectroscopic constants of this state are known.

The RKR method starts from the first-order JWKB quantization

$$(v+\frac{1}{2}) \;=\; \frac{1}{\pi}\sqrt{\frac{2\mu}{\hbar^2}}\int_{r_1}^{r_2}[E-V(r)]^{1/2}dr\;, \tag{C.1}$$

in which $V(r)$ and E denote the potential energy function and the total energy, respectively, μ is the reduced mass, and r_1 and r_2 are the inner and outer classical turning points. The derivation of the RKR formalism assumes the existence of a well-behaved single minimum potential around the equilibrium distance and that the vibrational and rotational energies are smooth functions of v. Two expressions can be then obtained for the case of non-rotating and rotating molecules

$$r_2(v)-r_1(v) \;=\; 2\sqrt{\frac{\hbar^2}{2\mu}}\int_{v_{min}}^{v}[E(v)-E(v')]^{-1/2}\,dv' \;=\; 2f \tag{C.2}$$

$$\frac{1}{r_2(v)}-\frac{1}{r_1(v)} \;=\; 2\sqrt{\frac{2\mu}{\hbar^2}}\int_{v_{min}}^{v}B_{v'}\,[E(v)-E(v')]^{-1/2}\,dv' \;=\; 2g\;, \tag{C.3}$$

which are usually known as the "vibrational" and the "rotational" RKR equations. Here, $v_{min} = v(E{=}0)$ and B_v in equation (C.3) is the rotational constant defined in $E(v,J) = B_v\,J(J+1)$. Rearrangement of equations (C.2, C.3) gives the final expressions

$$r_1(v) \;=\; \sqrt{f^2+f/g}\;-\;f \tag{C.4}$$

$$r_2(v) \;=\; \sqrt{f^2+f/g}\;+\;f\;. \tag{C.5}$$

It is worth noting at this point that although the semiclassical quantization condition maps integer values of v, within the semiclassical RKR approach v may be treated as a continuous variable. This allows obtaining a much larger number of points than those obtained using integer values for a precise determination of the energy potential curve. Finally, the integrals f and g are not defined in their upper limit, so that a Gauss quadrature method has to be used in order to determine these functions near the upper limit [1].

Once the near-equilibrium part of the potential curve has been obtained, it is necessary to extrapolate this potential curve up to the dissociation limit. In the developed routine, we choose to extrapolate the RKR potential using a repulsive potential for shorter internuclear distances, and by a Hulburt and Hirschfelder [71] potential for longer internuclear distances. This latter potential consists in a two-parameter correction term to the usual Morse potential. The expressions for such potential take the form

$$V_{rep}(r) = A/r^p \tag{C.6}$$

$$V_{HH}(r) = D_e \left[\left(1 - e^{-\alpha(r-r_e)}\right)^2 + \beta\alpha^3 (r-r_e)^3 e^{-2\alpha(r-r_e)} \left(1 + \alpha\gamma(r-r_e)\right) \right] \tag{C.7}$$

where r_e is the equilibrium internuclear distance, D_e is the dissociation energy, and A, p, α, β and γ are fitting parameters that need to be adjusted in order to insure continuity with the RKR potential curve.

Upon calculation of the overall potential curve, the vibrational level energies can be determined by solving the radial Schrödinger equation for this same potential curve. This calculation is carried out for the case of a rotationless state using the method proposed by Balint–Kurti [72], with the typographical correction indicated in [1]. For the lower part of the potential curve obtained utilizing the RKR method, one simply obtains once again the same level energies (barring any numerical precision errors) that have been used as an input (from spectroscopic data) for building this same RKR potential curve. But more importantly, one also obtains the energies of the higher-lying levels that fall on the extrapolated part of the potential curve. Such extrapolated values are more credible than the ones obtained from the extrapolation of a Dunham expansion 2.11, as they rely on a smoothly extrapolated potential curve, instead of an inherently unstable polynomial expression.

C.1.1 Recalculating potentials for an arbitrary rotational excitation

The potential for an arbitrary rotational number J can be obtained using the relationship

$$V_J(r) = V_{J=0}(r) + \frac{\hbar^2 J(J+1)}{2\mu r^2}, \tag{C.8}$$

where μ is the reduced mass of the molecule.

The energies for the corresponding rovibrational levels can then be obtained by solving the radial Schrödinger equation. The maximum rotational quantum number is then reached when the molecular potential no longer allows a local minima, becoming entirely repulsive.

For the application of Eq. C.8, we consider the accurate rotationless potential proposed by LeRoy [73]. The last potential curve allowing for discrete states occurs for J=275. The potential curves for different rotational levels are reported in Fig. C.1

The obtained solutions account for the existence of bounded levels above the dissociation energy. Those levels are called quasi-bound levels and contribute weakly to the overall electronic state partition function. These levels have finite lifetimes, as they can spontaneously dissociate through quantum-tunneling. A recap of the method that can be used for determining these states lifetimes,

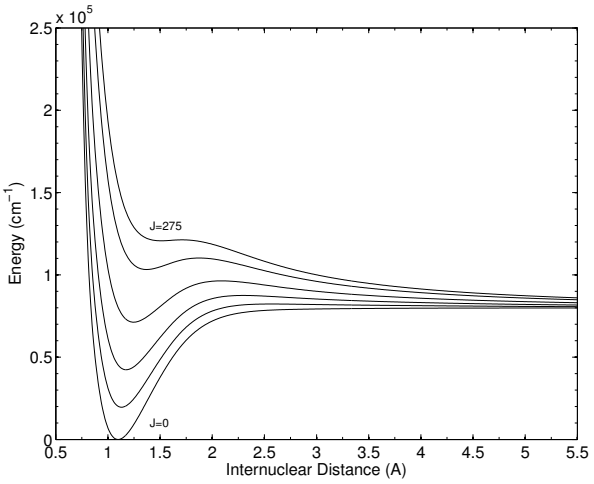

Figure C.1: N_2(X) Potential curves for J=0, 100, 150, 200, 250, and 275, from bottom to top

and a discussion on how these levels have to be accounted thermodynamically is presented in Ref. [74].

C.1.2 Expressions for Radiative transition probabilities

Solving the radial Schrödinger equation over reconstructed potential curves yields a set of predicted quantum vibrational levels and their associated energies and wavefunctions. The calculated values for the vibrational levels energies and wavefunctions may be utilized for calculating complete sets of radiative transition probabilities, the most paramount being the vibrational Einstein coefficients $A_{v'v''}$ who may then be supplied to the spectral database of the SPARTAN code. An example of recalculated levels and wavefunctions, for the CN Violet transition, is presented in Fig. C.2.

The expressions for several radiative quantities that are calculated by the `RKR_SCH` routine with the input of recalculated, rotationless potentials for the upper and lower states, and a supplied electronic transition moment $R_e(r)$ are

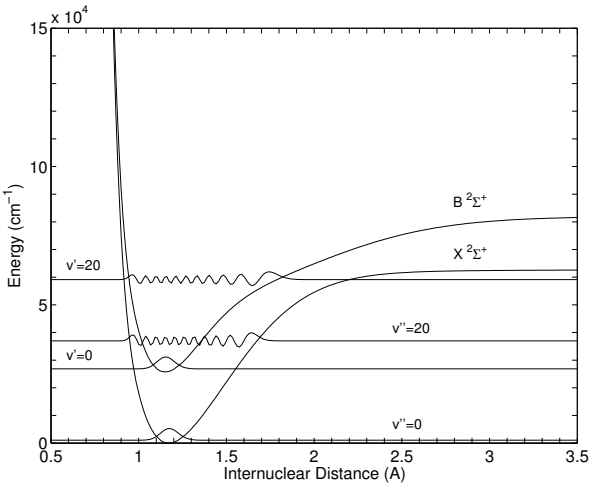

Figure C.2: Recalculated Wavefunctions for the $v = 0, 20$ levels of the upper and lower states of the CN Violet system

presented in Eqs. C.9.

$$q_{v'v''} = \left(\int \psi_{v'}(r)\psi_{v''}(r)dr \right)^2 \tag{C.9a}$$

$$r_{v'v''} = \frac{\int \psi_{v'}(r)\ r\ \psi_{v''}(r)dr}{\int \psi_{v'}(r)\psi_{v''}(r)dr} \tag{C.9b}$$

$$R_e^{v'v''} = \int \psi_{v'}(r)R_e(r)\psi_{v''}(r)dr \tag{C.9c}$$

$$A_{v'v''} = \frac{64\pi^4\overline{\nu}^3(2-\delta_{0,\Lambda'+\Lambda''})}{3hc^3(2-\delta_{0,\Lambda'})}\left(R_e^{v'v''}\right)^2 \tag{C.9d}$$

$$= 2.026\times10^{-6}\overline{\nu}^3_{v'v''}\frac{2-\delta_{0,\Lambda'+\Lambda''}}{2-\delta_{0,\Lambda'}}\left(R_e^{v'v''}\right)^2$$

$$f^{abs}_{v'v''} = \frac{8\pi^2 m_e\overline{\nu}(2-\delta_{0,\Lambda'+\Lambda''})}{3he^2(2-\delta_{0,\Lambda'})}\left(R_e^{v'v''}\right)^2 \tag{C.9e}$$

$$= 3.0376\times10^{-6}\overline{\nu}_{v'v''}\frac{2-\delta_{0,\Lambda'+\Lambda''}}{2-\delta_{0,\Lambda'}}\left(R_e^{v'v''}\right)^2$$

$$f^{emi}_{v'v''} = \frac{2-\delta_{0,\Lambda''}}{2-\delta_{0,\Lambda'}}f^{abs}_{v'v''} \tag{C.9f}$$

C.1.3 Numerical Routines Description

The `RKR_SCH` suite consists of three similar routines:

- `RKR_SCH` routine for the calculation of radiative transition probabilities.
- `RKR_SCH_PC` routine for the calculation of potential curves, vibrational energy levels and wavefunctions.

- `RKR_SCH_PC_ROT` routine for the calculation of rovibrational energy levels and wavefunctions, including quasi-bound states.

The usage for each routine is:

```
>> [qvv,rvv,Revv_2,Avv,fvv]=RKR_SCH('FILE.txt')

>> [r_RKR,V_RKR,G_v,Te,ri,A,E]=RKR_SCH_PC('FILE.txt',r,V)
```

with r (in Å) and V (in cm^{-1}) optional parameters (use `[]` otherwise) if you wish to supply a potential function and just solve the radial Schrödinger equation.

```
>> RKR_SCH_PC_ROT('Level spectrocopic constants',0/1,...
                  'Supplied potential',v_max,J_ini,J_step,J_final)
```

Instead of returning values to the invoking function, the `RKR_SCH_PC_ROT` saves the variables `r_i` (rotationless potential abcissae in Bohrs) radius; `Ve_ri_J` (rotationless potential energy in Hartree); `V_J` (Matrix with the energy in Hartrees of the level pairs $E(v, J)$); `v_minmax` (the minimum and maximum vibrational levels for each rotational level); to the `MATLAB` file `v_J_levels`

If you want to supply your own rotationless potential, create a `MATLAB` file with the variables r (in Å) and V (in cm^{-1}), set the variable `0/1` to `0`, and declare the file name in `'Supplied potential'`. Otherwise set the variable `0/1` to `1`, and set the input variable to empty (`''`).

C.1.3.1 Input files structure

The structure of the `RKR_SCH` routines will not be described in detail here. Instead the user may consult the `EXAMPLES` folder where the `NO-XX.txt` and `N2-X.txt` files provide examples of input files for respectively the routine `RKR_SCH`, and the routines `RKR_SCH_PC`,`RKR_SCH_PC_ROT`. The `MATLAB` file `N2X-DPF.mat` contains a high-resolution potential (for the ground electronic state of N_2) which may be supplied to the `RKR_SCH_PC_ROT` function directly (referencing the filename at function input), and indirectly supplied to the `RKR_SCH_PC` function (passing the r and V variables).

Note: If for some reason the recalculated potential curves do not seem accurate, try lowering the v_{max} parameter, describing the boundary beyond where the supplied Dunham matrix is no longer valid.

The files `CParam.txt` and `CParam_J*.txt` define several accuracy parameters for the RKR calculation, as well as the fixed spectral grid where the radial Schrödinger equation is solved. The currently input values should in principle suffice for all practical calculations, and they should be modified at the user's own risk.

Appendix D

Other Auxiliary Routines

This section shortly describes several auxiliary functions which are supplied with the SPARTAN code bundle. They are located in the code root directory. These functions should be used after running the main SPARTAN code. They interact with the the workspace variable `ResultTotal` which the code SPARTAN yields as an output.

`Avg_IA.m`:

Averages the absorption coefficients calculated by the SPARTAN Code, and yields band mean absorption coefficients, and Planck mean absorption coefficients for a custom set of spectral intervals.

Intervals (in A) are defined in the first line of the Function. The variables `avg` and variables `avg_Pl` respectively the band mean absorption and Planck mean absorption coefficients, are returned to the workspace.

`Compare.m`:

Compares the synthetic SPARTAN spectrum against measured spectra.

The necessary steps are:

1) Replacing the `Measured.txt` file in the OUTPUTS folder by the experimental file (in A wavelength units); 2) Calculating the simulated spectra; 3) From the command line running: `Compare(ResultTotal,shift,noise,normalize)`, where `shift` is the experimental spectrum shift (in Å), `noise` is the experimental spectrum noise (arbitrary units), and `normalise` is **1** if the two spectra are to be normalized, or **0** if they are to be calculated in absolute intensity units ($W/m^3/cm^{-1}$–sr).

Usage is:
`Compare(ResultTotal,3.7,0,1)`

`AFunction.m`:

Convolutes Spectra with a Gaussian apparatus function.

Usage is:
`[lam,I_AF]=AFunction(ResultTotal.nu,ResultTotal.I_E,width);`,

with `width` the width of the apparatus function (in Å)

`Test_DiatomicFiles.m`:

Tests the integrity of diatomic transitions spectral files.

Usage is:
`Test_DiatomicFiles('FILENAME','TRANSITION')`,

with `FILENAME` the name of the datafile for verification, which should be hosted in the DATABASE directory, and `TRANSITION` is the identifier for the multiplet-type of the transition.

Example for invoking the function:
`Test_DiatomicFiles('NO-XX.txt','2P---2P')`

Bibliography

[1] Lino da Silva M., "Simulation des Propriétés Radiatives du Plasma Entourant un Véhicule Traversant une Atmosphère Planétaire à Vitesse Hypersonique: Application à la planète Mars", PhD Thesis (in French), *Université. Orléans*, 2004. available at: http://esther.ist.utl.pt/documents/these_LinodaSilva2004.pdf

[2] Martin W. C., and Wiese W. L., "Atomic Spectroscopy", *NIST*, 1996, available at http://sed.nist.gov/Pubs/AtSpec/total.html

[3] Herzberg G., *"Spectra of Diatomic Molecules"*, 2nd Ed., AD. Van Nostrand Company Inc, 1965.

[4] Zare R. N., Schemeltekopf A. L., Harrop W. J., and Albritton D. L., "A Direct Approach for the Reduction of Diatomic Spectra to Molecular Constants for the Construction of RKR Potentials".*Journal of Molecular Spectroscopy*, Vol. 46, 1973, pp. 37–66.

[5] Hill E., and Van Vleck J. H., "On the Quantum Mechanics of the Rotational distortion of Multiplets in Molecular Spectra", *Phis. Rev.*, Vol. 32, No. 2, 1928, pp. 250–272.

[6] Nicolet M., Cieslik S., and Kennes R., "Aeronomic Problems of Molecular Oxygen Photodissociation - V. Predissociation in the Schumann–Runge Bands of Oxygen". *Planet Space Sci*, Vol. 37, 1989 pp. 427–458.

[7] Miller S. L., and Townes C. H., "The Microwave Absorption Spectrum of $(O^{16})_2$ and $O^{16}O^{17}$". *Phys Rev*, Vol. 90, 1953, pp. 537–543.

[8] Laux C. O. "Optical Diagnostics and Radiative Emission of Air Plasmas". Ph.D. Thesis, *Stanford University*, 1993.

[9] Budò A., "Über die Triplett-Bandentermformel für den Allge Meinen Intermediären Fall und Anwendung Derselben auf die $B^3\Pi-$, $^3\Pi-$ Terme des N_2-Moleküls". *Z. Physik*, Vol. 96, 1935, pp. 219–229.

[10] Brown J. M., Kaise M., Kerr C. M. L., and Milton D. J., "A Determination of Fundamental Zeeman Parameters for the OH Radical", *Mol. Phys.*, Vol. 36, No. 2, 1978, pp. 553–582.

[11] Brown J. M., Colbourn E. A., Watson J. K. G., and Wayne F. D., "An Effective Hamiltonian for Diatomic Molecules", *J. Mol. Spectrosc.*, Vol. 74, 1979, pp. 294–318.

[12] Lefebvre–Brion H., and Field R. W., *"Perturbations in the Spectra of Diatomic Molecules"*, Academic Press Inc – London, 1986.

[13] Taine J., "A Line-by-Line Calculation of Low-Resolution Radiative Properties of CO_2–CO Transparent Nonisothermal Gases Mixtures up to 3000 K". *JQSRT*, Vol. 30, No. 4, 1983, pp. 371–379.

[14] Gamache R. R., Rothman L. S., "Extension of the HITRAN Database to Non-LTE Applications", *JQSRT*, Vol. 48, 1992, No. 5/6, pp. 519–525.

[15] Scutaru D., "Etudes Théorique et Expérimentale de l'Absorption Infrarouge par CO_2 à Haute Température. Application à des Modèles de Rayonnement des Gaz", Ph.D. Thesis (in French), Laboratoire d'Energétique Moléculaire et Macroscopique, Combustion (E.M2.C), *Ecole Centrale de Paris*, 1994.

[16] Rothman L. S., Hawkins R. L., Watson R. B. , and Gamache R. R., "Energy Levels, Intensities, and Linewidths of Atmospheric Carbon Dioxide Bands", *JQSRT*, Vol. 48, No. 5/6, 1992, pp. 537–566.

[17] Wiese W. L., Fuhr J. R., and Deters T. M., "Atomic Transition Probabilities of Carbon, Nitrogen and Oxygen", *Journal of Physical and Chemical Reference Data*, Monograph No. 7, 1996.

[18] Jefferies J. T. *"Spectral Line Formation"*, Blaisdell Company, 1st Ed., 1968.

[19] Griem H .R., ''*Plasma Spectroscopy"*, McGraw-Hill, 1964

[20] Whiting E. E., "An Empirical Approximation to the Voigt Profile", *JQSRT*, Vol. 8, No. 6, 1968 pp. 1379–1384.

[21] Olivero J. J. and Longbothum R. L., "Empirical Fits to the Voigt Line Width: A Brief Review". *JQSRT*, Vol. 17, No. 2, 1977 pp. 233–236.

[22] Stallcop J. R., and Billman K. W., "Analytical Formulae for the Inverse Bremsstralung Absorption Coefficient", *Plasma Physics*, Vol. 16, 1974, pp. 1187–1189.

[23] Karzas W. J., and Latter R., "Electron Radiative Transitions in a Coulomb Field", *Astrophysical Journal Supplement*, Vol. 6, 1961, pp. 167–212.

[24] Hummer D. G., "A Fast and Accurate Method for Evaluating the Nonrelativistic Free-Free Gaunt Factor for Hydrogenic Ions", *The Astrophysical Journal*, Vol. 327, 1988, pp. 477–484.

[25] Menzel D. H., and Pekeris C. L., "Absorption Coefficients and Hydrogen Line Intensities", *Monthly Notices of the Royal Astronomical Society*, Vol. 96, No. 1, 1935, pp. 77–111.

[26] Kramers H. A., "On the Teory of X-Ray Absorption and of the Continuous X-Ray Spectrum", *Philosophical Magazine*, Vol. 46, 1923, pp. 836–871.

[27] Mjolsness R. C., and Ruppel H. M., "Contribution of Inverse Neutral Bremsstrahlung to the Absorption Coefficient of Heated Air", *JQSRT*, Vol. 7, 1967, pp. 423–427.

[28] Chauveau S., "Constitution de Bases de Données Spectroscopiques Relatives à un Plasma d'Air: Application au Calcul de Transferts Radiatifs", Ph.D. Thesis (in French), Laboratoire d'Energétique Moléculaire et Macroscopique, Combustion (E.M2.C), *Ecole Centrale de Paris*, 2001.

[29] Milne E. A., "Radiative Equilibrium in the Outer Layers of a Star", *Monthly Notices of the Royal Astronomical Society*, Vol. 81, No. 5, 1921, pp. 361–375.

[30] Milne E. A., "Spectroscopy, Astronomical, Radiative Equilibrium and Spectral Distribution", *Monthly Notices of the Royal Astronomical Society*, Vol. 81, No. 5, 1921, pp. 375–388.

[31] Vranckx S., Loreau J., Desouter–Lecomte M., and Vaeck N., "Determination of Photodissociation and Radiative Association Cross Sections From the Same Time-Dependent Calculation", *ArXiv e-prints*, eprint 1301.5547, 2013, available at http://adsabs.harvard.edu/abs/2013arXiv1301.5547V.

[32] Zhu X., "An Inproved Voigt Line Approximation for the Calculations of Equivalent Width and Transmission',' *JQSRT*, Vol. 39, No. 6, 1988, pp. 421–427.

[33] Smith A. J., Gogel T., and Vandevelde P., *Plasma Radiation Database PARADE*, Final Report, ESTEC Contract 11148/94/NL/FG, TR28/96, Apr. 1996.

[34] Lino da Silva M., Guerra V., and Loureiro J., "Vibrational Distributions in N_2 With an Improved Calculation of Energy Levels Using the RKR Method", *Chem. Phys.*, Vol. 348 ,2008, pp. 187–194.

[35] Prasad C. V. V., and Bernath P. F., "Fourier Transform Jet-Emission Spectroscopy of the $A^2\Pi_j - X^2\Sigma^+$ Transition of CN". *Journal of Molecular Spectroscopy*, Vol. 156, 1992, pp. 327–340.

[36] http://physics.nist.gov/PhysRefData/ASD/index.html

[37] http://vizier.u-strasbg.fr/topbase/topbase.html

[38] Cooper J. W., and Martin J. B., "Electron Photodetachment From Ions and Elastic Collision Cross Sections for O, C, Cl, and F", *Physical Review*, Vol. 126, No. 4, 1962, pp. 1482–1488.

[39] Hwang W., and Kim Y.-K., "New Model for Electron-Impact Ionization Cross-Sections of Molecules", *Journal of Chemical Physics*, Vol. 104, No. 8, 1996, pp. 2956–2966.

[40] Romanov G. S., Stankevich Y. A., Stanchits L. K., and Stepanov K. L., "Thermodynamic and Optical Properties of Gases in a Wide Range of Parameters", *Int. J. Heat Mass Transfer*, Vol. 38, No. 3, 1995, pp. 545–556.

[41] Masuoka T., and Nakamura E., "Single-, Double-, and Triple-Photoionization Cross Sections of Carbon Monoxide (CO) and Ionic Fragmentation of CO^+, CO_2^+, and CO_3^+", *Physical Review A*, Vol. 48, No. 6, 1993, pp. 4379–4389.

[42] Fennely J. A., and Torr D. G., "Photoionization and Photoabsorption Cross Sections of O, N_2, O_2, and N for Aeronomic Calculations", *Atomic Data and Nuclear Data Tables*, Vol. 51, 1992, pp. 321–363.

[43] Masuoka T., and Nakamura E., "Single- and Double-Photoionization Cross Sections of Nitric Oxide (NO) and Ionic Fragmentation of CO^+ and CO_2^+", *Physical Review A*, Vol. 48, No. 3, 1993, pp. 1955–1963.

[44] Huber K. P. and Herzberg G. "Molecular Spectra and Molecular Structure – IV. Constants of Diatomic Molecules", *Van Nostrand Reinhold Company*, 1979.

[45] Abgrall H., Roueff E., Launay F., Roncin J.–Y., and Subtil J.–L., "The Lyman and Werner Bands of Molecular Hydrogen", *J. Mol. Spectr.*, Vol. 157, 1993, 512–523.

[46] Fantz U., and Wünderlich D., "Franck–Condon Factors, Transition Probabilities and Radiative Lifetimes for Hydrogen Molecules and Their Isotopomeres", Tech. Rep. INDC(NDS)-457, *IAEA*, Vienna, May 2004.

[47] Douay M., Nietmann R., and Bernath P. F., "New Observations of the $A^1\Pi_u$–$X^1\Sigma_g^+$ Transition (Phillips System) of C_2", *Journal of Molecular Spectroscopy*, Vol. 131, 1988, pp. 250–260.

[48] Phillips J. G., "Perturbations in the Swan System of the C_2 Molecule", *Journal of Molecular Spectroscopy*, Vol. 28, 1968, pp. 233–242.

[49] Piar B., "Production de Molécules Excitées Vibrationellement et Electroniquement par Pompage Laser. Analyse des Etats Formés", Thèse de Doctorat, *Ecole Centrale de Paris*, Sept. 1993.

[50] George T., Urban W., and Le Floch A., "Improved Mass-Independent Dunham Parameters for the Ground State of CO and Calibration Frequencies for the Fundamental Band", *Journal of Molecular Spectroscopy*, Vol. 165, 1994, pp. 500–505.

[51] Prasad C. V. V., Bhale L., and Paddy Reddy S., "Rotational Analysis of the $B^1\Sigma^+ - A^1\Pi$ System of $^{13}C^{18}O^*$", *Abstracts of OSU International Symposium on Molecular Spectroscopy 1980–1989*, 1983.

[52] Prasad C. V. V., Bhale L., and Paddy Reddy S., "The Third Positive ($b^3\Sigma^+$–$a^3\Pi_r$) System of CO: Observation of the v=2 Level of $b^3\Sigma^+$", *Journal of Molecular Spectroscopy*, Vol. 121, 1987, pp. 261–269.

[53] Krupenie P. H., "The Band Spectrum of Carbon Monoxide", *Tech. Rep. NSRDS–NBS 5*, National Bureau of Standards, July 1966.

[54] Simmons J. D., Bass A. M., Tilford S. G., "The Fourth Positive System of Carbon Monoxide Observed in Absorption at High Resolution in the Vacuum Ultraviolet Region", *The Astrophysical Journal*, Vol. 155, 1969, pp. 345–358.

[55] Kepa R., Rytel M., "The Ångstrom ($B^1\Sigma^+$–$A^1\Pi$) System of the CO Molecule: New Observations and Analyses", *J. Phys. B: At. Mol. Opt. Phys.*, Vol. 26, 1993, pp. 3355–3362.

[56] Park C., "Nonequilibrium Hypersonic Aerothermodynamics", *John Wiley & Sons, Inc.*, 1989.

[57] Lofthus A, and Krupenie P. H., "The Spectrum of Molecular Nitrogen", *J. Phys. Chem. Ref. Data*, Vol. 6, No. 1, 1977, pp. 113–307.

[58] Owono Owono L. C., Jaidane N., Kwato Njock M. G., and Ben Lakhdar Z., "Theoretical Investigation of Excited and Rydberg States of Imidogen Radical NH: Potential Energy Curves, Spectroscopic Constants, and Dipole Moment Functions", *J. Chem. Phys.*, Vol. 126, 2007, pp. 244302-1–244302-13.

[59] Luque J., and Crosley D. R., "Transition probabilities in the $A^2\Sigma^+ - X^2\Pi_i$ Electronic System of OH", *J. chem. Phys.*, Vol. 109, No. 2, 1998, pp. 439–448.

[60] Hwang E. S., Lipson J. B., Field R. W., and Dodd J. A., "Detection of OH(X,v", J") via the $B^2\Sigma^+ - X2\Pi$ Transition and Properties of the $B^2\Sigma^+$ State", *J. Phys. Chem. A*, Vol. 105, 2001, pp. 6030–6037.

[61] Schadee A., "Theory of First Rotational Lines in Transitions of Diatomic Molecules", *Astron. & Astrophys.*, Vol. 41, 1975, pp. 203–121.

[62] Kovacs I., "Rotational Structure in the Spectra of Diatomic Molecules", *Adam Hilger Ltd.*, 1969.

[63] Schadee A., "The Formation of Molecular Lines in the Solar Spectrum", *Bull Astron Inst Neth*, Vol. 17, No. 5, 1964, pp. 311–357.

[64] Arnold J. O., Whiting E. E., and Lyle G. C., "Line by Line Calculation of Spectra From Diatomic Molecules and Atoms Assuming a Voigt Line Profile", *JQSRT*, Vol. 9, 1969, pp. 775–798.

[65] Tatum J. B., "Höln-London Factors for $^3\Sigma^\pm - ^3\Sigma^\pm$ Transitions", *Canadian Journal of Physics*, Vol. 44, 1966, pp. 2944–2946.

[66] Budò A., "Intensitätsformeln für die Triplettbanden", *Mitteilung aus dem Physikalischen Institut der Königl.-Ungarischen Universität für Technische und Wirtschaftwissenschaften*, 1937, pp. 579–587.

[67] Rydberg R., "Graphische Darstellung Einiger Bbandenspektroskopischer Ergebnisse", *Z. Physik*, Vol. 73, 1931, pp. 376–385.

[68] Klein O., "Zur Berechnung von Potentialkurven für Zweiatomige Moleküle Mit Hilfe Von Spektraltermen", *Z. Physik*, Vol. 76, 1932, pp. 226–235.

[69] Rydberg R., " Über Einige Potentialkurven des Quecksilberhydrids", *Z. Physik*, Vol. 80, 1933, pp. 514–524.

[70] Rees A. L. G., "The Calculation of the Potential Energy Curves From Band–Spectroscopy Data", *Proc. Phys. Soc. (London)*, Vol. 59, 1947, pp. 998–1008.

[71] Hulburt H. M., and Hirschfelder J. O., "Potential Energy Functions for Diatomic Molecules", *J. Chem. Phys.*, Vol. 9, 1941, pp. 61–69.

[72] Balint-Kurti G. G., Dixon R. N., and Marston C. C., "Grid Methods for Solving the Schrödinger Equation and Time Dependent Quantum Dynamics of Molecular Photofragmentation and Reactive Scattering Processes", *Int. Reviews in Phys. Chem.*, Vol. 11, No. 2, 1992, pp. 317–344.

[73] Le Roy R. J., Huang Y., and Jary C, "An Accurate Analytic Potential Function for Ground-State N_2 From a Direct-Potential-Fit Analysis of Spectroscopic Data", *J. Chem. Phys.* Vol. 125, No. 16, 2006, pp. 4310–4322.

[74] Lino da Silva M., Loureiro J., and Guerra V., "Rotational Nonequilibrium in State-Resolved Models for Shock-Heated Flows", *Chem. Phys.*, Vol. 398, 2012, pp. 96–103.

Appendix E

Code Versions Log

Table E.1 lists the previous versions of the SPARTAN code.

Version	Date	Comments
		SPARTAN Code
1.0	02/2003	Prototype version #1
1.1	11/2004	Prototype version #2
1.5	01/2005	Original Version
2.0	01/2006	Major update, reworking of the code directories and functions structure
2.0.1	03/2007	Added functions `AFunction.m` and `Compare.m`, updated functions `Atomic3.m` `Bremstr.m`
2.1	11/2007	Major update, added coupling capability for large-scale radiative transfer calculations. Species added to the spectral database
2.2	12/2008	Updated database for CO_2 Infrared transitions
2.2.1	05/2010	Updated `Spectre.m` function
2.2.2	05/2010	Updated GUI
2.3	12/2011	Corrected several bugs, added species to the spectral database
2.5	05/2013	Generalized rewrite of the code, added species and revamped the spectral database
		RKR_SCH routine
1.0	12/2003	Prototype version #1
1.1	01/2005	Final version, textfile input mode added
1.2	12/2011	Some updates, bug fixes, improved routines, new versions tailored for the calculation of rovibrational states, including quasi-bound states

Table E.1: SPARTAN code Version list

E.1 Next Version updates

Version 2.6 of the SPARTAN code is expected to be released partly or overall with the following updates:

- Explicit treatment of satellite lines in multiplet transitions
- Inclusion of N_2 Rydberg transitions in the spectral database.
- Inclusion of an optional routine which discards spurious levels with energies above the electronic state dissociation limit D_e.
- Adding the option to plot the Planck Blackbody emission coefficient.
- Inclusion of a semi-functional version of the Ray-Tracing Radiative Transfer routine developed for the simulation of radiative transfer in atmospheric entry flows.

For future versions, the following updates will be undertaken, yet are not scheduled to date:

- Implementation of a QSS model for nonequilibrium excitation modeling in air plasmas.

E.2 Code Regressions

- Compared to version 2.3, version 2.5 does not simulate perturbations for the $N2^+$ First Negative System with as much accuracy.

E.3 Code Run Times

The run times for the different radiative systems of the SPARTAN code database are reported in Table E.2. Calculations have been run on an Intel Core i7 620M processor with 6GB of memory. This is valid for the database include with the version 2.5 of the code. Calculations have been carried out with either the original v_{max}, or limiting v_{max} to 11. The resulting radiative grid sizes are also reported for both cases. For multiplet transitions, fine-structure has been accounted for.

As a rule of thumb, if calculation times are deemed too long for a specific system, one may first limit v_{max} to 11, and/or treat multiplet transitions as singlets. In the first case, neglecting the higher vibrational states should not lead to significant differences, except at very high temperatures, where these higher-lying levels may be enough populated that they cannot be discarded. In the second case, the results should be identical for optically thin gases and plasmas at low resolution. This should not be tried for reproducing high-resolution experimental spectra, or when simulating gases where absorption is important (the splitting of a line in multiplets will lead to different absorption values). It is reminded that one may also chose to relax the general parameters of the Lineshape calculation routine, for potentially similar improvements in the calculation times.

Radiative System	v_{max}		Calc. Time (s)		Grid Size (10^6 points)	
H_2 Lyman	15	11	85	85	0.32	0.98
H_2 Werner	14	11	205	210	0.46	0.46
C_2 Phillips	21	11	60	196	0.58	0.32
C_2 Mulliken	21	11	17	49	0.20	0.81
C_2 Deslandres–D'Azambuja	21	11	48	157	0.48	0.59
C_2 Fox–Herzberg	21	11	79	80	0.59	0.86
C_2 Ballik–Ramsay	21	11	51	136	0.51	0.33
C_2 Swan	11	11	271	271	1.00	1.00
CN Violet	21	11	38	92	0.37	0.59
CN Red	21	11	315	1175	1.18	2.6
CO 4^+	21	11	130	524	0.66	1.3
CO Angstrom	21	11	27	46	0.11	0.14
CO 3^+	21	11	22	40	0.29	0.35
CO Asundi	21	11	67	326	0.55	1.2
CO Triplet	21	11	146	490	0.73	1.3
CO^+ Comet–Tail	11	11	120	120	0.83	0.83
N_2 1^+	21	11	660	1660	1.51	2
N_2 2^+	21	11	125	213	0.73	0.9
N_2^+ 1^-	21	11	131	276	0.78	1
NO γ	21	11	304	912	1.08	1.8
NO β	15	11	1113	2093	1.79	2.6
NO δ	21	11	71	193	0.54	0.89
NO ϵ	21	11	144	563	0.76	1.4
NO β'	21	11	77	178	0.56	0.86
NO γ'	21	11	105	340	0.64	1.07
O_2 Schumann–Runge	18	11	1308	1729	1.67	2
CO IR	21	11	17	51	0.26	0.47
NO IR	21	11	52	317	0.43	1.03
CO_2 IR	–	–	84	84	0.31	0.31

Table E.2: Runtimes and grid sizes for the different diatomic transitions of the SPARTAN code database

Appendix F

Selected Published Works

Two selected published works, obtained using the SPARTAN code, are presented in this appendix.

They are respectively:

1. M. Lino da Silva, "An Adaptive Line-by-Line-Statistical model for Fast and Accurate Spectral Simulations in Low-Pressure Plasmas, *JQSRT*, Vol. 108, 2007, p.p. 106–125.

2. M. Lino da Silva, "A Contribution for the Simulation of VUV-IR Radiation Transfer in CO_2–N_2 Entry Flows Using a Line–by–Line Model", *Proc. "4th Int. Workshop on Radiation of High Temperature Gases in Atmospheric Entry"*, Lausanne, Switzerland, 12–15 October 2010 (ESA SP-689, February 2011).

The first work outlines the lineshape model implemented in the SPARTAN code and presents a numerical validation of this model. The second paper presents the application of the SPARTAN code in large-scale radiative transfer computations for an atmospheric entry flow, including a spectral grid convergence study, using the parametric conditions of the `Lineshape.m` routine of the SPARTAN code.

The JQSRT 2007 paper contains a small typo. The correct expression for the C_1 and C_2 expressions in Eq. 2 should read:

$$C_1 = \frac{\left(1 - \frac{\Delta\overline{\nu}_L}{\Delta\overline{\nu}_V}\right)}{\Delta\overline{\nu}_V \left(1.065 + 0.447\frac{\Delta\overline{\nu}_L}{\Delta\overline{\nu}_V} + 0.058\frac{\Delta\overline{\nu}_L^2}{\Delta\overline{\nu}_V^2}\right)}$$

$$C_2 = \frac{\left(\frac{\Delta\overline{\nu}_L}{\Delta\overline{\nu}_V}\right)}{\Delta\overline{\nu}_V \left(1.065 + 0.447\frac{\Delta\overline{\nu}_L}{\Delta\overline{\nu}_V} + 0.058\frac{\Delta\overline{\nu}_L^2}{\Delta\overline{\nu}_V^2}\right)}$$

ELSEVIER

Journal of Quantitative Spectroscopy & Radiative Transfer 108 (2007) 106–125

Journal of Quantitative Spectroscopy & Radiative Transfer

www.elsevier.com/locate/jqsrt

An adaptive line-by-line—statistical model for fast and accurate spectral simulations in low-pressure plasmas

M. Lino da Silva*

Centro de Física dos Plasmas, Instituto Superior Técnico, Av. Rovisco Pais, 1049-001 Lisboa, Portugal

Received 18 October 2006; received in revised form 12 February 2007; accepted 3 March 2007

Abstract

An adaptive grid method is proposed for the simulation of low-pressure plasma radiation. The method relies on two complementary approaches which significantly reduce calculation times and the size of the obtained grids: Weak lines are calculated as a so-called ''pseudo-continuum'', hence reducing the number of calculated lines, and a numerical algorithm has been developed for accurately calculating Voigt lineshapes using a minimum number of points. The method is fully user-parametric, allowing the choice of privileging calculation efficiency, or alternatively privileging the accuracy of the computed spectra. Sample radiative transfer calculations are presented, which show the efficiency of the method, also providing some guidelines on how to define lineshape calculation parameters, depending on the problem to be solved.
© 2007 Elsevier Ltd. All rights reserved.

PACS: 52.25.Os

Keywords: Line-by-line simulations; Numerical methods; Low-pressure plasmas

1. Introduction

Radiative processes encountered in low-pressure plasmas are known to be most accurately simulated using the exact ''line-by-line'' method. However, such approach typically implies the calculation of up to about a million lines. Accounting for the capabilities of modern day computer systems, this precludes the widespread use of this exact method in coupled hydrodynamic–radiative calculations.

This kind of issue may for example arise when simulating the radiative properties of atmospheric entry plasmas. Atmospheric entry radiative processes typically encompass a wide array of more than 50 bound, bound-free and free radiative transitions from more than 20 chemical species ranging from the VUV to the IR region. This means that about 10^4-10^6 discrete lines with the superposition of several continua are to be accounted for [1].

It is therefore evident why approximate methods remain so widespread and popular [2,3], as using the exact line-by-line method remains unaffordable in most applications.

*Fax: +351 21 846 29 91.
E-mail address: mlinodasilva@mail.ist.utl.pt.

0022-4073/$ - see front matter © 2007 Elsevier Ltd. All rights reserved.
doi:10.1016/j.jqsrt.2007.03.005

Nomenclature

$\alpha(\overline{\nu})$	absorption coefficient, m^{-1}
β	adjustable parameter in the calculation of W and FW, –
ℓ	Lorentz line profile, –
ν	frequency, Hz
$\overline{\nu}$	wavenumber, cm^{-1}
$\overline{\nu}_i$	gridpoint wavenumber, cm^{-1}
$\varepsilon_{\overline{\nu}}$	emission coefficient, $W\,m^{-3}-sr\,cm^{-1}$
ζ	adjustable parameter in the calculation of W and FW, –
C	constant, –
contstep	spectral interval for "pseudo-continuum" uniform grid, $contstep = C \times FWHM_{med}$, cm^{-1}
dnu	maximum spectral distance where a strong line is considered to cover a weak line, $dnu = C \times FWHM$, cm^{-1}
FW	boundary between the line near wing and far wing regions, cm^{-1}
$FWHM$	full width at half maximum, cm^{-1}
g	Doppler (Gaussian) line profile, –
i	transformed nonuniform grid, –
I_0	radiative intensity at the exit of the hot slab, $W\,m^{-2}-sr\,cm^{-1}$
i_0	initial uniform grid, –
I_1	radiative intensity at the exit of the cold slab, $W\,m^{-2}-sr\,cm^{-1}$
i_c	line core grid, $i_c = i$, –
i_w	line wings grid, $i_w = 1 - i$, –
max	maximum value of the monotonous grid, –
num_c	number of points distributed inside the half-line core region, –
num_w	number of points distributed inside the half-line wings region, –
par_c	nonuniform grid spacing parameter in the line core region, –
par_{wD}	shape weighting parameter (Doppler) for the calculation of par_w, –
par_{wL}	shape weighting parameter (Lorentz) for the calculation of par_w, –
par_w	nonuniform grid spacing parameter in the line wings region, $par_w = par_{wL} + \Delta\overline{\nu}_D/(\Delta\overline{\nu}_D + \Delta\overline{\nu}_L)\,par_{wD}$, –
*threshold*1	ratio of maximum and cutoff intensity for strong lines, –
*threshold*2	ratio of maximum and cutoff intensity for strong and weak lines, –
v	Voigt line profile, –
W	boundary between the line core and wing region, cm^{-1}

Subscripts

0	hot slab or line center
1	cold slab
c	line core region
G	Doppler
L	Lorentz
med	median value
V	Voigt
w	line wings region

However, regarding the investigation of the spectral properties of low-pressure plasmas, it is difficult to circumvent the use of exact line-by-line methods, owing to the small broadening widths of atomic and molecular spectral lines. Efficient approaches have then to be devised regarding the development of a compact,

yet accurate spectral database of line-by-line transitions [1], but also regarding the convolution of this line database with its adequate lineshapes, followed by the superposition of different continua.

Here, we will present a method to enhance the efficiency of line-by-line calculations, in order to achieve three main goals:

(a) fast calculations over the whole spectral range;
(b) reasonable spectral grid sizes;
(c) accuracy of the simulated spectra.

The method has been devised as being fully parametrical, so as to allow potential users to decide which of the issues (a), (b) or (c) are of the upmost importance for a particular problem, and adapt the routine to the proposed needs. It will be shown that such improvements allow considering the line-by-line method as a credible and accurate approach, accessible to modern-day computational tools.

2. A sample case-study: simulation of atmospheric entry radiative processes

As discussed in the previous section, the simulation of atmospheric entry radiative processes represents a typical intricate case for radiative transfer calculations. Additionally to the large array of radiative processes encountered behind a shock-wave, one has to cope with the presence of large gradients in the macroscopic properties of the flow (temperature, species number densities, etc.). This means that numerical grids for radiative transfer calculations have to account for a large number of spatial cells (10^2-10^3). Such spatial grid sizes, coupled to the large spectral grid of each spatial cell, means that the computational overheads of this type of simulations may quickly become unaffordable. As an example of the typical spectra obtained in such conditions, two sample calculations of the spectral emission of an atmospheric pressure 97% CO_2–3% N_2 (Martian-type) mixture in thermochemical equilibrium at 5000 and 10,000 K are presented in Fig. 1.

Two aspects are immediately obvious when examining the calculated spectra. Firstly, the spectral features differ sensibly depending on the plasma temperatures (and hence compositions as we are assuming chemical equilibrium). Secondly, depending on the considered spectral range, radiative features may be abundant or scarce. This means that any adequate spectral calculation must have sufficiently adaptive features to be able to efficiently reproduce spectra as different as the ones presented in Fig. 1.

We may start by examining the problem boundaries: Spectral ranges to be considered for the simulation of plasma radiation typically spread from 10 to $10^6\,cm^{-1}$ (or more for some continua). For the typical conditions of an atmospheric entry, spectral lineshapes have widths of about $0.5\,cm^{-1}$. At least three points are required for resolving a line peak, which means that considering a fixed-width grid would amount to at least 6×10^6 spectral points, or more if the Voigt lineshapes are to be correctly reproduced. Given the current state-of-the-art computational capabilities, handling this type of grid sizes remains out of reach. Fixed-width methods are therefore limited to the simulation of restricted spectral regions which encompass the most paramount radiative features of the flow. One such example which can be presented is the recent entry of the Huygens probe in Titan's atmosphere. Here the radiation from the CN Violet system accounted for the almost overall radiative power of the plasma surrounding the probe. This has allowed utilizing fixed-width spectral grids for coupled calculations [4–7]. Nevertheless, nonuniform spectral grid approaches have been proposed in the past, considering a frequency division based on the equivalent widths of individual lines [8,9]. These are not known to have been extensively utilized in practical applications.

However, as can be seen in Fig. 1, one can take advantage of the fact that some spectral regions lack significant radiative features. Thus, one can define an adaptive grid which would be defined as to be tighter in spectral regions with a large number of lines, and more relaxed in regions with lesser lines. Also, to further attain the most compact grids, means of calculating accurate lineshapes with a minimal number of points have to be devised. Point (a) derives from point (b) in the sense that the methods utilized to calculate global spectral profiles over such grids must be computationally efficient, thus requiring a minimum number of function evaluations. Finally, the spectra computed over such adaptive grids must prove to follow closely high-resolution spectra, which would enforce point (c).

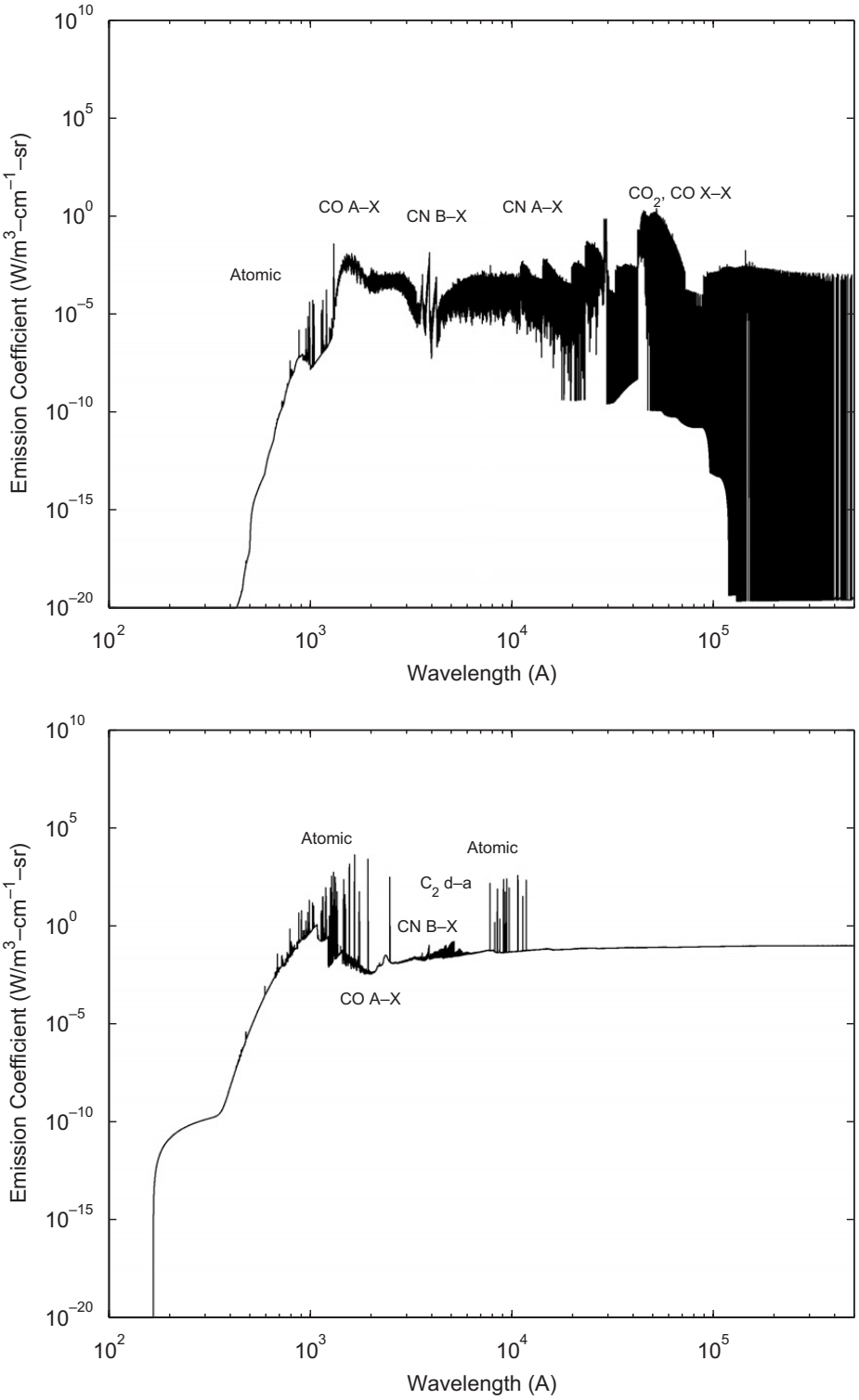

Fig. 1. Emission coefficients of an equilibrium Martian-type plasma at 5000 and 10,000 K.

3. An adaptive grid model for the simulation of plasma radiation

A fully adaptive spectral method is proposed here for the calculation of emission of an absorption spectra. This means that the method proposed here is capable of receiving as an input an arbitrary list of lines with their five key parameters (position, emission and absorption coefficients, Doppler and Lorentz full width at half maximum (FWHM); line shifting is not considered here), returning an overall spectra of global emission

$\varepsilon_{\bar{\nu}}$ and absorption $\alpha(\bar{\nu})$ coefficients over an adaptive spectral grid. Such method incorporates the following elementary steps: (1) selection of lines to be calculated explicitly or as a pseudo-continuum, (2) calculation of individual lineshapes and pseudo-continua and (3) combination of individual lineshapes and continua to yield the global spectra.

3.1. Identification of strong and weak lines and the pseudo-continuum radiation approach

As discussed previously, simulating the overall spectral properties of an atmospheric entry plasma implies calculating a large number of lines due to the presence of molecular radiation. It is clear that explicitly accounting for a large number of lines is not manageable in spectral calculations. An approach which is proposed for reducing the number of calculated lines, while not simply discarding weaker lines as it is common practice, includes accounting for weak lines as an effective continua.

Firstly, we consider two user-defined thresholds named *threshold*1 and *threshold*2. From a given line database, normalized to the database strongest line emission or absorption coefficient, we proceed to define strong lines as lines above the first threshold, weak lines as lines between the two thresholds and very weak lines as lines below the second threshold. An arbitrary example of strong, weak, and very weak lines is presented in Fig. 2.

Here, strong lines are explicitly calculated using a Voigt lineshape and the very weak lines are calculated as a fixed interval continuum. The pseudo-continua spectral interval is defined as $C \times FWHM_{\mathrm{med}}$ (parameter *contstep*) Where C is a constant depending on the ratio of the two thresholds (typically 20 for a ratio of 1000). Regarding the weak lines, a distinction is made depending on whether the weak line is covered by a strong line or not (See Fig. 2). A weak line is considered to be covered by a strong line if its line center is a distance of less than $C \times FWHM$ (parameter *dnu*). C depends on the ratio of the two thresholds and may also be typically set as equal to 20 for a ratio of 1000. The pseudo-continua is straightforwardly calculated adding the intensities of the weak and very weak lines which fall inside each of its intervals. It is chosen to account for weak and very weak lines as a continuum instead of simply discarding them, because if a very large number of lines are present, their summed contribution to the overall spectra might not be negligible. Typically, only about 10% of the overall lines are calculated explicitly.

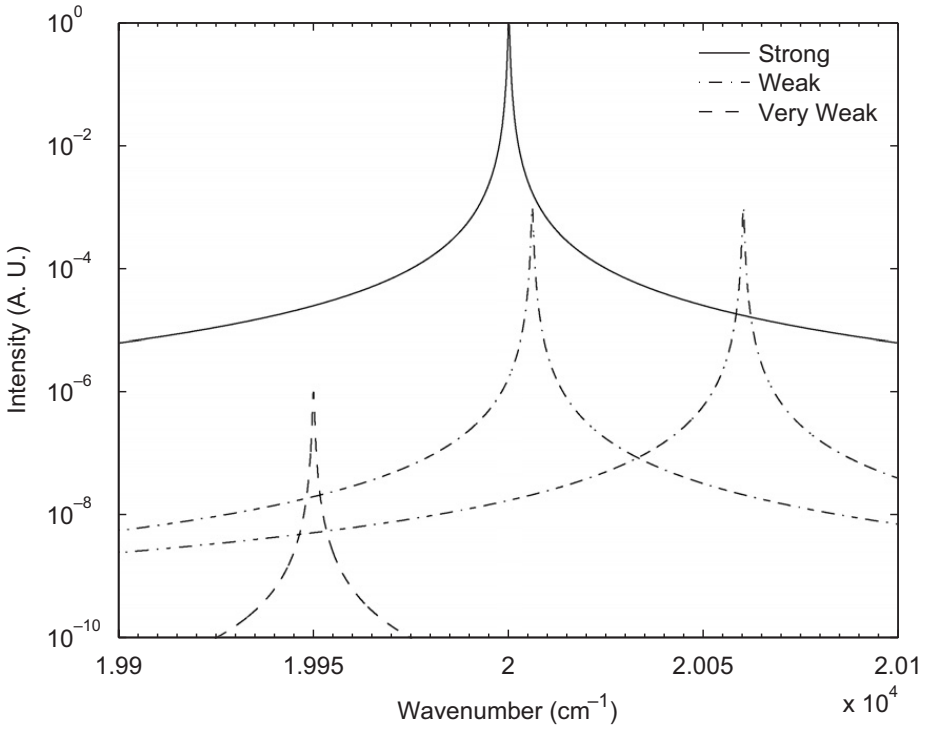

Fig. 2. Sample strong, weak and very weak lines (with *threshold*1 = 10^3 and *threshold*2 = 10^6).

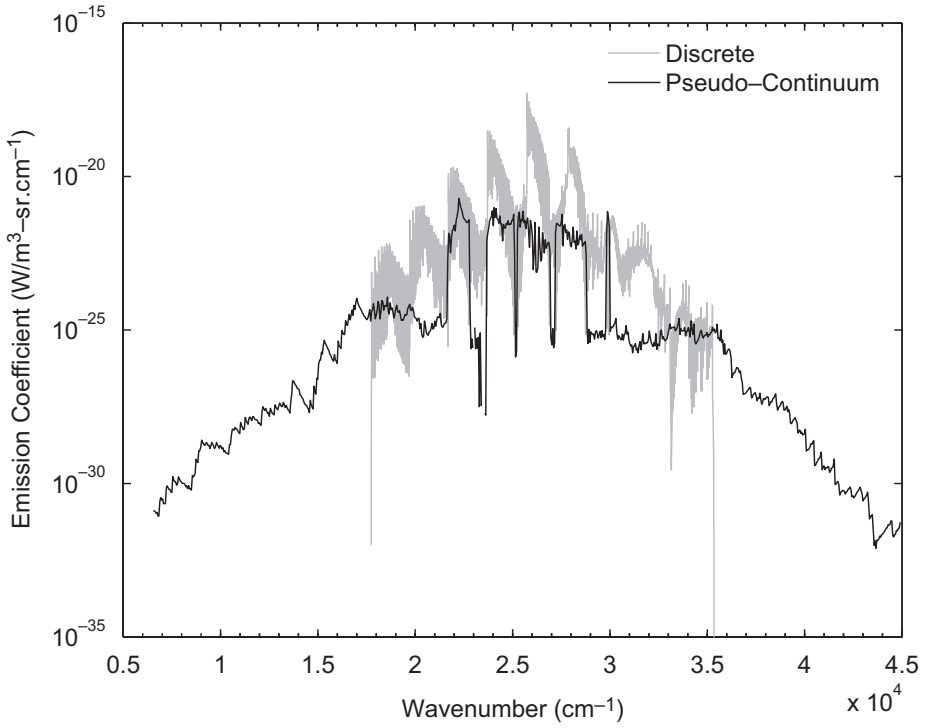

Fig. 3. Spectral simulation of the molecular CN Violet System $\Delta v = 0$, utilizing the hybrid line-by-line/pseudo-continuum approach. The pseudo-continuum spectrum encompassing weak and very weak lines is plotted in black, the discrete line-by-line spectrum encompassing strong and weak lines is plotted in light grey. As expected, the pseudo-continuum spectrum remains well below the discrete (line-by-line) spectrum.

An example of a spectral calculation for the CN Violet System (one molecule at an equilibrium temperature of 5000 K) is presented in Fig. 3. The parameters have been chosen such as: $threshold1 = 10^3$, $threshold2 = 10^6$, $contstep = 20 \times FWHM_{\text{med}}$ and $dnu = 20 \times FWHM$.

Here it can be seen that the strong lines, for diagonal transitions, are selected to be calculated according to the line-by-line method, whereas the nondiagonal weak lines are selected to be calculated as a pseudo-continuum. This is a typical trend of the molecular spectra calculated according to this method.

3.2. Calculation of individual Voigt line profiles

The method for calculating the selected strong and weak lines, according to the line-by-line approach, will be discussed in this section. The basic approach for the calculation of a Voigt lineshape will be firstly presented, followed by the presentation of a method for accurately calculating such lineshapes with a minimum number of points, using an adaptive spectral grid.

The convolution of collisional and Doppler broadening processes, respectively defined, by a Lorentz and a Gauss line profile, yields a so-called Voigt profile:

$$\begin{aligned} v(x) &= \ell(x) \otimes g(x), \\ &= \frac{\Delta v_{\text{L}}}{\Delta v_{\text{G}}} \sqrt{\frac{\ln 2}{\pi^3}} \int_{-\infty}^{+\infty} \frac{\exp[-(\xi - x)^2 \ln 2 / \Delta v_{\text{G}}^2]}{\xi^2 + \Delta v_{\text{L}}^2} \, \mathrm{d}\xi, \quad x = v - v_0. \end{aligned} \tag{1}$$

Such a line profile cannot be solved to an analytical expression, and several approximated methods have been proposed for carrying such calculations [10,11]. More recently, Fourier-transform methods have also been proposed for high-resolution calculations of these line profiles [12].

For the simulation of atmospheric entry radiative processes, accuracy requirements for radiative transfer calculations are less stringent than for other applications, such as remote atmospheric sensing. For most of the

Table 1
Gridpoints for 5, 7, 9, and 11 point lineshapes

Number of points	Selected points					
	$\bar{\nu}_0$	V/8	V/2	W	FW	25V/2
5	×			×		×
7	×			×	×	×
9	×		×	×	×	×
11	×	×	×	×	×	×

An × defines a specific point being accounted for in the given lineshape.

spectral range (except in the VUV and certain IR regions) the optical medium is typically optically thin, and spatial grids deployed in radiative transfer calculations have short lengths. Instead requirements regarding computational overheads are much more stringent. For such a case, the approximation to the Voigt profile proposed by Whiting [13] and extended by Olivero [14] is particularly adequate as it provides an analytical expression with a claimed precision of 0.02% to the exact profile:

$$v(\bar{\nu}) = C_1 \mathrm{e}^{-4\ln 2 D^2} + \frac{C_2}{1+4D^2} \cdots + 0.016 C_2 \left(1 - \frac{\Delta\bar{\nu}_\mathrm{L}}{\Delta\bar{\nu}_\mathrm{L}}\right)\left(\mathrm{e}^{-0.4 D^{2.25}} - \frac{10}{10 + D^{2.25}}\right), \tag{2}$$

with

$$\Delta\bar{\nu}_\mathrm{V} = \frac{1}{2}\left(1.0692\Delta\bar{\nu}_\mathrm{L} + \sqrt{0.86639\Delta\bar{\nu}_\mathrm{L}^2 + 4\Delta\bar{\nu}_\mathrm{G}^2}\right),$$

$$D = \frac{\bar{\nu} - \overline{\nu_0}}{\Delta\bar{\nu}_\mathrm{V}},$$

$$C_1 = \frac{(1 - \Delta\bar{\nu}_\mathrm{L}/\Delta\bar{\nu}_\mathrm{V})}{\Delta\bar{\nu}_\mathrm{V}(1.065 + 0.047(\Delta\bar{\nu}_\mathrm{L}/\Delta\bar{\nu}_\mathrm{V}) + 0.058(\Delta\bar{\nu}_\mathrm{L}/\Delta\bar{\nu}_\mathrm{V}^2))},$$

$$C_2 = \frac{(\Delta\bar{\nu}_\mathrm{L}/\Delta\bar{\nu}_\mathrm{V})}{\Delta\bar{\nu}_\mathrm{V}(1.065 + 0.047(\Delta\bar{\nu}_\mathrm{L}/\Delta\bar{\nu}_\mathrm{V}) + 0.058(\Delta\bar{\nu}_\mathrm{L}/\Delta\bar{\nu}_\mathrm{V}^2))}.$$

The main objective being the calculation of a line profile as close to Eq. (2) as possible, while retaining a minimum number of points, a method has been devised in order to obtain an adapted grid of key points where the expression of Eq. (2) is to be evaluated. The resulting profiles are found to adequately approximate the Voigt profile of Whiting and Olivero, to a user-defined precision which will depend on the number of considered grid points.

Firstly a set of low-resolution line profiles have been defined for allowing quick spectral calculations yielding a compact overall spectral grid. Four line profiles with, respectively, 5, 7, 9 and 11 grid points have been defined, introducing the parameters, W and FW which define the boundaries between the line center region, the "near" line wings, and the "far" line wings, respectively. The expression for those parameters, for a given Voigt profile, is proposed by Zhu [15]:

$$[W, FW] = \frac{2}{\pi}(1+\zeta)\Delta\bar{\nu}_\mathrm{L} + \beta\Delta\bar{\nu}_\mathrm{D} \tag{3}$$

the $[\zeta, \beta]$ constants are held at à $[1, 1.8]$ for the calculation of the parameter W as proposed by Smith [16], and held at $[2.6, 5.8]$ for the calculation of the parameter FW according to a critical analysis carried by the author on sample Lorentz, Doppler and Voigt profiles. The different grid points have been defined accordingly,[1] and are presented in Table 1.

[1]Considering a zero line intensity for the last grid point.

A different method has been devised for the calculation of high-resolution profiles. Two line parameters par_c and par_w have firstly been defined, related to the line center and line wings, respectively. The line center being identical whether the profile is Lorentz or Doppler, par_c will be independent of the parameters $\Delta\overline{\nu}_L$ and $\Delta\overline{\nu}_D$.

The lineshape wings will, however, be very different regarding whether the line profile is Doppler or Lorentz. par_w will therefore have a strong dependence on the parameters $\Delta\overline{\nu}_L$ and $\Delta\overline{\nu}_D$, and such dependence has been acknowledged in the following way:

$$par_w = par_{wL} + \frac{\Delta\overline{\nu}_D}{\Delta\overline{\nu}_D + \Delta\overline{\nu}_L} par_{wD}, \tag{4}$$

such that for a Lorentz lineshape we have $par_w = par_{wL}$ and for a Doppler lineshape we have $par_w = par_{wL} + par_{wD}$.

A series of monotonous points has then been defined such as

$$i_0 = [0 : \max/(num_c - 1) : \max], \tag{5}$$

and a geometrical transform is applied such that

$$i = \frac{1 - \exp(par_{(c,w)} \times i_0)/\exp(par_{(c,w)} \times i_0(\max))}{1 - \exp(par_{(c,w)} \times i_0(1))/\exp(par_{(c,w)} \times i_0(\max))}. \tag{6}$$

We then define $i_c = i$ and $i_w = 1 - i$. An example of the geometrical transforms i_c and i_w, obtained for specific par_c and par_w values, is presented in Fig. 4.

Practically speaking, such transformations return two grids more or less tightened around the values 0 or 1.

These two grids need now to be put to use. Firstly, for distributing the grid points in the line center region, the second derivative of the Voigt profile is firstly calculated. Then the line profile points $\overline{\nu}_i$ are determined

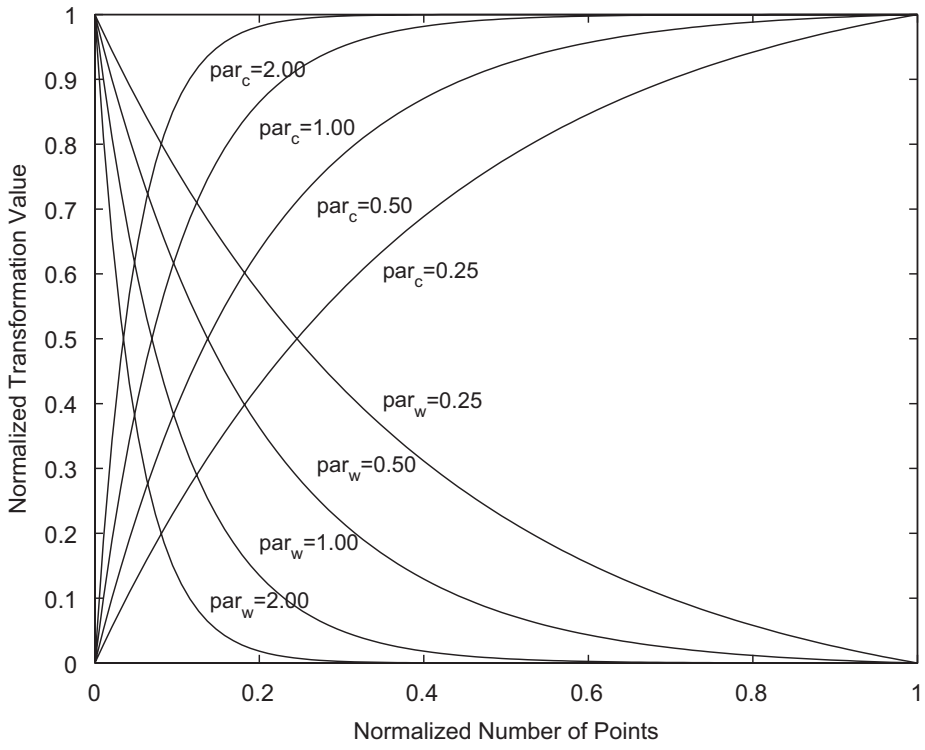

Fig. 4. Plot of the numerical transforms yielding the unevenly spaced gridpoints i_c and i_w from the evenly spaced gridpoints i, for different values of the adjustable parameters par_c and par_w.

according to the relation:

$$i_c = \frac{v''(\overline{\nu}_i)_c}{\max[v''(\overline{\nu}_i)_c]} \tag{7}$$

which means that the spectral grid will be tighter in the profile regions with large second derivatives (near the line center). Here, the second derivative is a good variational parameter as it allows an optimum distribution of lineshape points, ensuring an adequate reproduction of the exact lineshape through the linear connection of such points.

The line wings structure is such that the optimal grid points distribution is considered to be given by the relation

$$i_w = \frac{v(\overline{\nu}_i)_w}{\max[v(\overline{\nu}_i)_w]}, \tag{8}$$

which allows distributing the grid points efficiently in the "far" wings regions where the intensity decrease is very slow (thus explaining the tightening of the parameter i_w near 0).

We may now assign a given number of points to be distributed near the line center and the line wings. The calculation routine then proceeds according to the described method in order to optimally distribute such points. More precise line profiles will be obtained for a larger number of assigned grid points, at the cost of increased spectral grids and calculation times.

Different low- and high-resolution lineshapes have been compared with the exact Voigt profiles (Eq. (2)) with $\Delta\overline{\nu} = 5\,\mathrm{cm}^{-1}$. The differences to the exact profile have also been determined for each of such profiles. The obtained results are presented in Fig. 5 for low-resolution profiles, and in Fig. 6 for high-resolution profiles.

3.3. Handling and overlay of individual lineshapes

Following the definition of a method for adaptively calculating individual lineshapes, one may apply it to the calculation of the individual lineshapes for each of the calculated radiative transitions (with their accompanying Doppler and Lorentz FWHM). However, doing so for a large number of lines (typically more than 10^4) might still yield large calculation times. One can acknowledge that the systematic evaluation of exponential terms of Eq. (2) for the calculation of several thousand lines might be an ineffective method. Instead, one can take advantage of the fact that the different lineshapes Doppler and Lorentz FWHM remain very close over a large spectral range. The calculated lineshapes are then nearly equivalent and there is no need to systematically recalculate them.

As an example, the differences between two Voigt lineshapes, for a 10% variation of their Lorentz and Doppler FWHM, are presented in Fig. 7. Given the small differences between such spectra, one may chose not to recalculate a spectral lineshape if both the Lorentz and Doppler FWHM differ less than by a given percentage (10% being an adequate value).

Such approach further improves computational efficiency, as for most of the transitions to be simulated, the calculation routine merely replicates the previous lineshape spectral grid points and relative intensities, simply multiplying the relative line intensities by the line strength to yield the absolute line intensities.

Once that the spectral lineshapes have been calculated for each of the overall database transitions, such individual lineshapes then have to be combined to yield an overall spectra.

This is firstly done considering the overall calculated grid points and grouping them in an increasing order. Secondly, the spectral points too close to each other by a defined parameter (named *minstep* and typically $\frac{1}{40}$ of the FWHM) are grouped. Finally, each individual lineshape is interpolated over the boundaries of the overall spectral grid which falls inside the first and last grid points of the individual lineshape. The overall discrete spectrum is then overlaid to the previously calculated "pseudo-continuum" spectrum to yield the final spectrum.

In brief, this proposed adaptive grid method represents an approach where a series of approximations ("pseudo-continuum", calculation of Voigt lineshapes with a minimum number of points, nonsystematic lineshape recalculation) are carried in order to achieve consequent reduction of calculation times and spectral grids. One more advantage of the proposed method is the fact that it is fully user-parametrizable, and allows

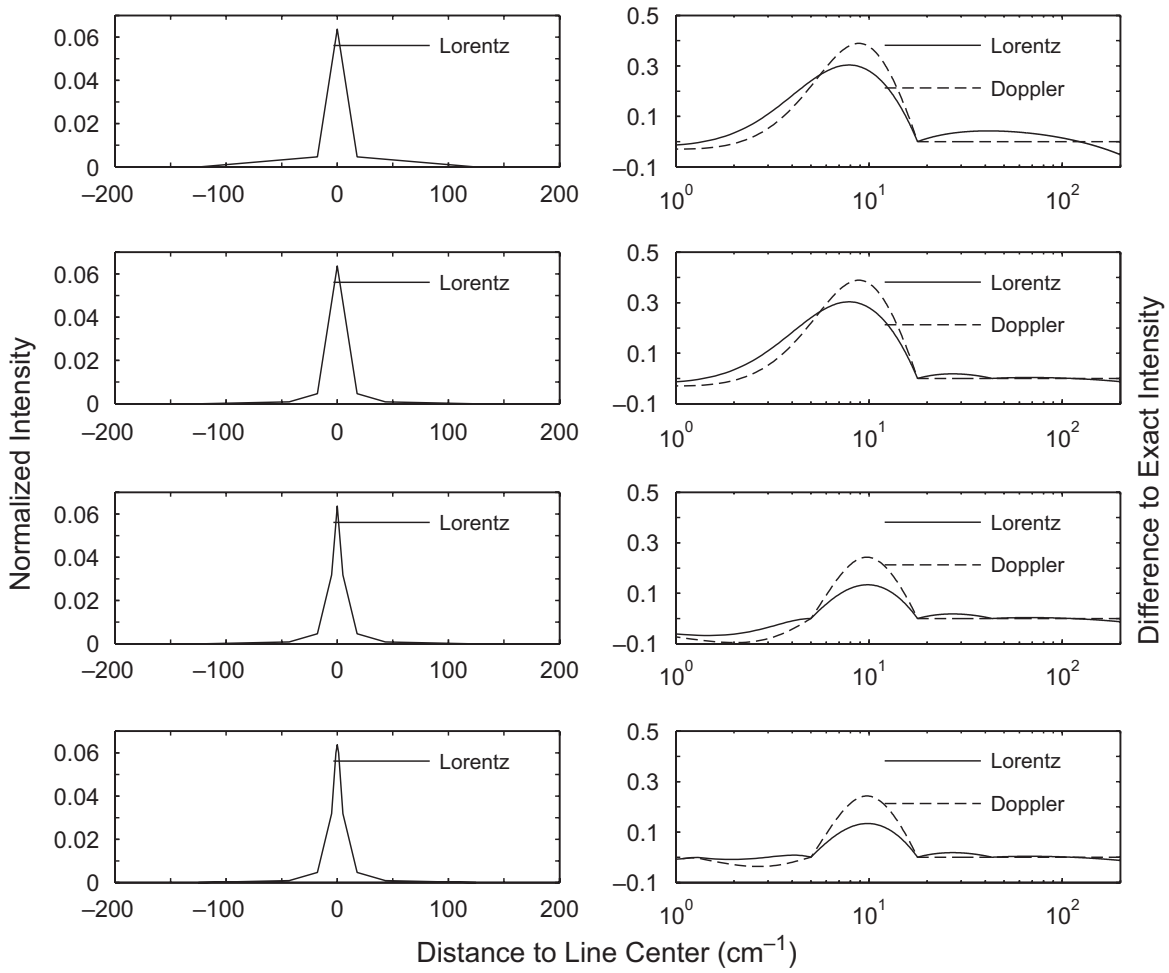

Fig. 5. Plot of low-resolution Lorentz lineshapes (left; 5, 7, 9 and 11 points from top to bottom; $\Delta\bar{\nu} = 5\,\mathrm{cm}^{-1}$) and plot of the normalized difference of Lorentz (full line; $\Delta\bar{\nu} = 5\,\mathrm{cm}^{-1}$) and Doppler (dotted line; $\Delta\bar{\nu} = 5\,\mathrm{cm}^{-1}$) lineshapes to the exact lineshapes (right; 5, 7, 9 and 11 points from top to bottom).

one to chose the level of accuracy (with the associated memory and computational overheads) when carrying spectral calculations.

3.4. Deployment of adaptive spectral grids in radiative transfer calculations

Handling adaptive spectral grids in radiative transfer calculations poses some additional challenges compared to fixed-width spectral grids. If radiative transfer models such as Monte-Carlo or ray-tracing methods are to be utilized, this is not an issue, as such methods typically probe a narrow spectral region at a time. Thus, one can straightforwardly convert the considered adaptive grid region to a high-resolution local spectral grid. This is no longer the case if radiation transfer is treated explicitly, accounting for the overall spectrum. Here a problem arises from the fact that depending on the local conditions of the plasma, the spectral grids will differ. As an example, the gradients of the spectral grids for the simulated spectra presented in Fig. 1, and the gradient for an additional spectral grid for the same Martian-type plasma in equilibrium conditions at 1000 K are presented in Fig. 8.

From the analysis of Fig. 8, one may conclude that although the spectral grids may be rather alike (grids for the CO_2–N_2 plasma at 5000 and 10,000 K) they are not exactly equal, owing to different line intensities, calculated explicitly or not depending on the plasma temperature, owing to different Doppler broadening widths, etc. For the 1000 K temperature, the spectral grid differs significantly, as different radiative transitions account for the main radiative features of the plasma. For such a low temperature, radiation is mainly

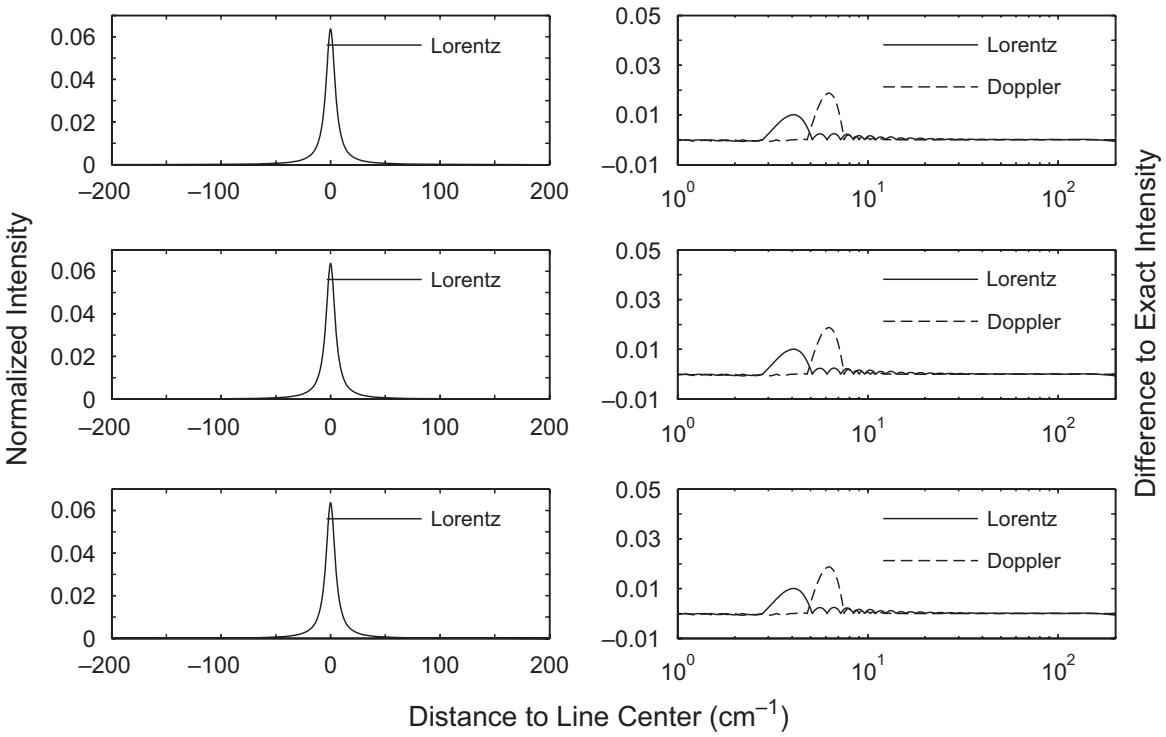

Fig. 6. Plot of high-resolution Lorentz lineshapes (left; 21, 37 and 73 points from top to bottom; $\Delta\bar{v} = 5\,\mathrm{cm}^{-1}$) and plot of the normalized difference of Lorentz (full line; $\Delta\bar{v} = 5\,\mathrm{cm}^{-1}$) and Doppler (dotted line; $\Delta\bar{v} = 5\,\mathrm{cm}^{-1}$) lineshapes to the exact lineshapes (right; 21, 37 and 73 points from top to bottom).

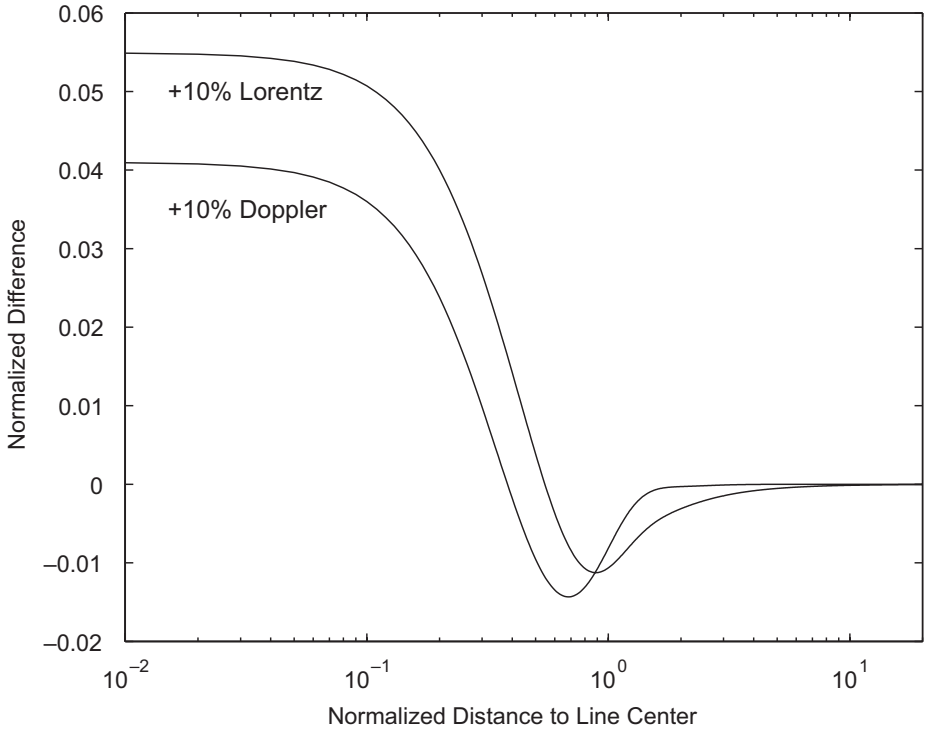

Fig. 7. Normalized difference between two Voigt lineshapes with $\Delta\bar{v}'_{\mathrm{L}} = 1.1\Delta\bar{v}_{\mathrm{L}}$ and $\Delta\bar{v}'_{\mathrm{D}} = 1.1\Delta\bar{v}_{\mathrm{D}}$, and an initial Voigt lineshape with $\Delta\bar{v}_{\mathrm{L,D}} = 5\,\mathrm{cm}^{-1}$.

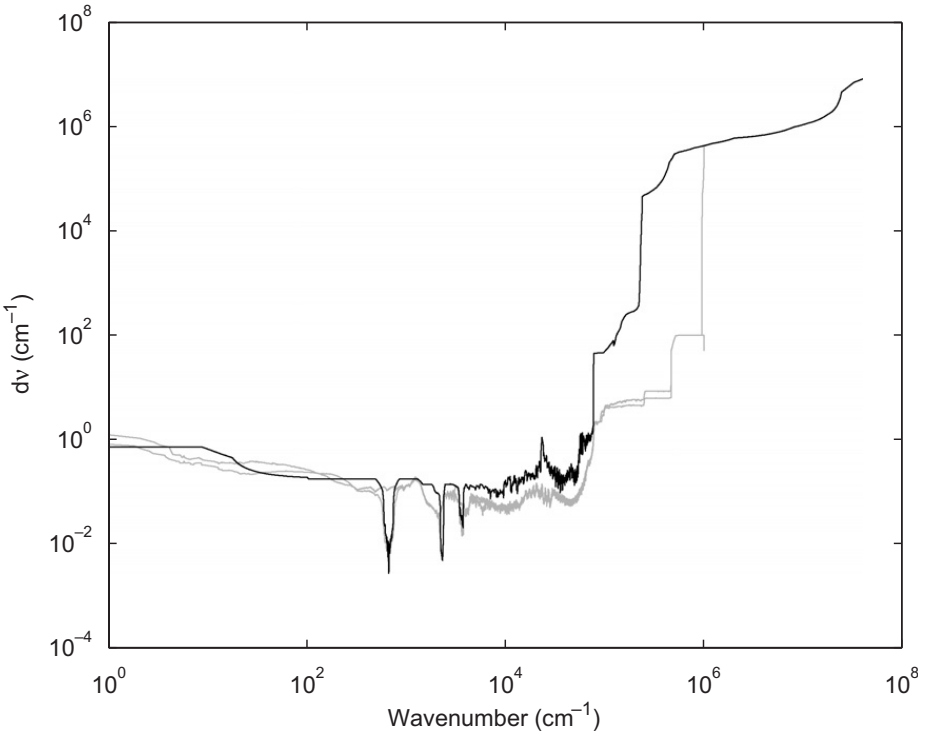

Fig. 8. Spectral gradients for the spectral grids obtained for 97% CO_2–3% N_2 plasmas in thermal equilibrium at 1000 K (black), 5000 and 10,000 K (grey). The gradients reproduced in grey correspond to the spectral grids of Fig. 1.

emitted/absorbed by the CO_2 infrared transitions, which explains the tightened grid near the three main radiative modes of CO_2 at 666, 2300 and 3700 cm^{-1}.

A first approach that could be devised for radiative transfer calculations would be combining adjacent spectral grids and then removing the spectral points too close from each other. However, this is rather inefficient as carrying radiative transfer calculations over a given spatial grid will result in ever increasing spectral grids. Instead, it is recommended that the spectral grids obtained for each radiative system are compared for adjacent spatial cells.

Although grid point distributions may vary a little due to different line broadening widths, the spectral grids of a given radiative transition, obtained in the different spatial cells, will remain very close. One may take advantage of this by comparing the individual grids of each cell, selecting the largest grid: If there is strong emission/absorption in the initial cell and weak emission/absorption in the adjacent cell, the adjacent cell spectrum will remain close to the initial cell spectrum, thus justifying utilizing the first cell spectral grid. For the inverse case of figure, the spectrum will be strongly dependent on the adjacent cell spectral properties, thus justifying the use of this cell spectral grid.

After selecting the appropriate grids for each given radiative system, one only needs to combine such grids to obtain the adequate grid for radiative transfer calculations between two adjacent cells. This approach allows keeping consecutive grid sizes at a balanced level, while allowing essential radiative behavior to be adequately captured and reproduced.

4. Accuracy and validation of the method

Sample radiative transfer calculations have been carried out using the different low- and high-resolution spectra, calculated according to the adaptive model presented in this paper. Comparisons of the transmitted radiative power have been carried out against calculations utilizing very high-resolution spectra. This allows an estimation of the accuracy of the different spectra liable to be provided by the method.

For such purposes, the problem of hot radiation absorption by a cold gas layer is one of the more stringent radiative transfer problems that can be considered. Accordingly, adequate test-cases have been defined, probing radiative transitions between a ground state and a radiative state, where line radiation re-absorption in the cold gas layer will be of paramount importance.

The two upmost important parameters of this variable grid method are the number of grid points utilized for individual lineshape calculations, and the thresholds for strong, weak, and very weak lines separation. Consequently, two different test-cases have been defined: A first test-case which examines radiative transfer involving a triplet atomic transition, and a second test-case which examines radiative transfer involving a diatomic vibronic band. Transitions in the VUV region have been chosen as test-cases, to ensure that strong absorption coefficients are obtained in the different test-cases.

4.1. Lineshape accuracy

The examination of the accuracy for the different calculated lineshapes has been carried out defining a test-case where the triplet atomic transition $2s^2 2p^3 - 2s^2 2p^2(^3P)3d$ of atomic nitrogen at 953 Å is simulated, assuming a constant number density of $6 \times 10^{23}\,\mathrm{part/m^3}$.

A first benchmark calculation has been carried for a restrictive case of radiative transfer from a hot slab at 20,000 K to a cold slab at 1000 K (case 1). However, such a restrictive case is not likely to be encountered, except perhaps for atmospheric entry applications, considering the simulation of radiative transfer upstream of a shockwave. A second benchmark, with lower temperature gradients, has therefore been defined, with a hot slab at 10,000 K and a cold slab at 5000 K (case 2). The different slab geometries are presented in Table 2. Fig. 9 presents the radiative power exiting from slabs 0 and 1 for two sample conditions. Low-resolution lineshapes have the index *l*5, *l*7, *l*9 and *l*11 for the 5, 7, 9 and 11 point lineshapes, respectively. High-resolution lineshapes have the index *c*3*w*6, *c*6*w*12 and *c*8*w*16 for 21 point (7 core and 14 wings points), 39 point (13 core and 26 wings points) and 51 point (17 core and 34 wings points) lineshapes, respectively. The obtained results, for different absorption slab lengths, are presented in Tables 3 and 4.

From the analysis of case 1, one may verify that for very large lengths, only the most precise lineshapes are able to accurately reproduce the radiative features at the exit of slab 1. Regarding radiative transfer in a 10 km slab, only 2.5% of the radiative power incoming from slab 0 is retrieved (see calculation results with the *c*8*w*16 lineshape). Compared to these results, the 21 and 39 point lineshapes (*c*6*w*12 and *c*3*w*6) strongly underpredict the outgoing radiation (20% and 0% of the outgoing radiation, respectively). On the other hand, low-resolution lineshapes (*l*5, *l*7, *l*9 and *l*11) overpredict the emitted radiation (up to 1650% more). This is not surprising as the lineshapes strongly differ among the two slabs (mainly due to Doppler effects, the lineshape being narrower in the cold slab), and as only a very little portion of the wings radiation will be transmitted over such a long length. For narrower slabs (1 km and 0.1 m), the errors incurred when utilizing coarser lineshapes are significantly lower.

This brings us to the analysis of case 2, where the temperature gradients and slab lengths are lower. Here we can verify that the coarser lineshapes are able to accurately reproduce the radiative transfer behavior, even for large extinction percentages (with less than 1% of transmitted radiative power). Only the lower resolution lineshapes somehow fail at accurately reproducing the radiative transfer features for longer cold slab lengths (up to 500% difference to the reference lineshape). Regarding high-resolution lineshapes, a coarser lineshape such as *c*3*w*6 suffices for adequately treating the examined problem.

Table 2
Slabs for sample radiative transfer benchmark calculations for the accuracy test of lineshapes with a different number of points (5–73 points)

$T_0 = 20,000\,\mathrm{K}$	$T_1 = 1000\,\mathrm{K}$
$x_0 = 1\,\mathrm{m}$	$x_1 = 0.1\,\mathrm{m},\ 1\,\mathrm{km},\ 10\,\mathrm{km}$
$T_0 = 10,000\,\mathrm{K}$	$T_1 = 5000\,\mathrm{K}$
$x_0 = 1\,\mathrm{m}$	$x_1 = 1\,\mathrm{m},\ 10\,\mathrm{m},\ 1\,\mathrm{km}$

Each slab has a given homogenous temperature throughout it's specified length.

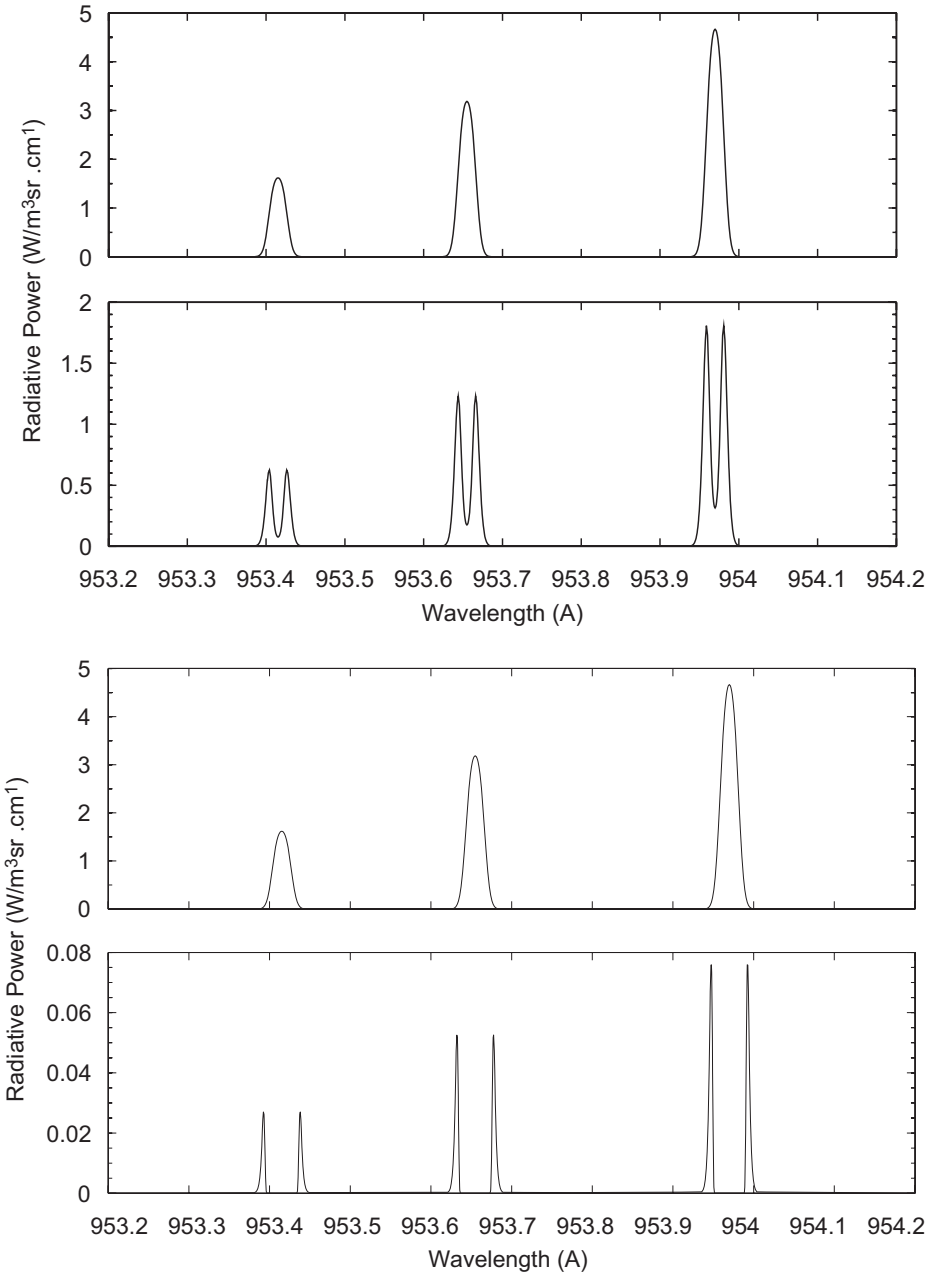

Fig. 9. Sample radiative transfer calculation for nitrogen atomic radiation utilizing high resolution lineshapes (see Table 2). Two sample cases are shown where the radiative features exiting the hot slab and entering the cold slab are plotted in the upper part of the figure and the radiative features exiting the cold slab are presented below. Here, calculations for case 1 are presented with, from top to bottom: hot slab exit with $x_0 = 1\,\mathrm{m}$, $T_0 = 20,000\,\mathrm{K}$; cold slab exit with $x_1 = 1\,\mathrm{m}$, $T_1 = 1000\,\mathrm{K}$; hot slab exit with $x_0 = 1\,\mathrm{m}$, $T_0 = 20,000\,\mathrm{K}$; cold slab exit with $x_1 = 1\,\mathrm{km}$, $T_1 = 1000\,\mathrm{K}$.

4.2. Accuracy of the "pseudo-continuum" approach

A similar sample radiative transfer problem has been considered for testing the "pseudo-continuum" approach, accounting this time for the $\Delta v = 0$ band of the CO fourth positive system at 1600 Å, and assuming a constant number density of $3.7 \times 10^{20}\,\mathrm{part/m^3}$. A radiative transfer case has been devised where only $\frac{1}{3}$ of the incoming radiation is retrieved. The two slabs are in thermal equilibrium with temperatures of 5000 and 1000 K respectively, and are presented in Table 5. Different thresholds for defining strong, weak and very weak lines have been chosen. $t16t212$ stands for $threshold1 = 10^6$ and $threshold2 = 10^{12}$; $t13t26$ stands for $threshold1 = 10^3$ and $threshold2 = 10^6$ and so on.

Table 3
Radiative transfer results for different lineshapes; case 1, see Table 2.

	Case 1: $T_0 = 20,000$, $T_1 = 1000$			
	I_0, $x_0 = 1\,\mathrm{m}$	I_1, $x_1 = 0.1\,\mathrm{m}$	I_1, $x_1 = 1\,\mathrm{km}$	I_1, $x_1 = 10\,\mathrm{km}$
*c*8*w*16	37,425.021	33,609.895	11,061.844	901.319
*c*6*w*12	37,362.679	33,579.270	9332.971	180.892
*c*3*w*6	37,137.075	33,559.071	1079.988	0.003
*l*11	38,622.523	35,253.188	12,294.190	11,873.855
*l*9	38,120.998	35,585.727	12,816.890	12,362.364
*l*7	36,090.270	33,636.470	15,454.166	14,902.383
*l*5	37,921.303	31,679.264	5940.018	5940.018
I_1/I_0				
*c*8*w*16		89.81%	29.56%	2.41%
*c*6*w*12		89.87%	24.98%	0.48%
*c*3*w*6		90.37%	2.91%	0.00%
*l*11		91.28%	31.83%	30.74%
*l*9		93.35%	33.62%	32.43%
*l*7		93.20%	42.82%	41.29%
*l*5		83.54%	15.66%	15.66%
$I_1/(I_1)_{\mathrm{hires}}$				
*c*8*w*16		100.00%	100.00%	100.00%
*c*6*w*12		99.91%	84.37%	20.07%
*c*3*w*6		99.85%	9.76%	0.00%
*l*11		104.89%	111.14%	1317.39%
*l*9		105.88%	115.87%	1371.59%
*l*7		100.08%	139.71%	1653.40%
*l*5		94.26%	53.70%	659.04%

The table successively reports the radiative intensity exiting from the hot (I_0) and cold (I_1) slabs, the percentage of the incoming hot slab radiative intensity transmitted by the cold slab (I_1/I_0), and the differences in transmissivity compared to high-resolution calculations ($I_1/(I_1)_{\mathrm{hires}}$).

The radiative transfer calculation results are presented in Table 6 and a sample calculation is presented in Fig. 10.

From the analysis of the obtained results, one may verify that the thresholds can be significantly lowered without largely affecting the accuracy of the obtained results. Differences between the more stringent and more relaxed thresholds only amount to 13%. Computation times are, however, divided by a factor of four. Nevertheless, defining thresholds lower than 10^3 is not recommended if consistency of the calculated spectra is to be assured. Either way it is demonstrated that the ''pseudo-continuum'' is a very effective method for decreasing molecular spectra calculation times without a significant loss in the accuracy of the obtained results.

5. Possible model extension for the simulation of general radiative transfer problems and comparison with other numerical approaches

Although the line-by-line method is routinely utilized in spectral simulations of low-pressure plasmas, the systematic evaluation of different line-by-line models has rather been carried in the scope of atmospheric sensing applications, and to a lesser extent, astrophysical applications. This can be easily understood considering the typical radiative problems to be solved in low-pressure plasma applications: Investigations are usually carried out in the near-UV to near-IR range (300–900 nm), and over short length scales (centimeter-wise). This means that the medium can be usually considered as optically thin, thus not requiring stringent

Table 4
Radiative transfer results for different lineshapes; case 2, see Table 2.

	Case 2: $T_0 = 10,000$, $T_1 = 5000$			
	I_0, $x_0 = 1\,\mathrm{m}$	I_1, $x_1 = 1\,\mathrm{m}$	I_1, $x_1 = 10\,\mathrm{m}$	I_1, $x_1 = 1\,\mathrm{km}$
*c*8*w*16	24.9190	9.1768	2.3393	0.1907
*c*6*w*12	24.8430	9.1584	2.3591	0.1963
*c*3*w*6	24.6754	9.1951	2.5884	0.1657
*l*11	26.4886	10.5922	2.4937	0.6705
*l*9	27.4778	11.4270	2.7297	0.8839
*l*7	24.6807	9.5831	3.2066	0.9865
*l*5	34.3964	19.4701	9.6988	0.6524
I_1/I_0				
*c*8*w*16		36.83%	9.39%	0.77%
*c*6*w*12		36.87%	9.50%	0.79%
*c*3*w*6		37.26%	10.49%	0.67%
*l*11		39.99%	9.41%	2.53%
*l*9		41.59%	9.93%	3.22%
*l*7		38.83%	12.99%	4.00%
*l*5		56.61%	28.20%	1.90%
$I_1/(I_1)_{\mathrm{hires}}$				
*c*8*w*16		100.00%	100.00%	100.00%
*c*6*w*12		99.80%	100.85%	102.91%
*c*3*w*6		100.20%	110.65%	86.89%
*l*11		115.42%	106.60%	351.51%
*l*9		124.52%	116.69%	463.42%
*l*7		104.43%	137.08%	517.18%
*l*5		212.17%	414.60%	342.05%

The table successively reports the radiative intensity exiting from the hot (I_0) and cold (I_1) slabs, the percentage of the incoming hot slab radiative intensity transmitted by the cold slab (I_1/I_0), and the differences in transmissivity compared to high-resolution calculations ($I_1/(I_1)_{\mathrm{hires}}$).

Table 5
Slabs for sample radiative transfer benchmark calculations for testing the accuracy of the pseudo-continuum approach, sampling different values for the *threshold*1 and *threshold*2

$T_0 = 5000\,\mathrm{K}$	$T_1 = 1000\,\mathrm{K}$
$x_0 = 1\,\mathrm{m}$	$x_1 = 100\,\mathrm{km}$

Each slab has a given homogenous temperature throughout its specified length.

radiative transfer calculations. Recently, more complex simulations have been carried out, in which the spectral range has been extended to values as low as 200–250 nm. High-resolution experimental spectra measured in atmospheric pressure plasma torches have been rebuilt numerically, utilizing more detailed radiative transfer models [17–22]. The number of spectral lines considered in such simulations exceeds 10,000 individual lines.

However, most of the spectral investigations in low-pressure plasmas have been carried out as a nonintrusive method to examine excited molecular level populations (emission spectroscopy), or ground molecular level populations (absorption spectroscopy). Moreover, emissive or absorptive chemical species encountered in such plasmas are at most diatomic. This means that complex polyatomic spectra (triatomic or

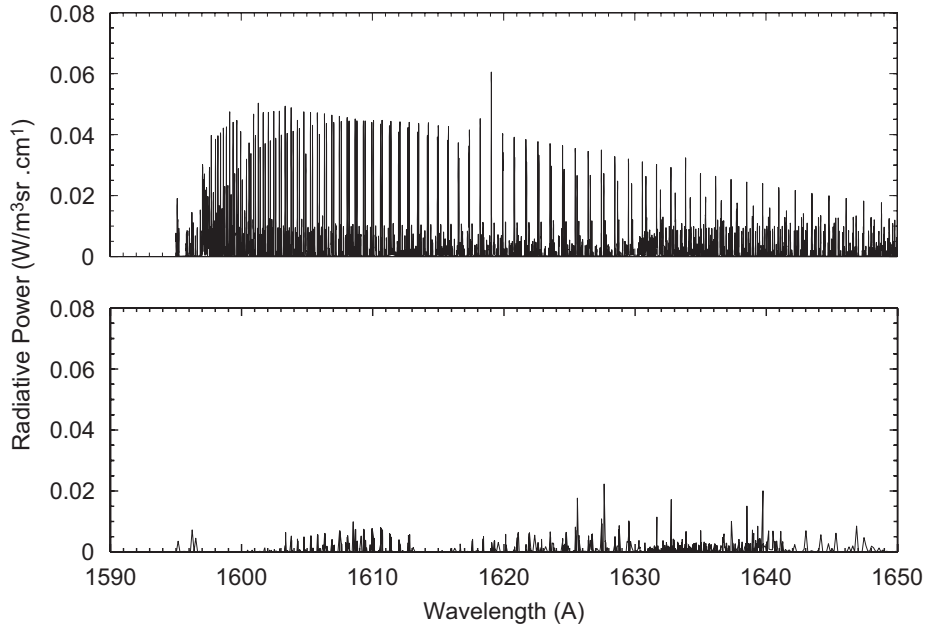

Fig. 10. Sample radiative transfer calculation for the CO Fourth Positive System $\Delta v = 0$ (see Table 5). Top: radiative features exiting the hot slab and entering the cold slab with $T_1 = 1000\,\mathrm{K}$ and $x_1 = 100\,\mathrm{km}$. Bottom: radiative features exiting the cold slab with $T_0 = 5000\,\mathrm{K}$ and $x_0 = 1\,\mathrm{m}$.

Table 6
Radiative transfer results for different "pseudo-continuum" threshold parameters (see figure in Table 5)

	$T_0 = 5000$, $T_1 = 1000$			
	I_0, $x_0 = 1\,\mathrm{m}$	I_1, $x_1 = 100\,\mathrm{km}$	I_1/I_0 (%)	$I_1/(I_1)_{\mathrm{hires}}$ (%)
*t*16*t*212	6.7057	2.2124	32.99	100.00
*t*13*t*26	6.7071	2.0987	31.29	94.86
*t*13*t*23	6.7071	1.9738	29.43	89.22
*t*12*t*23	6.6915	1.9128	28.59	86.46
	s		%	
Calculation times				
*t*16*t*212	61.7		100.00	
*t*13*t*26	41.5		67.25	
*t*13*t*23	36.1		58.44	
*t*12*t*23	14.5		23.48	

The table reports the radiative intensity exiting from the hot (I_0) and cold (I_1) slabs, the percentage of the incoming hot slab radiative intensity transmitted by the cold slab (I_1/I_0), and the differences in transmissivity compared to high-resolution calculations ($I_1/(I_1)_{\mathrm{hires}}$). Further below are reported the absolute and relative calculation times.

higher) are absent, and accordingly the number of spectral lines to be simulated may be as low as a few hundred, or as high as a few thousand of lines. This explains why numerical line-by-line methods utilized in such applications have not been significantly optimized: simple line-by-line methods, relying on fixed-width grids, yield detailed results without large memory or computational overheads.

Nevertheless, as discussed in Section 2, atmospheric entry applications have fostered the need for looking out for more efficient line-by-line methods, as this kind of application requires the calculation of more than one million spectral lines for each cell of the 3D spatial grid generated around a spacecraft. Considering that

spatial grids for radiative transfer applications may exceed one-hundred cells, each with very different plasma conditions (see Fig. 1), the necessity in optimizing the efficiency of line-by-line calculation routines becomes evident.

Furthermore, when one is to examine other existing approaches for achieving efficient line-by-line methods in radiative transfer calculations, it is important to study the approaches proposed in atmospheric sensing applications. Not only can these approaches be found to be applicable to low-pressure plasmas applications, but one may also examine the possibility of extending the method discussed in this article to the former applications. Currently, multi-grid approaches [23–26] appear to be amongst the most popular in this domain, although different methods have been proposed, based on the interpolation of reference absorption spectra simulated for different gas temperature increments [27].

Similarities with the approach discussed in this article include:

- Acknowledging different lineshape regions (core and wings regions) through the use of cascaded grids, where rapidly varying line center regions are sampled in fine resolution grids, and the smooth wings region are sampled over more coarser grids. Although this method differs from the one proposed in this article, the obtained results are somehow similar, as both methods consider a set of closely spaced grid points in the core region and a set of loosely spaced grid points in the wings region (see Section 3.2).
- Allowing a certain level of user parametrization, namely regarding error tolerances [25].
- Similar line selection criteria [23,28].

Differences include:

- In atmospheric sensing applications, a single line or a group of lines may be predominantly absorbing, which means that their influence on the overall gas transmissivity may extend well beyond their line center. Therefore, line profiles usually have to be calculated for a broad spectral range. The approach discussed in this article only considers a single (although variable step) grid. Although the algorithm discussed here considers the line cutoff (spectral limit above which the line intensity is considered to be zero) as an adjustable parameter (typically $[100-1000]\times FWHM$), broader line cutoff parameters come at the price of encompassing a large number of points to which the line profile has to be interpolated in the spectral grid. For such conditions, the algorithm discussed here might not be competitive when compared to the cascaded grids approach.
- The predominance of such intense absorption lines may mandate the application of different Voigt lineshape calculation routines, if the accuracy provided by the formulae of Eq. (2) (0.02%) is deemed insufficient. However, the approach discussed here is not dependent on a specific method for the calculation of a Voigt profile, and Olivero's expression (Eq. (2)) may be straightforwardly replaced by a different expression or algorithm. Eqs. (7) and (8) will then be calculated over the new high-accuracy profile, with the small difference that the second derivative in Eq. (7) will have to be determined using numerical methods if the high-accuracy Voigt profile is nonanalytic.

As a concluding remark on this subject, one may point out that the availability of a significant array of different methods for line-by-line calculations fosters the need for benchmarking calculations to be carried out in order to examine quantitatively the advantages of each method. Currently this is yet to be achieved: Several numerical codes have not been released for general use, and also one should not forget the inherent difficulties in handling and utilizing several different numerical algorithms by a single user.

6. Conclusions

An adaptive grid method for radiative transfer calculations in low-pressure plasmas has been presented and validated. Such method relies on two approaches of paramount importance for its successful application. The first approach is the "pseudo-continuum" concept which limits the number of lines which are to be explicitly calculated, and the second approach is the method for the calculation of accurate Voigt lineshapes with a minimum number of points. One of the major advantages of this model is that the proposed method is fully

parametric, leaving the user with the choice of adapting the calculation parameters to its specific requirements, likely to be linked to the available computing power. A grand total of 25 parameters can be defined by the user, who can follow the guidelines and the sample calculation results of this article as a basis for adapting this method to any specific needs. From the different presented test-cases, it is predicted that lineshapes defined with about 20–30 points suffice for ensuring enough accuracy for most of the radiative transfer applications. For mediums close to optically thin conditions, lineshapes with less than 10 points are sufficient. Also, it has been verified that using a ''pseudo-continuum'' approach in the simulation of molecular spectra leads to considerable calculation speed-ups with a minimum loss of accuracy (typically, for the more relaxed thresholds, a decrease to about 25% of the original calculation times is achieved for less than a 15% loss in accuracy).

The source code of the method, along with the line-by-line code SPARTAN and its accompanying spectral database, can be made available from the author upon request [29].

References

[1] Lino da Silva M. Simulation des Propriétés Radiatives du Plasma Entourant un Véhicule Traversant une Atmosphère Planétaire à Vitesse Hypersonique: Application à la planète Mars. Ph.D. thesis, Université d'Orléans, Orléans, France; 2004 [in French].
[2] Peraiah A. An introduction to radiative transfer: methods and applications in astrophysics. Cambridge, UK: Cambridge University Press; 2002.
[3] Kalkofen W. Numerical radiative transfer. Cambridge, UK: Cambridge University Press; 1988.
[4] Mazoue F, Marraffa L. Flow-field/radiation coupling analysis for Huygens probe entry into Titan atmosphere. In: AIAA Paper 2005—5392, 38th AIAA thermophysics conference, Toronto, Ontario, 6–9 June 2005.
[5] Wright MJ, Bose D, Olejniczak J. The impact of flowfield–radiation coupling on aeroheating for Titan aerocapture. J Thermophysics Heat Transfer 2005;19(1):17–27.
[6] Johnston CO, Hollis BR, Sutton K. Radiative heating methodology for the Huygens probe. In: AIAA Paper 2006—3426, 9th AIAA/ASME joint thermophysics and heat transfer conference, San Francisco, CA, 5–8 June 2006.
[7] Osawa H, Matsuyama S, Ohnishi N, Sawada K. Comparative computation of radiative heating environment for Huygens probe entry flight. In: AIAA Paper 2006—3772, 9th AIAA/ASME joint thermophysics and heat transfer conference, San Francisco, CA, 5–8 June 2006.
[8] Oinas V. A new method for the rapid calculation of infrared transmittances of atmospheric gases. JQSRT 1981;26(4):381–3.
[9] Oinas V. Rapid transmittance integration using line blending and a straight-line fit to line shapes. JQSRT 1983;29(5):407–11.
[10] Schreier F. Voigt and complex error function—a comparison of computational methods. JQSRT 1992;48(5/6):743–62.
[11] Wells RJ. Rapid approximation to the Voigt/Fadeeva function and its derivatives. JQSRT 1999;62(1):29–48.
[12] Kobayashi H. Line-by-line calculation using Fourier-transformed Voigt function. JQSRT 1999;62(4):477–83.
[13] Whiting EE. An empirical approximation to the Voigt profile. JQSRT 1968;8(6):1379–84.
[14] Olivero JJ, Longbothum RL. Empirical fits to the Voigt line width: a brief review. JQSRT 1977;17(2):233–6.
[15] Zhu X. An improved Voigt line approximation for the calculations of equivalent width and transmission. JQSRT 1988;39(6):421–7.
[16] Smith AJ, Gogel T, Vandevelde P. Plasma radiation database PARADE, Final Report, ESTEC Contract 11148/94/NL/FG, TR28/96, April 1996.
[17] ESA SP-533. In: Proceedings of the 1st international workshop on radiation of high temperature gases in atmospheric entry, 8–10 October 2003, Instituto Superior Técnico, Lisboa, Portugal.
[18] ESA SP-587. In: Proceedings of the 1st international workshop on radiation of high temperature gases in atmospheric entry—part II, Porquerolles, France, 1–2 October 2004.
[19] ESA SP-629. In: Proceedings of the 2nd international workshop on radiation of high temperature gases in atmospheric entry, Rome, Italy, 6–8 September 2006.
[20] Lino da Silva M, Dudeck M. A proposed solution to test-case 1 using the SESAM code. In: ESA SP-533, 1st international workshop on radiation of high temperature gases in atmospheric entry, 8–10 October 2003, Instituto Superior Técnico, Lisboa, Portugal. p. 121–6.
[21] Vacher D, Faure G, Lino da Silva M, Dudeck M, Andre P. Definition of a new level one test case: measurements of equilibrium radiation from an inductively coupled plasma in the near-UV to near-IR spectral region for a Martian-type CO_2–N_2 mixture. In: ESA SP-587, 1st international workshop on radiation of high temperature gases in atmospheric entry—part II, Porquerolles, France, 1–2 October 2004.
[22] Lino da Silva M, Dudeck M, Vacher D, André P. A solution for test-case 5: simulation of the radiative emission of a chemical equilibrium 97% CO_2–3% N_2 atmospheric pressure plasma. In: ESA SP-629, 2nd international workshop on radiation of high temperature gases in atmospheric entry, Rome, Italy, 6–8 September 2006.
[23] Mitsel AA, Ponomarev YN, Firsov KM, Ptashnic IV, Kataev MY. The computer codes LARA and AIRA for simulating the atmospheric transmittance and radiance: current status. JQSRT 1995;54(3):559–72.

[24] Kuntz M, Höpfner M. Efficient line-by-line calculation of absorption coefficients. JQSRT 1999;63(1):97–114.
[25] Quine BM, Drummond JR. GENSPECT: a line-by-line code with selectable interpolation error tolerance. JQSRT 2002;74(2):147–65.
[26] Schreier F. Optimized evaluation of large sum of functions using a three-grid approach. Comput Phys Commun 2006;174(10):783–92.
[27] Titov DV, Haus R. A fast and accurate method of calculation of gaseous transmission functions in planetary atmospheres. Planet Space Sci 1997;45(3):369–77.
[28] Mitsel AA, Firsov KM. A fast line-by-line method. JQSRT 1995;54(3):549–57.
[29] ⟨http://cfp.ist.utl.pt/radiation/SPARTAN/⟩.

A CONTRIBUTION FOR THE SIMULATION OF VUV-IR RADIATION TRANSFER IN CO_2–N_2 ENTRY FLOWS USING A LINE–BY–LINE MODEL

M. Lino da Silva[1]

[1]Instituto de Plasmas e Fusão Nuclear, Laboratório Associado, Instituto Superior Técnico, 1 Av. Rovisco Pais, 1049–001, Lisboa, Portugal

ABSTRACT

Departing from the proposed Test-Case 3 for the simulation of Martian atmospheric entry radiative transfer, we present several simulations carried out using a full line-by-line spectral simulation, ranging from VUV to IR. Namely, the radiation of CO_2 Infrared transitions are treated using a two-temperature (T,T_v) line-by-line model. Several calculations are presented which showcase the ability to solve the uncoupled radiative transfer problem (Heat transfer towards a spacecraft thermal protections) in a timely fashion, using a 8-core, 32GB RAM Linux Debian machine. In these calculations, different criteria are evaluated (1T vs. 2T models; different line-by-line spectral grid parameters; different spatial grids for radiative transfer) which allow determining their inpact on the overall predicted wall fluxes.

1. INTRODUCTION

This work presents a contribution for TC3 focused on the quantification of sensitivity to several parameters, such as spatial and spectral grid shapes, and the contribution of Visible-VUV spectral systems to the overall radiative power budget of Martian Entries, which is known to be dominated by CO_2 and CO IR transitions (Charbonnier 2003; Omaly:2005; Lino da Silva 2004). Such contributions are expected to allow a better tailoring of Computational Fluid Radiative Dynamics (CFRD) calculations, for the specific case of CO_2–N_2 mixtures.

Indeed, convergence studies on TC3 have been scarce up to now, and the only available recommendations concern the number of rays to sample in the scope of such simulations, in a study briefly mentioned by Rivière et al. (Riviere 2003). However, there is no information on what spatial and spectral grids sizes strike the best compromise between accuracy and reasonable dataset size. The spectral calculations implemented in the scope of this work are based on the line-by-line approximation, using IPFN in-house SPARTAN code. Radiative transfer procedures are also based on first rinciples, solving the radiative transfer equation using a ray-tracing routine. Therefore, the conclusions of this work are mostly applicable for this kind of direct approaches for radiative transfer. As it will be discussed more ahead in this article, the computational tools currently available already allow achieving very reasonable calculation times, allowing the phasing out of approximate radiative methods (such as band models). While allowing very fast calculation times and reasonably accurate results, these methods also suffer from conceptual restrictions, which essentially make them less universal than line-by-line models.

2. RADIATIVE MODELS

2.1. Spatial Grid for Radiative Transfer

The first step of this work has been the definition of a suitable radiative grid. Although the SPARTAN code lineshape routine uses variable grid methods in order to achieve more compact grids, grid sizes ranging from 1/2 to 2 million points are routinely achieved if one considers the whole VUV-IR spectral range. Therefore one may not define very large number of spatial cells, as each one has a size of around 100MB. An acceptable number of spatial cells is therefore around 500–1000.

We have departed from the structure flowfield grid proposed by RTech, adding some small fixes to points which got inside the spacecraft boundaries, and adding some additional points for the better definition of a spacecraft edge, as seen in Fig. 1.

The averaging procedure of the grid cells has to be carefully considered. One might simply average the values of the four vertex of the cells. However this approach might be oversimplistic in the case of large cells where for example one might have a hot region in the center, surrounded by colder vertex. Instead the sounder approach consists in a simple averaging of the original points inside the cell, or a weighted averaging if said points are not equispaced. An illustration of the averaging procedure is presented in Fig. 2. As an illustration, the differences in the averaging of the initial RTech temperature flowfield over a coarser grid is presented in Fig. 3. One may see that the differences in the averaged temperatures may exceed 500K in the regions of larger gradients, such as the

Proc. '4th Int. Workshop on Radiation of High Temperature Gases in Atmospheric Entry', Lausanne, Switzerland, 12–15 October 2010 (ESA SP-689, February 2011)

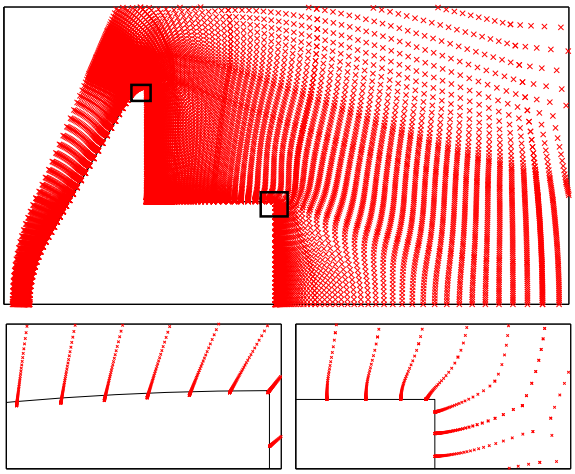

Figure 1. Details of the original RTech grid.

shock layer.

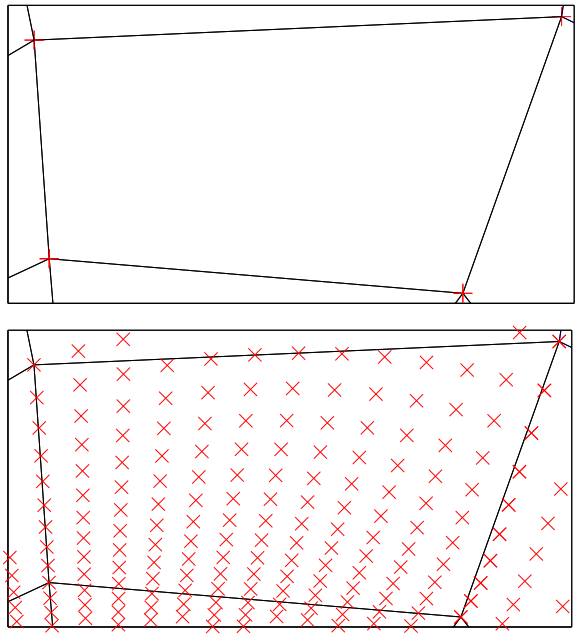

Figure 2. Averaging procedure over one grid cell.

In addition to the mandatory 24 points in the spacecraft afterbody region, we define an additional 24 points in the forebody region, in order to allow for a more complete simulation of radiative transfer towards the entirety of the spacecraft wall boundaries. The discretized wall points are presented in Fig. 4

The associated averaged radiative grid is presented in Fig. 5

Radiative calculations are carried out resorting to the ray-tracing method. In this method one samples a sufficiently high number of light rays at constant zenithal

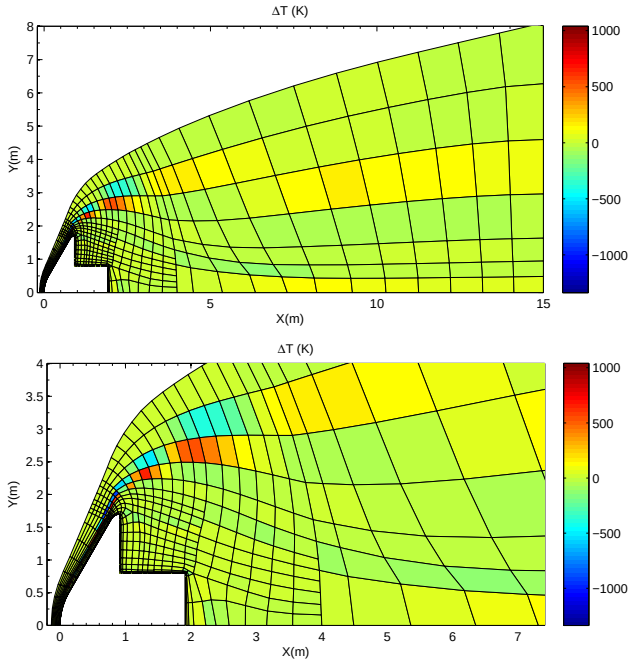

Figure 3. Differences of the two procedures for the temperature field.

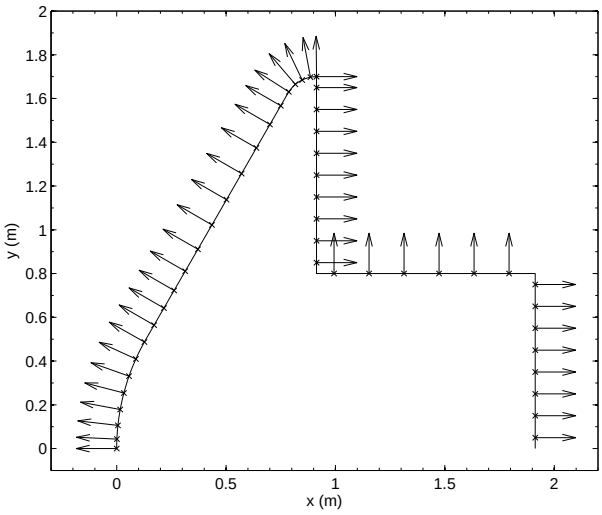

Figure 4. Wall points for radiative transfer.

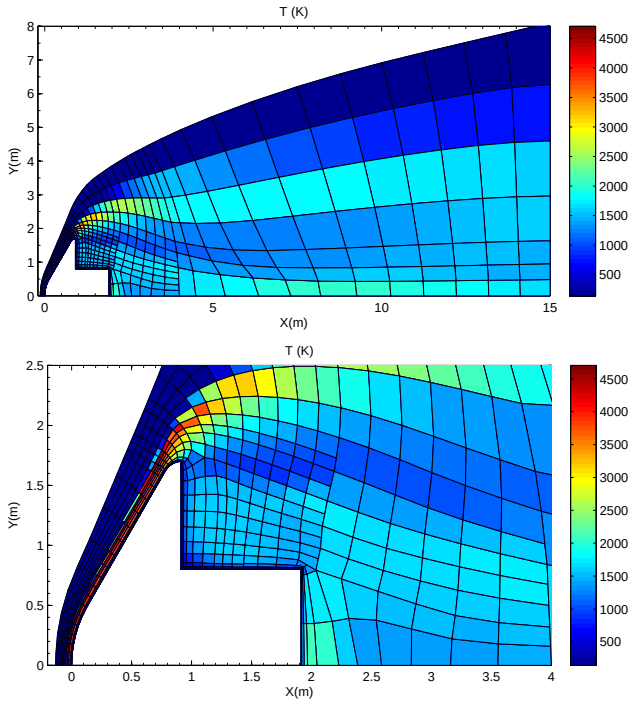

Figure 5. Averaged radiative grid.

and azimuthal angles. As the number of rays is increased, the radiative flux through a surface such that (Anderson 2000):

$$q_w = \int \int I_w(\theta, \varphi) cos\theta \sin\theta \sin d\theta d\varphi \qquad (1)$$

converges to the exact value.

and for each ray path, we have the traditional equation for radiative transfer (excluding scattering):

$$\frac{dI}{dl} = \varepsilon_\lambda - \alpha(\lambda) I_\lambda \qquad (2)$$

The ray-tracing routine itself has been developed taking into advantage the cartesian structure of the radiative grid. Each ray is sampled over equispaced $0.5\mathrm{mm}$ points, and each of these points is then determined to fall inside a specific cell. Taking into account the axi-symmetry of the flowfield, the length of the ray which crosses each specific cell is the calculated. The zenithal angle is calculated from 0 to 180°, and the azimuthal angle is calculated from 0 to 90°, taking into account axi-symmetry of the flow, as stated before. Angle intervals are fixed at 15°, according to the recommendations from (Riviere 2003). A total of 21,600 rays is sampled in this fashion for the 48 wall points.

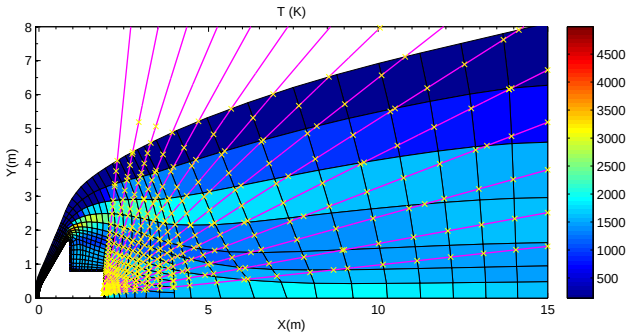

Figure 6. Sample rays at a 0° azimuth, for a given point in the spacecraft backcover

2.2. Line-by-Line Model and Associated Database for CO_2 Flows

The SPARTAN code (SPARTAN) is capable of simulating around 60 bound, bound-free and free radiative transitions from more than 20 chemical species ranging from the VUV to the IR region, with typically 10^4 to 10^6 lines and the superposition of several continua.

The code numerical routines are capable of simulating bound-bound atomic and molecular radiation. Molecular radiation routines include fine-structure effects, as they are capable of simulating singlet, doublet and triplet transitions, as well as accounting for Λ-doubling. Bound-free radiation like photodissociation, photoionization and photodetachment transitions can be accounted for according to available cross-sections from the literature, regardless of whether they are integrated over specific temperature ranges, or state-specific. Free-free transitions like Bremsstrahlung are also accounted for, using the most popular theoretical and semi-empirical expressions found in the literature. For low-pressure plasmas, the dominant line-broadening process will be Doppler broadening, although collisional broadening processes might not be completely irrelevant, and they are equally accounted for, considering a Voigt line profile in an efficient lineshape routine allowing fast and accurate spectral simulations(Lino da Silva 2007).

For CO_2–N_2 plasmas, the spectral database described in (Lino da Silva 2004; Lino da Silva 2006) is considered. In the case of pure CO_2 plasmas, the database can be further reduced to the one presented in Tab. 1.

2.3. Hardware for Calculations

The calculations presented in this report have been carried out in a Linux Debian Intel x86 8-core machine with 32GB of RAM and two RAID-1 1TB storage space. As it has been previouslyy discussed, the selected lineshape parameters, alongside with the number of spatial cells for radition, lead to overall radiative field with a size of 25–50GB, depending on the entry point. When radiative transfer calculations are being carried out, it is not feasible to directly load the radiative cells emission and absorption coefficients, as this leads to I/O operations tak-

Table 1. Spectroscopic Database for the Simulation of the EXOMARS Radiative Field

species	system	upper state – lower state	bands (v'_{max}, v''_{max})
Martian-like molecular systems			
CO	X-X	$X^1\Sigma^+ - X^1\Sigma^+$	(10; 10)
	Fourth-Positive	$A^1\Pi - X^1\Sigma^+$	(10; 10)
	Third-Positive	$b^3\Sigma^+ - a^3\Pi$	(2; 10)
	Angstrom	$B^1\Sigma^+ - A^1\Pi$	(2; 10)
	Triplet	$d^3\Pi - a^3\Pi$	(10; 10)
	Asundi	$a'^3\Pi - a^3\Pi$	(10; 10)
CO_2	–	–	613 bands
Earth-like molecular systems			
O_2	Schumann-Runge	$B^3\Sigma_u^- - X^3\Sigma_g^-$	(10; 10)
Atomic lines			
species	database	model	electronic levels
C	NIST (NIST)	–	272
O	NIST (NIST)	–	377

species	database	model	electronic levels
atomic photoionization			
C	Topbase (Topbase)	level Q_a	361
O	Topbase (Topbase)	level Q_a	245
molecular photoionization			
O_2	–	total Q_a	–
CO	–	total Q_a	–
CO_2	–	total Q_a	–
molecular photodissociation			
O_2	–	T-dependent Q_a	–
atomic photodetachment			
C^-	–	total Q_a	–
O^-	–	total Q_a	–

ing over 90% of the calculation time. It is therefore necessary to preallocate the different radiative data using a stack system. For such a purpose, a 28GB ramdrive has been implemented in the machine.

Figure 7. Multicore machine for radiative transfer calculations.

3. CONVERGENCE STUDIES

As discussed in (Lino da Silva 2007), the lineshape routine of the SPARTAN code is fully parametrical in the sense that it allows the user to select the accuracy of the calculated lineshapes, as well as the number of lines to be calculated explicitly and the lines to be added as a pseudo-continuum. Two sets of thresholds separate strong, weak and very weak lines. Strong lines are then calculated as a Voigt profile, Weak lines (W) are calculated as a Voigt profile if they are not covered by a strong line, and finally Very Weak (VW) lines always added as a pseudo-continuum. An illustration of this energy-conservative scheme is presented in Fig. 8

These two parameters have been tested for grid convergence investigations. The two sets of different lineshape and pseudo-continuum parameters have been tested, to-

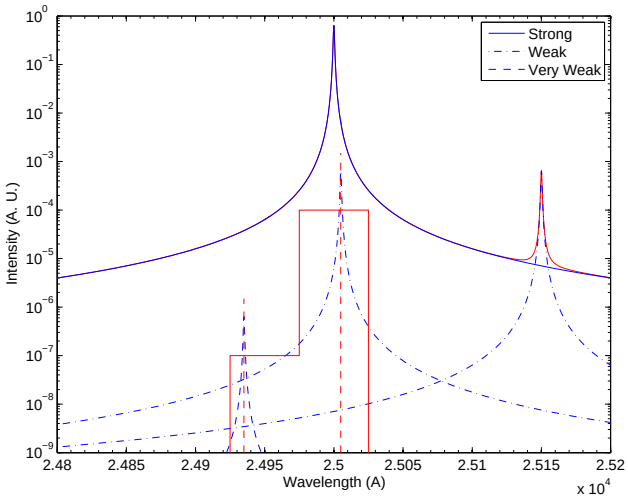

Figure 8. Example of Strong, Weak, and Very weak lines

talling 4 different sets of parameters. these are detailed in Tab.

Table 2. Spectral grid parameters

	(W,VW): $(10^{-3},10^{-6})$	(W,VW): $(10^{-2},10^{-4})$
(c,w):(13,25)	run 1	run 2
(c,w):(7,14)	run 3	run 4

c: line center points; w: line wings points;
W: Weak lines threshold;
VW: Very Weak lines threshold;

The obtained spectral fluxes are presented in Fig. 9 for run 1

We verify that wall fluxes issued from IR transitions (>10,0000Å) are predominant, due to CO_2 radiation with a smaller contribution from CO IR radiation. In the VUV-

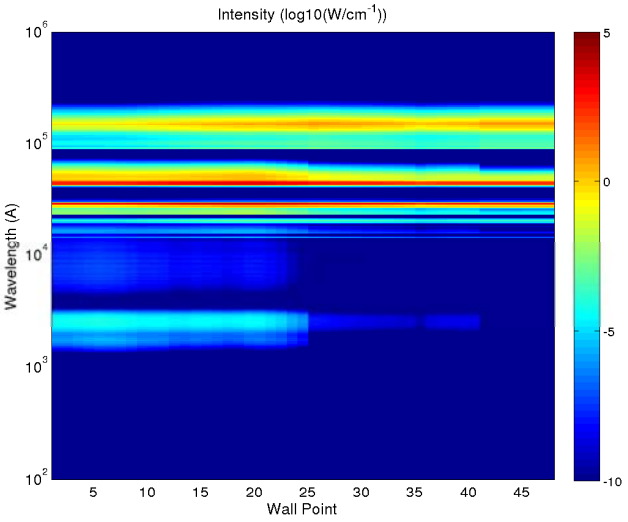

Figure 9. Spectral distribution of the wall fluxes, run 1

Visible region, traace radiation from CO 4^+, CO 3^+, and CO Angstrom systems can be observed, but only in the forebody region.

The spectrally integrated wall fluxes for the 4 runs is presented in Fig. 10

No significant differences are observed for variable thresholds, and differences for coarser lineshapes remain very faint. Non-IR fluxes are mostly negligible as they represent at most 2% in point 5 of the forebody.

4. CONCLUSIONS

Different spectral parameters have a lmited influence over the overall wall fluxes, and a strong influence on calculation times. Coarser adaptive line-by-line and pseudo-continuum grids lead to less Voigt lineshape calculations, and to more compact grids, which can be handled quicker. For the strictest run (1), spectral field and radiative transfer calculations take about 1 week, and for the more relaxed run (4), less than 3 days. The size of the radiative data is also $3\times$ smaller, which has an impact on memory (ramdrive) requirements. The overall calculation times are presented in Tab. 3

At the outset of this work on spectral convergence, a set of recommended parameters can be recommended from now on for line-by-line calculations of Martian entry flows. It is expected that these optimal parameters can be roughly valid for most of entry flows, namely the number of sampled rays (Riviere 2003), the number of Voigt Lineshape points, and the pseudo-continuum grid. This work has further shown that calculations can take as little as 3 days, which seems to be promising for the general application of detailed line-by-line models for these general radiation problems.

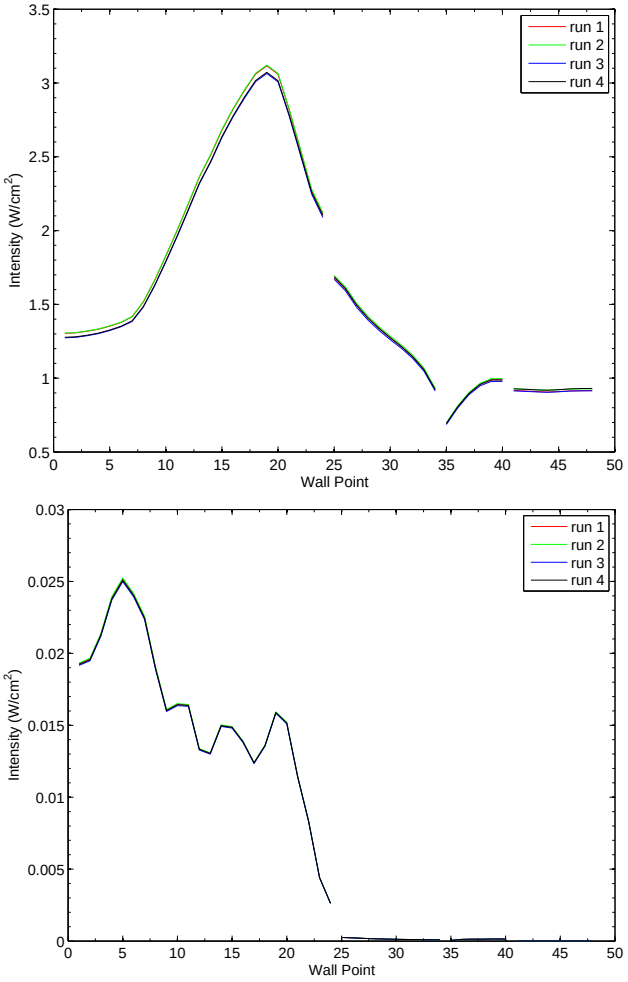

Figure 10. Spectrally interated wall fluxes for the 4 runs (top), and integrated wall fluxes in the VUV-Visible region (cutoff at 1 μm*)*

Table 3. Calculation times for the 4 runs

	(W,VW):(10^{-3},10^{-6})	(W,VW):(10^{-2},10^{-4})
(c,w):(13,25)	3 d; 4.5 d; 94GB	1.5 d; 3 d; 52GB
(c,w):(7,14)	1.5 d; 2.2 d; 41GB	0.9 d; 1.9 d; 28GB

c: line center points; w: line wings points; W: Weak lines threshold; VW: Very Weak lines threshold; shown: calculation times for radiative field; radiative transfer (in days), and spectral field grid size (in GB)

REFERENCES

Omaly P., and Marraffa L., "TC3: Update of the Axially Symmetric Testcase for High Temperature Gas Radiation Prediction in Mars Atmosphere Entry (TC3-3)".

Charbonnier, J.–M., "Analysis of the results for TC3 Presented at the 1st International Workshop on Radiation of High Temperature Gas in Planetary Atmosphere Entry", *ESA–SP533*, Proceedings of the First International Workshop on Radiation of High Temperature Gases in Atmospheric Entry, 8—10 Oct. 2003, Lisbon, Portugal, pp. 145–159.

Omaly, P., Dieudonne, W., and Spel, M., "Synthesis and Analysis for Test Case 3", *ESA–SP583*, Proceedings of the First International Workshop on Radiation of High Temperature Gases in Atmospheric Entry - Part II, 30 Sep.–1 Oct. 2004, Porquerolles, France, pp. 81–89.

Lino da Silva M., and Dudeck M., "Arrays of Radiative Transition Probabilities for CO_2–N_2 Plasmas", *J. Quant. Spectrosc. Radiat. Transfer*, Vol. 102, No. 3, 2006, pp. 348–386.

Lino da Silva M., "Simulation des Propriétés Radiatives du Plasma Entourant un Véhicule Traversant une Atmosphère Planétaire à Vitesse Hypersonique – Application à la Planète Mars", Ph. D Thesis (in French), *Université d'Orléans*, Dec. 2004.

Rivière, P., Soufiani, A., and Perrin, M.-Y., "Line by line and Statistical Narrow-Band Calculations of Radiative Transfer in Some Atmospheric Entry Problems", *ESA–SP533*, Proceedings of the First International Workshop on Radiation of High Temperature Gases in Atmospheric Entry, 8—10 Oct. 2003, Instituto Superior Tecnico, Lisbon, Portugal, pp. 189–196.

Anderson, J. D., "Hypersonic and High Temperature Gas Dynamics",American Institute of Aeronautics & Astronautics, 2000.

Lino da Silva M., "An Adaptive Line-by-Line-Statistical Model for Fast and Accurate Spectral Simulations in Low-Pressure Plasmas", *Journal of Quantitative Spectroscopy and Radiative Transfer*, Vol. 108, No. 1, 2007, pp. 106-125.

http://cfp.ist.utl.pt/radiation/

http://physics.nist.gov/PhysRefData/ASD/index.html

http://vizier.u-strasbg.fr/topbase/topbase.html